

CONSTRUCTION AND CHARACTERISATION  
OF A CODED-MASK GAMMA CAMERA FOR BEAM  
RANGE MONITORING IN PROTON THERAPY

MAGDALENA KOŁODZIEJ



PhD Dissertation

Supervisor: dr hab. Aleksandra Wrońska, prof. UJ

FACULTY OF PHYSICS, ASTRONOMY AND APPLIED COMPUTER SCIENCE  
JAGIELLONIAN UNIVERSITY

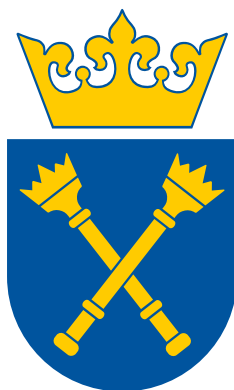
Kraków, Poland

February 2025



BUDOWA I CHARAKTERYZACJA KAMERY GAMMA Z MASKĄ  
KODOWANĄ DO KONTROLI ZASIĘGU WIĄZKI W TERAPII  
PROTONOWEJ

MAGDALENA KOŁODZIEJ



Praca doktorska

Promotor: dr hab. Aleksandra Wrońska, prof. UJ

WYDZIAŁ FIZYKI, ASTRONOMII I INFORMATYKI STOSOWANEJ  
UNIwersytet Jagielloński

Kraków

Luty 2025





## ABSTRACT

---

The major advantage of proton therapy over conventional radiotherapy is the dose deposition pattern: unlike X-rays, protons are entirely stopped in patient's tissues with a distinct maximum of energy deposition at the end of their range, the Bragg peak. This enables precise coverage of the tumour volume while sparing nearby healthy tissues. However, accurate control of the proton beam range online during patient irradiation is still considered a challenge. Thus, there are extensive efforts to develop a detector capable of *in vivo* beam range monitoring for proton therapy, among them, the coded-mask gamma camera developed by the SiFi-CC group. The assembly of this detector, as well as its first test under clinical conditions, are the subject of this thesis. The detector consists of a structured collimator made of tungsten, and a stack of thin, elongated scintillation fibres, read out at both ends by silicon photomultipliers. Such a design allows for efficient detection of prompt gammas and reconstruction of a prompt gamma depth profile, which is strongly correlated with the proton beam range. The readout system for the detector was selected in an extensive comparison study of five different systems. After detector assembly, the detector was tested under clinical conditions: a phantom was irradiated with proton beams of energies from 70.51 MeV to 108.15 MeV, the detector response was processed with low-level reconstruction software, and the maximum-likelihood expectation maximisation algorithm was applied to reconstruct the prompt-gamma depth profiles (images). The distal falloff positions of these profiles were determined and compared with the calculated proton ranges. The image reconstruction parameters were optimised in terms of accuracy of proton range shift determination. The results obtained were checked against a Geant4 simulation, showing good consistency. The statistical precision was found to be 1.7 mm for  $10^8$  protons for a reference position close to the centre of the camera field of view. The result is comparable to similar systems investigated by other research groups. However, simulation results suggest that certain hardware amendments to the detector can increase that precision about four times.

Since this thesis was pursued within the SiFi-CC project, which is a collaborative effort, the form "we" is widely used throughout the text. However, the majority of the work described here is the author's own contribution. In cases where a certain part of the work presented was done by another person, the fact is clearly stated in the footnote. Otherwise, the work was conducted by the author of this thesis.



## STRESZCZENIE

---

Główną zaletą terapii protonowej w porównaniu z konwencjonalną radioterapią jest rozkład dawki: w przeciwieństwie do promieniowania rentgenowskiego, protony są całkowicie zatrzymywane w tkankach pacjenta, gdzie występuje wyraźne maksimum depozycji energii - pik Bragga. Umożliwia to precyzyjne pokrycie objętości guza przy jednoczesnej minimalizacji dawki w otaczających zdrowych tkankach. Wyzwaniem jednak wciąż pozostaje dokładna kontrola zasięgu wiązki protonów w czasie rzeczywistym podczas napromieniowania pacjenta. Dlatego podejmowane są szeroko zakrojone wysiłki w celu opracowania detektora umożliwiającego monitorowanie zasięgu wiązki *in vivo* w terapii protonowej, a jedną z rozważanych opcji jest kamera gamma z maską kodowaną, opracowana przez grupę SiFi-CC. Budowa tego detektora, a także jego pierwszy test w warunkach klinicznych, są przedmiotem niniejszej pracy. Detektor składa się ze strukturalnego kolimatora wykonanego z wolframu i wiązki cienkich, wydłużonych włókien scyntylacyjnych, odczytywanych na obu końcach przez fotopowielacze krzemowe. Taka konstrukcja umożliwia wydajną detekcję natychmiastowego promieniowania gamma i rekonstrukcję profilu głębokościowego tego promieniowania, który jest silnie skorelowany z zakresem wiązki protonów. System odczytu detektora został wybrany w obszernym badaniu porównawczym pięciu różnych systemów. Po zmontowaniu, detektor został przetestowany w warunkach klinicznych: napromieniano fantom wiązkami protonów o energiach od 70,51 MeV do 108,15 MeV, odpowiedź detektora została przetworzona za pomocą oprogramowania do rekonstrukcji niskiego poziomu, a do rekonstrukcji profilu głębokości natychmiastowego promieniowania gamma (obrazów) zastosowano algorytm MLEM. Na profilach zlokalizowano pozycje spadku dystalnego i porównano je z obliczonymi zasięgami protonów. Parametry rekonstrukcji obrazu zoptymalizowano pod kątem dokładności wyznaczenia przesunięcia zasięgu protonów. Uzyskane wyniki porównano z symulacją wykonaną w środowisku Geant4, wykazując, że oba podejścia dają w dużej mierze spójne wyniki. Uzyskano precyzję statystyczną na poziomie 1,7 mm dla  $10^8$  protonów, w pozycji odniesienia blisko środka pola widzenia kamery. Wynik jest porównywalny z podobnymi systemami rozwijanymi przez inne grupy badawcze. Wyniki symulacji sugerują jednak, że pewne modyfikacje sprzętowe detektora mogą zwiększyć tę precyzję około czterokrotnie.

Ponieważ niniejsza praca została zrealizowana w ramach projektu SiFi-CC, który jest pracą zbiorową, forma „my” jest szeroko stosowana w całym tekście. Niemniej jednak większość opisanej tutaj pracy jest własnym wkładem autorki. W przypadkach, gdy pewna część przedstawionej pracy została wykonana przez inną osobę, fakt ten jest wyraźnie zaznaczony w przypisie. W przeciwnym razie praca została wykonana przez autorkę niniejszej dysertacji.



## ACKNOWLEDGMENTS

---

I would like to express my sincere gratitude to my supervisor, Prof. Aleksandra Wrońska, for her invaluable support, guidance, and encouraging me to take up challenges. Her expertise, insightful feedback, and inspiring passion for science taught me essential lessons, that helped me grow as a young researcher.

I am thankful to Katarzyna Rusiecka, for her invaluable practical advice and patience, countless times when she helped me solve problems I was stuck on, as well as all the good days spent together desk-by-desk in B-2-37.

I would like to thank Ming Liang Wong, for all the helpful advice and fruitful discussions. I genuinely enjoyed the cooperation on the DAQ comparison project, it was really inspiring and taught me a lot.

My appreciation extends to all the current and former members of the SiFi-CC group with whom I had the pleasure to work and whose input helped to write this thesis, especially Ronja Hetzel, Jonas Kasper, Monika Kercz, Rafał Lalik, Prof. Andrzej Magiera, Linn Mielke, Gabriel Ostrzolek, Prof. Magdalena Rafecas, and Vitalii Urbanevych.

I truly appreciate Wojciech Migdał, for invaluable technical support in the lab, even with the last-minute problems.

I am profoundly grateful to my parents Aleksandra and Jacek, for their unconditional support, encouragement, and inspiration.

Finally, I would like to thank my husband Tomasz, for his constant understanding, patience and support throughout this journey.



## CONTENTS

---

1	INTRODUCTION	1
1.1	Motivation	1
1.2	Proton therapy	1
1.2.1	Overview	1
1.2.2	Interaction of protons with tissue	2
1.2.3	Radiobiology	3
1.2.4	History	4
1.2.5	Current status and challenges	5
1.2.6	Proton therapy monitoring	7
1.3	Gamma scintillation detectors	9
1.3.1	Scintillation crystals	9
1.3.2	Silicon photomultipliers	11
1.3.3	Requirements for a PG detector for PT monitoring	12
2	THE SIFI-CC PROJECT	13
2.1	Detector modalities	13
2.1.1	Compton camera	13
2.1.2	Coded mask	14
2.2	Earlier studies and versions of the detector	15
2.2.1	Optimisation of fibre material and wrapping	15
2.2.2	Optimisation of the detector setup geometry	16
2.2.3	Small-scale prototype of a detector module	16
2.2.4	Small-scale prototype with a CM	17
2.3	Detector components	18
2.3.1	Scintillators	19
2.3.2	SiPM arrays	19
2.3.3	Silicon rasters	20
2.3.4	Masks	20
2.4	Front-end electronics and data acquisition system	21
2.4.1	SiPM readout systems	22
2.4.2	Experimental setup	24
2.4.3	Performance metrics	24
2.4.4	FEE and DAQ: results	27
2.4.5	FEE and DAQ: summary and discussion	29
2.5	Setup assembly	30
3	EXPERIMENTS	33
3.1	Laboratory tests	33
3.1.1	Calibration	33
3.1.2	Dead SiPM issue	35
3.2	Measurements with a proton beam	36
3.2.1	Conditions at Heidelberg Ion Beam Therapy Center	36
3.2.2	Experimental setup	36
3.2.3	Online results	38
3.2.4	Auxiliary measurements	40

4	DATA ANALYSIS	43
4.1	Overview	43
4.2	Preprocessing	43
4.2.1	Conversion of raw data to root trees	43
4.2.2	Nonlinearity correction	44
4.2.3	Data splitting and sorting	44
4.2.4	Time preselection	44
4.2.5	Simulation filtering	46
4.3	Low-level reconstruction	47
4.3.1	Structure and operation	47
4.3.2	Reading in the data	47
4.3.3	SiPM clustering	48
4.3.4	Finding fibre hits	49
4.4	Hit maps production	51
4.5	Auxiliary studies	51
4.5.1	Fibre calibration parameter spread per SiPM	52
4.5.2	Photon counts calibration	53
4.5.3	Inspection of fibre energy spectra	54
4.5.4	Hit maps in different beam spots	55
4.5.5	System stability over time	57
4.5.6	Background studies	59
4.5.7	Contributions of event classes in LLR	59
4.6	Analysis of Monte Carlo data	60
4.7	Image reconstruction	61
4.7.1	MLEM algorithm	61
4.7.2	Input to the image reconstruction	62
4.7.3	Efficiency correction	63
4.7.4	Distal falloff position determination	64
4.7.5	Optimisation of image reconstruction	65
4.8	Analysis of statistical precision	68
5	RESULTS	69
5.1	Rate capability	69
5.2	Detection efficiency	69
5.3	Dynamic range	69
5.4	Reconstructed images	70
5.5	Analysis of statistical precision	72
5.6	Simulation vs. experiment	74
5.7	Non-filtered simulation	74
6	DISCUSSION AND OUTLOOK	77
6.1	Detector performance	77
6.2	PG depth profiles - experimental and simulated	77
6.3	Clinical feasibility, significance	77
6.4	Prospects of moving to 2D CM imaging	78
7	SUMMARY AND CONCLUSIONS	79
A	APPENDIX	81
	BIBLIOGRAPHY	89





## ACRONYMS

---

**1D CM** one-dimensional coded mask

**2D CM** two-dimensional coded mask

**ADC** analog-to-digital converter

**ASIC** application-specific integrated circuit

**BP** Bragg peak

**CC** Compton camera

**CM** coded mask

**DAQ** data acquisition

**DFP** distal fall-off position

**FEE** front-end electronics

**FOV** field of view

**GUI** graphical user interface

**LLR** low-level reconstruction

**MLEM** maximum-likelihood expectation maximisation

**PCB** printed circuit board

**PCIe** Peripheral Component Interconnect Express

**PG** prompt gamma

**PGI** prompt-gamma imaging

**PMMA** polymethyl methacrylate

**PT** proton therapy

**QDC** charge-to-digital converter

**SiFi-CC** Silicon Photomultiplier and Scintillating Fibre based Compton Camera

**SiPM** silicon photomultiplier

**SM** system matrix

## INTRODUCTION

---

### 1.1 MOTIVATION

Cancer is the second most common cause of death in Europe [1]. A study on the US population showed that about 40.5% of men and 38.9% of women will receive a cancer diagnosis at some point of their lives [2]. Therefore, extensive efforts are directed towards finding a reliable method for treating various types of cancer. The most widely used treatments are chemotherapy, surgery, and radiotherapy. In the last one, various types of radiation are utilised: photons, electrons, or ions, mainly protons or carbon ions. Proton therapy (PT) has an advantage over more common X-ray therapy, which is a superior dose-deposition scheme. An X-ray beam passes through the patient's body, depositing most energy just under the surface, then the amount of deposited energy decreases with depth in tissue. In turn, protons stop at a certain depth in tissue and deposit most of their energy at the end of their range. This dose maximum is called the Bragg peak (BP). However, as a consequence of this scheme, very accurate beam range monitoring methods are needed to provide safe and precise treatment. A coded mask (CM) gamma camera, which is a subject of this thesis, is one of the approaches to develop such a monitoring method, based on imaging with prompt-gamma (PG) radiation. PG quanta are one of the by-products of tissue irradiation with a proton beam. They are emitted from the patient's body as a result of inelastic nuclear reactions and the following deexcitation of tissue nuclei. As the distribution of these gammas in tissue is strongly correlated with the proton range, by registering the PG distribution one can conclude about the proton range. Having a fast, reliable method of proton range determination would allow to improve PT and widen the scope of possible tumour locations that can be effectively treated with it.

### 1.2 PROTON THERAPY

#### 1.2.1 Overview

The concept of treating tumours with protons, as well as with heavier ions, relies on their several favourable features. Unlike X-rays, they do not pass all the way through the irradiated body but instead are stopped at a certain depth in tissue, depositing most of their energy in that region. This deposition scheme is well described by the Bethe-Bloch formula (see Section 1.2.3.1) and the said maximum is called the BP [3]. With this feature, treatment could be planned so that crucial organs located behind the tumour are fully spared, i.e., receive zero delivered dose. Moreover, any tissue on the way of protons receives less dose than the tissue at the end of their range, which is another advantage of PT compared to conventional X-ray therapy. A comparison of dose-depth profiles for protons and X-rays can be found in Figure 1.1a. The higher the beam energy, the deeper the tissue penetration. This is particularly beneficial in deep-seated tumour treatment. Another

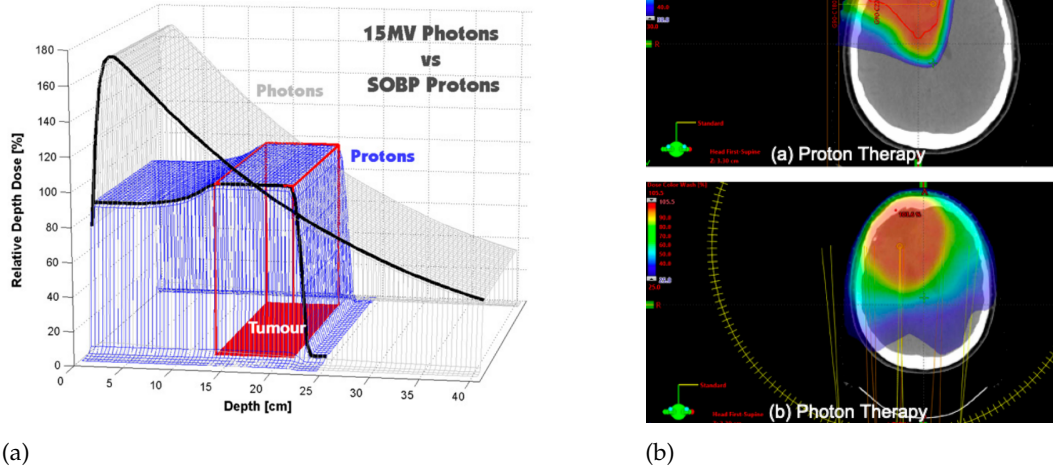


Figure 1.1: (a) Relative deposited dose in % of maximum dose vs. depth in tissue. Grey - photons (X-rays), blue - protons (spread-out BP), the tumour region is marked in red. (b) Example treatment plans for a brain tumour for proton (top) and X-ray (bottom) therapy. The colour scale denotes the relative dose deposited. The red contour in the top picture marks the tumour region. Both figures are adapted from [5].

favourable feature of protons is their relative biological effectiveness (RBE), which is about 10% higher than for X-rays [4]. All these effects contribute to a much better dose conformality than in X-ray therapy, as can be seen in Figure 1.1b, where dose delivery schemes (so-called treatment plans) for proton and X-ray therapy are compared.

### 1.2.2 Interaction of protons with tissue

The physical basis of PT is the interaction of protons with human tissue. There are four main types of proton interactions with tissue [6, 7]:

1. Coulomb interaction with electrons bound in atoms, resulting in ionisation (inelastic scattering),
2. Coulomb interaction with atomic nuclei (elastic scattering),
3. nuclear reactions,
4. brehmsstrahlung.

Coulomb interaction with bound electrons does not change the trajectory of the proton, but a fraction of its energy is transferred to each of the electrons, and hence the proton velocity decreases. It is the main factor causing the stopping of protons in the tissue, thus determining the proton beam range.

Elastic scattering causes a deflection in the proton trajectory as a result of repulsive Coulomb force. In the context of PT, this effect causes lateral broadening of the beam, also blurring its lateral borders.

When a nuclear reaction occurs, the proton enters the nucleus and, as a result, secondary particles are emitted from the nucleus: protons, neutrons, and heavier ions, as well as gamma rays. This effect causes the primary proton to be effectively removed from the beam. The PG quanta being emitted in this process are crucial for real-time PG-based PT monitoring methods.

Interactions due to brehmsstrahlung are associated with primary proton energy being partially lost due to deceleration caused by deflection by the nucleus and emitted in the form of a brehmsstrahlung photon. However, their significance for PT is negligible as they are dominated by the remaining three mechanisms.

### 1.2.3 Radiobiology

The crucial parameters characterising the radiation, related to its dose distribution in the tissue and biological consequences are: linear stopping power, linear energy transfer (LET) and relative biological effectiveness (RBE).

#### 1.2.3.1 Linear stopping power

The energy loss associated with the interactions described in the previous section is quantified with the Bethe-Bloch formula [8, 9]:

$$\left\langle -\frac{dE}{dx} \right\rangle = Kz^2\rho \frac{Z}{A} \frac{1}{\beta^2} \left[ \frac{1}{2} \ln \frac{2m_e c^2 \beta^2 \gamma^2 W_{max}}{I^2} - \beta^2 - \frac{\delta(\beta\gamma)}{2} \right], \quad (1)$$

where:

$E$  - particle energy,

$x$  - distance travelled by the particle in the medium,

$K = 4\pi N_A r_e^2 m_e c^2$  - a constant,

$N_A$  - Avogadro's number,

$r_e$  - classical electron radius,

$z$  - charge number of the particle,

$\rho$  - density,

$Z$  - atomic number of the medium,

$A$  - atomic mass of the medium,

$c$  - speed of light,

$v$  - the particle velocity,

$\beta = v/c$ ,

$\gamma = 1/\sqrt{1-\beta^2}$ ,

$m_e$  - electron mass,

$W_{max}$  - maximum possible energy transfer to an electron during a single collision,

$I$  - mean excitation energy,

$\delta(\beta\gamma)$  - density effect correction to ionisation energy loss.

The equation defines the linear stopping power, the units are MeV/cm. The mass stopping power is the linear stopping power divided by the density, the units are then MeV g<sup>-1</sup>cm<sup>2</sup>. In the leading term of the Bethe-Bloch formula (Equation (1)), the dependence of the energy transferred to the medium by the particle per unit path length is inversely proportional to the squared particle velocity. Thus, the lower the particle energy, the higher the energy deposition in that region. This

dependence explains the shape of the dose-depth curve. Also, for heavier particles (e.g.  $^{12}\text{C}$ ), the distal falloff of the BP is steeper than for protons, which is a result of smaller range straggling. This feature varies inversely to the square root of the particle mass. The same dependence occurs for the lateral profile of the beam. The lateral broadening of the dose distribution can be approximated by a Gaussian, but for higher accuracy, one needs to consider the Moliere's theory, which takes into account additional scattering at larger angles, making the lateral penumbra wider than for a simple Gaussian.

#### 1.2.3.2 *Linear energy transfer*

Linear energy transfer [3] is defined as the energy locally transferred to the medium per unit track length (that is, depth) in the medium. The LET increases with  $Z$ , e.g.  $^{12}\text{C}$  ions have higher LET than protons. Higher LET means the dose is more localised, which is favourable for therapy. Dose-averaged LET is a quantity widely used when assessing radiation quality.

#### 1.2.3.3 *Relative biological effectiveness*

X-ray biological effectiveness is considered a reference, the effectiveness of other types of radiation is assessed relative to it. RBE is defined as a ratio of the reference radiation (X-ray) dose absorbed to the given radiation dose at which the biological effect would be identical (isoeffective), assuming that all other conditions are the same for the examined and reference radiation [10]. Currently, the proton RBE in clinics is assumed constant along the particle path and equal to 1.1. However, there are arising claims that RBE in PT should be variable [4, 11, 12, 13]. For carbon ions, RBE varies along the particle path and ranges from about 2 in the entrance region to about 4 near the end of the particle range. RBE depends on several variables, most significant ones being dose fractionation changes, LET,  $\alpha/\beta$  ratio [3].

The latter are the parameters of the linear-quadratic (LQ) model [14], which relates the dose delivered to cell survival:  $s = e^{-\alpha d - \beta d^2}$ , where  $s$  is the probability of survival and  $d$  is the dose delivered.  $\alpha$  and  $\beta$  parametrise the radiosensitivity of a given cell type. The term  $\alpha$  corresponds to cell death after being hit by a single particle, while the term  $\beta$  represents killing after multiple hits. Tissues with different  $\alpha/\beta$  ratio react differently to radiation. There are cell repair effects that occur some time after irradiation and are more pronounced in the tissue with a lower  $\alpha/\beta$  ratio. This characteristic can be used for more effective treatment, by dividing the total dose into smaller portions in time (dose fractionation), under the condition that the tumour tissue has a higher  $\alpha/\beta$  ratio than the healthy tissue [3].

#### 1.2.4 *History*

The idea of using protons for cancer treatment was first mentioned in Robert Wilson's paper in 1946 [15], where he discussed the potential of the use of accelerated protons for therapeutic irradiation, described the effects of protons' interactions with tissue and theoretical limits of available precision resulting from these interactions, attributed to range straggling and the angular spread. The first treatment of a human patient with accelerated protons was performed at a cyclotron

in Lawrence Berkeley Laboratory [16]. That was an irradiation of the pituitary gland. Soon after, Larsson and others irradiated animals with a beam of modified shape by focusing magnets and sweeping coils [17], which formed a basis for the spread-out Bragg peak (SOBP) technique and therefore the passively scattered beam. In 1962, Kjellberg et al. treated four patients with brain tumours by irradiation with a 160 MeV proton beam [18]. In the following decades, patients were treated with PT at a small scale in several research facilities i.e. in the US, Sweden and Russia. In 1990, the first clinical facility was commissioned at the Loma Linda University Medical Center in California. Since then, PT centres were predominantly located near hospitals rather than in research facilities. A decade later, commercial companies emerged which offered off-the-shelf PT systems, which enabled further development of PT. The number of PT facilities worldwide has been growing steadily over the last few decades, reaching 121 in June 2024, with close to 350 000 patients treated [19]. PT is nowadays an established method of cancer treatment, along with surgery, chemotherapy, conventional radiotherapy and the most recent immunotherapy.

#### 1.2.5 *Current status and challenges*

Over the years of PT progress, various techniques and technologies have been developed. Regarding the beam delivery system, there are two main options: passive scattering [20, 21] and active scanning [22, 23]. The general scheme of both is presented in Figure 1.2. Passive scattering is an older, but still widely used method. To be able to deliver the dose precisely to the tumour, the beam undergoes scattering to increase its field, passes through a range modulator, then it is shaped in passive collimators matching the tumour shape. Subsequently, range compensators are applied to correct for tissue density irregularities on the way of the beam. After applying such a shaping procedure, the lateral beam profile exactly matches the tumour shape. Uniform irradiation of the tumour along its proximal-distal axis is performed by superimposing beams of several energies (with a range modulator wheel or a Ridge filter), forming the SOBP. In turn, active scanning, also known as intensity-modulated proton therapy (IMPT), relies on a system of magnets that can narrow the cross section of the beam and bend the beam to direct it to the desired voxel. A beam shaped this way is called a pencil beam, thus another name of this modality is pencil beam scanning (PBS). The tumour volume is segmented into voxels and the pencil beam is directed and delivered to each voxel separately. There are several disadvantages of the passive scattering: the proximal dose conformality is quite poor, there is a need to machine patient-specific hardware for each treatment, secondary neutrons are produced as a result of beam scattering on the passive elements. The above issues are not the case for PBS. There, the proximal edge of the beam can be shaped as needed and there is much less neutron background thanks to the lack of shielding or passive elements. Another approach to beam delivery, which is in the early clinical stage, is FLASH radiotherapy [24]. In this case, the entire dose is delivered to the tumour with a single, high-rate beam "shot" (minimum 40 Gy/s). It has been demonstrated that such a delivery scheme reduces radiation damage to healthy tissues, as compared

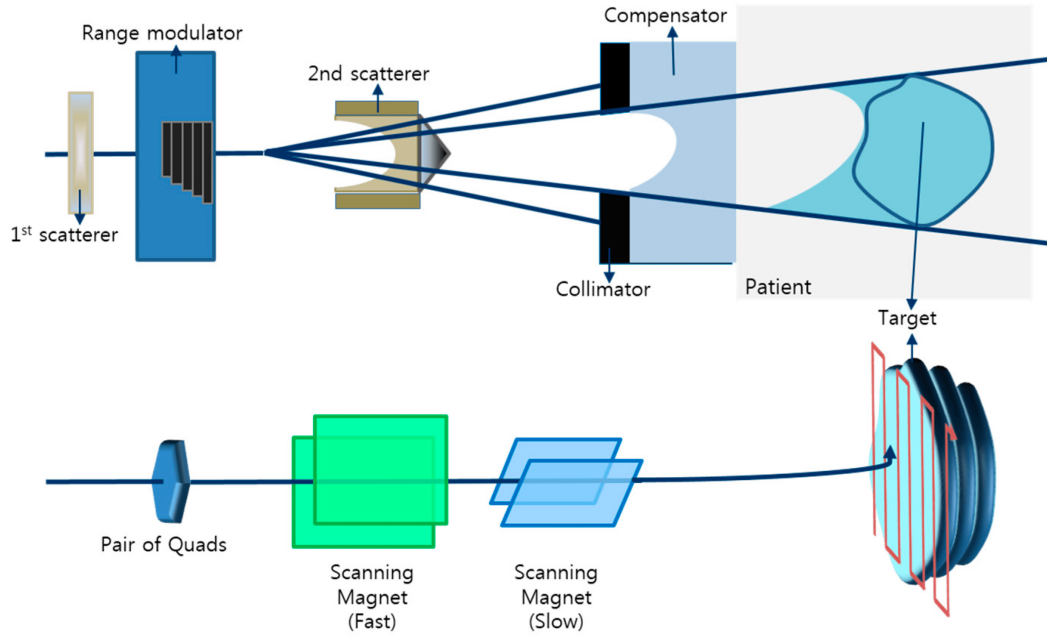


Figure 1.2: Passive scattering (top) and active scanning (bottom) beam delivery systems. Adapted from [29].

to regular PT. This phenomenon is called the FLASH effect. The first in-human test of the FLASH PT was performed in 2022 [25, 26].

Proton beams in the treatment facilities are typically accelerated using either a cyclotron or a synchrotron. They can be delivered to the treatment room via a fixed-position horizontal nozzle or a rotational gantry. Both the accelerators and the beam delivery systems are complex and large-scale. Therefore, a PT facility is much more expensive than an X-ray one. The high cost is one of the main factors that limit the common usage of PT. Another strong limitation is the accuracy of beam range monitoring. Due to the particular dose deposition scheme in PT, even a minor change in the patient anatomy relative to the original treatment plan can result in a significant extra dose deposited in healthy tissue. Thus, various measures are applied to minimise the risk of dose inaccuracy, i.e. patient immobilisation, laser markers on the outer surface of the body or adjusting the irradiation time to breathing cycle if a tumour is located in the lung region. However, currently applied PT monitoring methods provide feedback only after an irradiation session, which allows one to adjust treatment plan for the next treatment session, but not during the current one. In view of the above conditions, an online method of beam range monitoring, providing feedback in real time, would be the most beneficial. However, currently there is no such a method applied routinely in clinics, though the first clinical trials are ongoing [27]. This has been indicated to be one of the key factors that limit the applications of PT [28]. The approaches to developing such a method are summarised in the following section.



### 1.2.6 Proton therapy monitoring

Methods for *in vivo* range verification in PT have been reviewed in [30]. There, the authors distinguish two general-purpose methods utilising secondary radiation: positron emission tomography (PET) and PG detection. Several types of secondary radiation emitted from the patient's body during radiation treatment correlate with the range of proton beam in tissue, so they can be utilised for monitoring. These can be protons [31, 32], neutrons [33],  $\beta^+$  emitters and PG rays (both discussed below), or some combination of them [34, 35]. PET uses the  $\beta^+$  emitters, while PG detection utilises PG rays, as the name suggests.

#### 1.2.6.1 Positron emission tomography

One of the by-products of tissue irradiation with protons are  $\beta^+$  emitters. They are produced in nuclear fragmentation reactions, which occur along the whole path of an ion in the tissue, up to a few mm before the BP. The correlation of their activation pattern with dose spatial distribution depends on the type of primary ion, but it is stronger for heavier ions, e.g. for carbon ions, than for protons. The half-life time of the  $\beta^+$  emitters produced in tissue ranges from e.g. 2 minutes for  $^{15}\text{O}$  and 20 minutes for  $^{11}\text{C}$ . Due to those relatively long times, there is an effect of biological washout, which puts a serious limitation on the technique resolution. The effect is amplified by the fact that the pairs of gamma quanta are usually registered only after the treatment session, after moving a patient to another room with a PET scanner. However, there is a recent solution which diminishes the problem of biological washout, proposed by Bisogni et al. [36], which involves first in-beam PET for online beam range monitoring, making use of a dedicated dual-head scanner setup. The PET signal is correlated with, but not identical with the dose distribution, so in order to draw conclusions about the dose distribution, one needs to compare the obtained PET image with a Monte Carlo (MC) or analytically calculated expected image.

#### 1.2.6.2 PG detection

PG rays are one of the by-products of the reactions between the impinging protons and nuclei of human tissue. A proton excites a nucleus, which then deexcites, emitting PG rays. They are a valid choice for PT monitoring due to the following characteristics:

1. they are emitted within a very short time after the proton-nucleus interaction (femto - picoseconds),
2. thanks to their high energy, their trajectory barely changes when exiting the patient's body. Hence, they carry undisturbed information about the place of interaction,
3. their spectrum contains discrete lines originating from nuclei of  $^{16}\text{O}$  at 6.13 MeV and  $^{12}\text{C}$  at 4.44 MeV (see Figure 1.3), which facilitates their separation from the continuous neutron background.

In 2006, Min et al. [37] demonstrated that the spectrum of PG rays emitted from the patient's body, particularly the distal falloff, strongly correlates with the range of

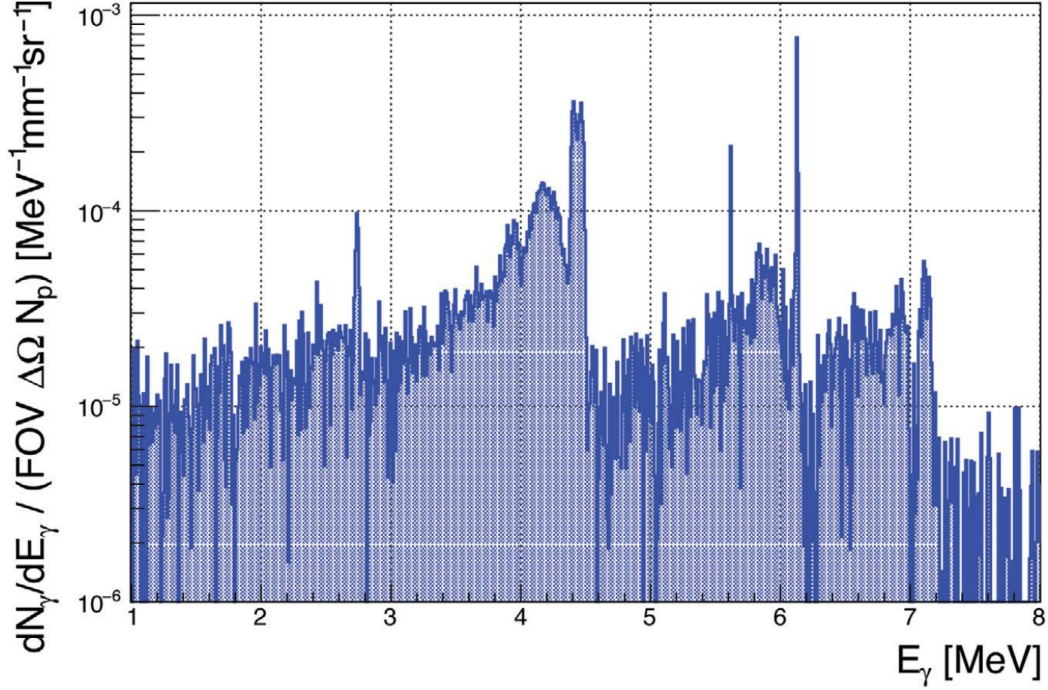


Figure 1.3: PG spectrum from a 1 mm thick layer of PMMA phantom irradiated with protons of 70 MeV energy, registered with a high-purity germanium detector, normalised to the number of primary protons, corrected for detector acceptance and efficiency. Horizontal axis is the target thickness expressed in the units of proton range in the material. Figure adapted from [55].

protons in the patient's tissues. That finding constituted the basis for PG range verification in PT, and the field has been growing rapidly ever since. The results obtained in a later experimental study that further explored the details of this correlation [38] are presented in Figure 1.4. The methods of PG range verification can be divided into two major groups: imaging and non-imaging techniques. The imaging techniques are, among others, a knife-edge shaped slit camera [39, 40], a multi-slit camera [41], and a Compton camera [42, 43, 44, 45] (see Section 2.1.1), while the non-imaging techniques include PG timing [46], PG spectroscopy [47, 48], and PG peak integrals [49]. Notably, an online proton range verification system based on PG was clinically applied for the first time by Richter et al. [39] in the form of a knife edge-shaped slit camera during a passive-scattered beam treatment. This detector has since been improved and applied to the first-in-human validation of proton range [27]. The first clinical application under pencil beam scanning conditions, during the whole treatment session, was presented in [40]. The slit camera has an intrinsic limitation of statistics, which is challenging in clinical applications. Thus, multi-slit setups were also tested [50, 51], as well as collimators with multiple knife-edge shaped slits [52]. Another type of collimator is a coded mask, described in detail in Section 2.1.2, which has superior statistics capabilities and has been tested via simulations and experimentally for PT monitoring applications in [53, 54]. The findings described in this thesis are extending and building on the concept described in the latter publication.

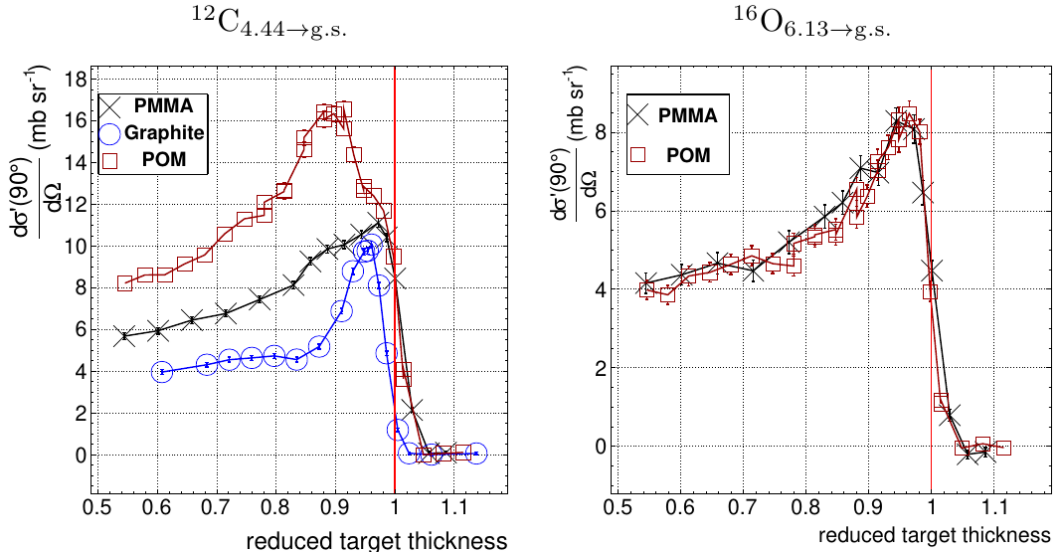


Figure 1.4: Measured depth-distributions of PG rays resulting from deexcitation of  $^{12}\text{C}_{4.44 \rightarrow \text{g.s.}}$  and  $^{16}\text{O}_{6.13 \rightarrow \text{g.s.}}$  in PMMA, graphite and POM. The reduced target thickness is the depth in the material, expressed in units of proton range in the material. Figure adapted from [38].

### 1.3 GAMMA SCINTILLATION DETECTORS

A common solution used to detect gamma quanta, but also other particles, is a scintillator, which emits a flash of light when ionising radiation deposits energy in it. Registration of this signal requires a photomultiplier, which converts this flash of light into an electric signal. An early version of a gamma camera for medical imaging was proposed by H. O. Anger in 1958 [56]. The core part of such a detector consists of a scintillating crystal and several photomultiplier tubes (PMTs). The concept was later extended in [57]. The field has since been developing intensively. Nowadays, there is a variety of scintillating materials available, optimised for various use cases. The photomultiplier tubes have since been replaced, at least in most of the use cases, by silicon photomultipliers (SiPMs). The following briefly characterises the typical building blocks of a typical scintillation detector, i.e., scintillating crystals and silicon photomultipliers.

#### 1.3.1 Scintillation crystals

A scintillator is a special kind of material that emits a flash of visible or near-visible light when exposed to ionising radiation [58], as a result of deexcitation of the scintillator molecules. The process is called scintillation or radioluminescence. A scintillator suitable for radiation detection applications is characterised with:

1. linear response to energy,
2. short response time and lack of long-time activation (this feature is essential for high-rate applications),
3. transparency to the wavelength at which the scintillation light is emitted,

#### 4. high light yield.

Scintillators can be divided into two main categories: organic and inorganic. A crucial difference between them is that while organic scintillators are usually based on polymers whose elemental composition is dominated by light elements (H, C, O), inorganic scintillators are usually made of materials with high effective atomic number  $Z_{\text{eff}}$  (so-called high-Z materials). Therefore, typically the inorganic scintillators have shorter radiation length, greater stopping power, and high light output, thus being the optimal choice for X-ray and gamma-ray detection. Inorganic scintillators are in the form of crystals, some examples of the commonly used ones are NaI(Tl), LaBr<sub>3</sub>, LSO.

The mechanism of scintillation in inorganic crystals can be explained based on the electronic band model [58]. A crystal in the ground state has approximately all energy levels populated in the valence band and approximately no levels occupied in the conduction band. Between these bands, there is the bandgap, i.e. an energy range without electron states. To enable light emission at desired wavelengths, the crystal must be doped with atoms that provide localised levels for the centres of luminescence in the bandgap. When a gamma ray hits the scintillator, an electron can be excited from one of the lower energy levels to the valence band or, more often, to a much higher energy level [59]. The electron will then lose its additional energy by exciting another electrons and so on. Thus, a single gamma hitting the scintillator produces multiple electron-hole pairs or separate electrons and holes. Then, the electrons and holes reach the luminescence centres and scintillation light is produced. One needs to note that this is a simplified model, the more precise one involves crystal impurities and the Stokes shift [59].

One of the features characterising the signal produced in the scintillation crystal is its decay time, which depends on the lifetime of a certain excited state. Usually, a short and long decay components are present in a plot of relative light emission versus time. They correspond to fluorescence and phosphorescence effects, respectively. Usually, the short component is dominant.

A scintillation crystal should, most desirably, have a linear response to energy [59]. It is true in the energy region of above 1 MeV, however, at lower energies certain deviations from linearity occur. The type of particle interacting with the scintillation crystal also affects its output, e.g. alpha particles are usually detected with a few times lower sensitivity than electrons [59]. The shape of the scintillation pulse produced by various particles can also vary, which is an underlying principle of a method of particle identification called pulse shape discrimination [60].

Gamma rays interact with matter in three dominant ways: photoelectric effect, pair production, and Compton scattering. While in the first two, the gamma is completely absorbed and its energy transferred to a particle (particles), in the last one, it leaves only part of its energy to an electron and can undergo further interactions or escape the material, not depositing its full energy there. Thus, in an efficient gamma-ray detector, the first two processes should dominate. This is the case for high-Z materials.

### 1.3.2 *Silicon photomultipliers*

A silicon photomultiplier is a solid-state silicon detector. It is essentially an array of hundreds to thousands of single-photon avalanche photodiodes (SPADs) or avalanche photodiodes (APDs) connected in series to quenching resistors. APDs and SPADs have similar principles of operation, but this section focuses on APDs. An APD together with a quenching resistor form a single pixel (microcell) of a SiPM. The size of such a single pixel (microcell) is typically  $10\ \mu\text{m}$  to  $100\ \mu\text{m}$  [61]. An APD is basically a semi-conductor p-n junction. Each APD operates in Geiger mode, which means that the bias voltage is above the breakdown voltage of the APD.

The operation principle of the APD is the following: if a photon is absorbed by the photodiode, the ejected charge carrier (an electron or a hole) triggers an avalanche and a continuous Geiger discharge starts. In such a process,  $10^5$  to  $10^6$  charge carriers are produced, forming an electrical pulse. The discharge is quenched by the resistor, so that the APD can return to its initial state and register another photon. The summed electrical pulses from all activated APDs during a single "event" form an output SiPM signal, proportional to the number of photons that reached the SiPM. Due to its internal structure, a SiPM lower detection threshold can be as low as a single photon, while the upper detection threshold is limited by the number of microcells. However, the saturation effect is already visible when the number of photons reaching a SiPM becomes comparable with the number of microcells. Then the effect becomes more pronounced with increasing number of activated microcells, up to a point where an increase in the number of incident photons has no impact on the pulse height anymore, due to full saturation.

SiPMs, unlike PMTs, are insensitive to magnetic fields. They are also smaller in size, and a lower bias voltage is required for their operation. Like all other light-sensitive devices, they must be operated in light-tight conditions; otherwise, they can be damaged due to large current increase. SiPMs can detect photons from the region close to the visible range, typically 300-900 nm [62]. The active surface of a typical SiPM ranges from one to several  $\text{mm}^2$ . Several characteristic parameters of the SiPMs are:

1. Gain, which is the number of charge carriers produced in a single microcell. The gain depends linearly on the bias voltage (in a limited range of accepted overvoltage). It is also temperature-dependent, which may lead to the need to use a cooling system.
2. Breakdown voltage, the highest voltage that can be applied before the current increases exponentially in the photodiodes.
3. Photon detection efficiency (PDE), which is a measure of the ability of the SiPM to detect photons. PDE varies depending on the wavelength of the incident light. It is the ratio of photons detected and photons impinging on the detector.
4. Dark count rate, the number of counts per unit time when there is no light reaching the SiPM from outside, caused by thermal activations inside the SiPM.



5. Afterpulse probability. A single incident photon can sometimes produce more than one electric pulse. The additional pulses are called afterpulses and contribute to SiPM noise.
6. Crosstalk probability. Crosstalk occurs when a secondary photon is produced after a hit in one microcell and is detected by one of the neighbouring cells. This effect also contributes to the SiPM noise.

The main areas in which SiPMs are used are low-light applications, e.g. PET, also with fast timing (time of flight - TOF PET), radiation detection in high-energy physics, single-photon measurements in spectroscopy, light detection and ranging (LIDAR), quantum experiments [63].

### 1.3.3 Requirements for a PG detector for PT monitoring

From a clinical point of view, the PG detector needs to meet the following criteria, in order to be applicable for PT monitoring [64]:

- The PG detector must be compatible with the beam delivery system. If there is a gantry, the detector should be gantry mountable.
- The monitoring process should not prolong the total treatment time, as it would limit the number of patients that can be treated and thus is not economically justified.
- The clinical workflow demands the irradiation time to be as short as possible, in order to reduce patient's strain and the risk of positioning errors due to patient's movement. Thus, the PG detector must be operable under high, clinical rates and cope with non-uniform beam time structure.

The first criterion puts a significant limit of the detector size and weight. The second one demands a fast data processing scheme allowing for getting results in real time. The last criterion sets constraints on the detector design, which are further discussed in this section.

Typically, the number of incident protons is about  $10^8$  for a single, distal spot in PBS. Irradiation of one spot lasts about 10 ms [65]. The resulting yield of PG rays is  $1 - 3 \times 10^7$ , emitted in full solid angle, resulting in the rate of  $1 - 3 \times 10^9$  cps. Assuming angular detector acceptance of the order of  $10^{-3}$ , the typical detector load is of the order of  $1 - 3 \times 10^6$ . Thus, the possible detector load and system throughput need to be maximised in a PG detector design. Efficient event selection criteria should also be applied, to eliminate as much background as possible. Moreover, the beam's time structure is irregular: huge leaps of the load occur. The detector has to be stable under such conditions. Finally, the PG detector should be segmented, having multiple pixels with independent readout, as this not only enables position sensitivity but also increases the possible data throughput, as the count rate is distributed among readout channels.

These criteria in view of our proposed detector design are addressed in Sections 2.1.1, 2.1.2 und 2.4.

The work presented in this thesis has been done within the **Silicon Photomultiplier and Scintillating Fibre based Compton Camera (SiFi-CC)** project [66]. The aim of the project is to build a novel PG detector for *in vivo* proton therapy monitoring. The detector can be set up in one of the two modalities: as a Compton camera (CC) or as a coded-mask (CM) camera. The first one allows in principle for a reconstruction of a three-dimensional PG distribution, while the other one is limited to one or two dimensions, depending on the shape of the mask and detector properties.

The CM option requires less material, less data acquisition channels and involves a simpler image reconstruction algorithm. Hence, the detector in the CM modality was assembled and tested in the first place, and it is the focus of this thesis. In this chapter, the detector concept and design are described, along with its previous versions and optimisation of the components.

## 2.1 DETECTOR MODALITIES

### 2.1.1 Compton camera

A Compton camera is a type of radiation detector that exploits Compton scattering. Among all approaches to prompt-gamma imaging (PGI), it is the only detector that allows obtaining a 3D spatial distribution of the observed radiation source with a single device [67]. Originally, CCs were applied in astrophysics [68], later they were also optimised for use in medical applications [69], characterisation of nuclear waste [70] and homeland security [71]. Typically, a CC is composed of two detector modules: a scatterer, where a gamma is Compton-scattered and the recoil electron is absorbed, and an absorber, where the scattered gamma is absorbed. The two modules register the positions of the interaction points and energy of the electron and the scattered photon in coincidence. Having this information and knowing the kinematics of Compton scattering (Equation 2), one can reconstruct a cone of possible directions of the primary gamma.

$$\theta = \arccos \left( 1 + m_e c^2 \left( \frac{1}{E_{\gamma'} + E_e} - \frac{1}{E_{\gamma'}} \right) \right). \quad (2)$$

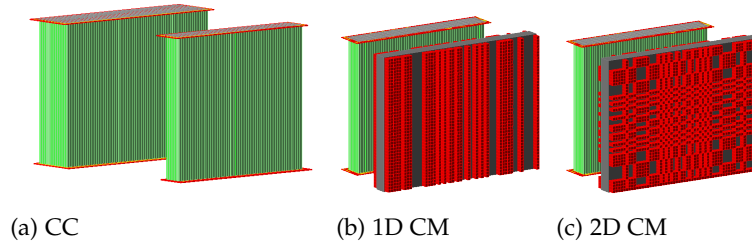


Figure 2.1: Illustration of the SiFi detector modalities.

There,  $E_{\gamma'}$  is the energy of the scattered gamma,  $E_e$  is the energy of the recoil electron,  $E_{\gamma'} + E_e$  is the energy of the primary gamma, and  $\theta$  is the angle between the direction of the primary and the scattered gamma, which defines the cone. Having multiple such cones, a spatial distribution of the source can be retrieved by using an appropriate image reconstruction algorithm.

There are various approaches to the design of CCs for medical imaging. Multiple scatterer modules were proposed in [72, 73]. In the latter study, the absorber was built of scintillation crystals, while the scatterers were in form of silicon detectors. Kurosawa et al. proposed a camera in which Compton scattering is induced in a gas chamber [74]. There, the authors present the first PG distribution after proton irradiation that was measured with a CC. Draeger et al. performed an experiment in clinical conditions, demonstrating feasibility of three-dimensional imaging with a CC [43]; the detector modules were based on CdZnTe crystals. Another solution tested under proton beam conditions are several generations of the MACACO detector [75, 76]. There, the detector modules are made of LaBr<sub>3</sub> and LYSO scintillation crystals. In [42], the authors report on a CC with 3D position sensitivity, in which the detector modules are composed of multiple cubical Ce:GAGG crystals; the detector was tested under proton beam conditions.

Our approach to CC design (see Figure 2.1a) involves constructing both detection modules out of thin scintillating fibres, read out at both ends by silicon photomultipliers (SiPMs) (a detailed description of the design can be found in Section 2.3.1). The high granularity of the detection modules ensures a low pile-up probability. Moreover, two out of three coordinates of the particle interaction point can be retrieved directly if one identifies the fibre in which the interaction took place, provided that the readout channels are independent. The third coordinate of the interaction point is reconstructed from the charge ratio of the signals registered at both ends of the fibre. The fibres are made of a dense, high-Z material (LYSO:Ce,Ca), to ensure good detection efficiency of PGs.

In the further parts of this thesis, we use the following nomenclature: we refer to the position of the interaction point in the detector as the "hit position", and by "hit fibre" we mean the fibre in which the interaction took place.

### 2.1.2 Coded mask

A CM camera is an extension of a pinhole camera concept [77]. The pinhole camera involves a black, light-tight box with a small hole in one of its walls to obtain an image. This simple concept has certain advantages over lens-based optics: no linear distortion, wide angular field of view, and arbitrary field depth [77]. A serious limitation of this detection method is that the vast part of the light is lost, so a significant time of measurement is needed to collect enough data.

To increase the statistics and thus shorten the measurement time, a passive collimator in the form of multiple holes or slits (named coded mask or coded aperture) with known pattern can be used instead of a single pinhole. The collimator modifies the image registered on the detector plane in a known and characteristic way. Then, an appropriate algorithm is applied to reconstruct an actual image from the raw detector response. The CM imaging technique was proposed in [78] and was originally applied in astrophysics to image far-field, point sources [79]. Examples



of image reconstruction algorithms for CM imaging are maximum-likelihood expectation maximisation (MLEM) [80, 81], OSEM [82, 83], and FISTA [84, 53]. The MLEM was used in our case (see Section 4.7.1). A class of masks that is widely perceived as optimal for CM imaging is a Uniformly Redundant Array (URA), an overview of which can be found in [85]. These masks are built out of square pixels, and the pattern is constructed based on prime numbers. One of the subgroups of this class is a modified uniformly redundant array (MURA) CM pattern, proposed in [86]. This pattern ensures that the noise terms in the reconstructed image are independent of the structure of the image source [86]. We have chosen the MURA pattern (more details of the design in Section 2.3.4) for our measurements, see Figures 2.1b and 2.1c.

A CM gamma camera for near-field applications, in particular proton therapy monitoring, has been studied via simulations by Sun et al. [53] and experimentally by the SiFi-CC group [54]. In the SiFi-CC project, the CM is one of the two modalities in which the detector can be set up, the other one being the CC. The CM imaging requires only one detection module, hence it was the first modality tested in proton beam conditions. Description of those tests constitutes a major part of this thesis. Once the detector is reconfigured to the CC modality, the detection module used in the CM one will serve as a scatterer.

## 2.2 EARLIER STUDIES AND VERSIONS OF THE DETECTOR

### 2.2.1 Optimisation of fibre material and wrapping

On the way to find an optimal detector design and materials, an extensive experimental study was conducted<sup>1</sup> [87, 88]. There, various fibre materials and wrappings were compared in terms of energy resolution, position resolution, timing resolution, attenuation length, and light collection. The first two parameters are discussed here in more detail, as they were the most crucial in the context of the research described in this thesis.

Let us define the charge collected by the SiPMs on both fibre sides ( $L$ ,  $R$ ) as  $Q_L$  and  $Q_R$ , respectively. The energy deposited in the fibre depends primarily on  $\sqrt{Q_L Q_R}$ , while the hit position along the fibre depends mainly on  $\ln(\sqrt{Q_L}/Q_R)$ . Based on these observations, position and energy calibration can be performed - for this purpose, two light attenuation models were developed, one of them considering also the light reflected in the fibre [87]. The calibration is based on a series of measurements with an electronically collimated, radioactive source, which is placed in different positions along the fibre. For each source position, the charges collected by the SiPMs on both fibre sides are registered. Using the energy and position calibration, one can determine the resolutions, which are defined as follows:

- The energy resolution is the relative width of the reconstructed 511 keV peak:  $\sigma/\mu$ , where  $\sigma$  is the standard deviation of the Gaussian fit, and  $\mu$  is its mean position.

<sup>1</sup> The study was conducted by K. Rusiecka.

- The position resolution is the full width at half maximum of the distribution of reconstructed positions.

In this study, the SiPMs coupled to the fibre had approximately 9 times larger surface than the fibre end. The fibre ends were positioned centrally with respect to both SiPMs.

The conclusion from the study of fibre properties was that the fibre that provides the best tradeoff between position and energy resolution is a LYSO:Ce fibre wrapped in Al foil, the shiny side facing the fibre surface. The dimensions of the fibres compared in that study were  $1 \times 1 \times 100 \text{ mm}^3$ . The obtained parameters were: energy resolution 8.56% at 511 keV, position resolution 32 mm.

### 2.2.2 Optimisation of the detector setup geometry

Another study performed within the SiFi-CC group, which was the basis for the detector construction, was a Geant4 simulation study<sup>2</sup>, where the geometry of the experimental setup was optimised [89]. The optimised parameters were:

1. the distance between the radiation source and the first module: 150 mm
2. the distance between the two CC modules: 120 mm
3. the number of layers of the first CC module: 16
4. the number of layers of the second CC module: 36

Using the optimised parameters, the detector performance in such configuration was evaluated. It was found that the detector is able to detect a 5-mm shift of the range of proton beam with a resolution of 2 mm at the statistics corresponding to  $5 \times 10^8$  protons. The detector imaging sensitivity in this configuration is  $(5.58 \pm 0.01) \times 10^{-5}$ .

### 2.2.3 Small-scale prototype of a detector module

The studies described above formed the basis for the construction of a small-scale prototype of a detector module (Figure 2.2). It consisted of four layers of 16 fibres each, of the properties determined as optimal in the fibre study (see Section 2.2.1). All fibres were coupled at both ends to SiPMs [90] with a matching active surface size ( $1 \times 1 \text{ mm}^2$ ). One fibre end was coupled to one SiPM (so-called 1-to-1 coupling), to ensure direct fibre identification: if the SiPMs at both ends of a given fibre register a signal, it is assumed that this fibre was hit. Optical pads made of Elastasil RT 604 [91] served as a coupling between the fibre end and the SiPM surface. The SiPMs were read out by a Caen DT5742 digitiser [92] (16 SiPMs at a time, due to the limited number of DAQ channels). The prototype was calibrated fibre-by-fibre, in the same way as the single fibres in Section 2.2.1. The energy and position resolutions obtained were 10.58% and 91.49 mm, respectively [88]. Such position resolution was not sufficient for the purpose of determining the hit position along the fibre, and significantly worse than in the single fibres study. The

<sup>2</sup> The simulation study was performed by J. Kasper.



Figure 2.2: Small-scale prototype of the SiFi-CC detector module. Left panel: top view, red printed circuit boards (PCBs) housing the SiPMs visible; right panel: side view, fibre stack arrangement visible.

main difference between the small-scale prototype setup and the single fibre setup (Section 2.2.1) was the larger SiPM size in the latter, which allowed for collection of light scattered at larger angles. This light undergoes multiple internal reflections and thus experiences a larger optical path, being strongly attenuated. Hence, it is mostly responsible for the position sensitivity and restricting the scattering angle leads to worse position resolution.

This issue was addressed in another experiment, using readout based on light sharing, also described in [88]. The fibres were read out by Philips Power Tile digital sensors [93], which, contrary to the SiPMs of the active surface of  $1 \times 1 \text{ mm}^2$ , allowed the light from each fibre to spread and be registered by several pixels of the photosensor. Then, the centre-of-gravity method was employed to determine the two coordinates of the interaction point in the plane of the fibre ends. Position and energy calibration procedures were performed analogously as for the 1-to-1 coupled setup, and the following values were obtained: an energy resolution of 7.73 %, and a position resolution 34.28 mm. Both the resolutions were significantly better than in the 1-to-1 coupled setup. This supported the conclusion that collecting the light scattered at larger angles leads to better position resolution; moreover, it improves the energy resolution, as more scintillation photons are registered.

Based on the prototype study, conclusions were drawn for the full-size setup. To improve the light collection, which is connected to the energy resolution, we decided to increase the fibre cross section up to  $1.94 \times 1.94 \text{ mm}^2$ . In order to improve position resolution, we used 4-to-1 coupling between the fibres and SiPMs, as this enables collection of light scattered at large angles (SiPM area is larger than fibre area, like in the single fibre studies described in Section 2.2.1). The cost of this modification, however, is the necessity to decode fibre hits from SiPM hits, which is not as straightforward as in the 1-to-1 coupling case. Another argument for the transition to 4-to-1 coupling was a limited budget, and such a geometry requires four times less data acquisition (DAQ) channels than the 1-to-1 geometry.

#### 2.2.4 Small-scale prototype with a CM

The small-scale prototype was also incorporated into a CM imaging setup and tested under laboratory conditions to demonstrate the proof of principle for the near-field CM application. The findings are reported in [54]. The fibre matrix was

rearranged into two layers, 32 fibres each. Digital SiPMs by Philips Digital Photon Counting were used for readout and the Hyperion system [94] served as the DAQ. With this setup and a 1D CM (see Figure 2.3), the images for point-like radioactive sources were reconstructed with a mean standard deviation of 1.14(18) mm.

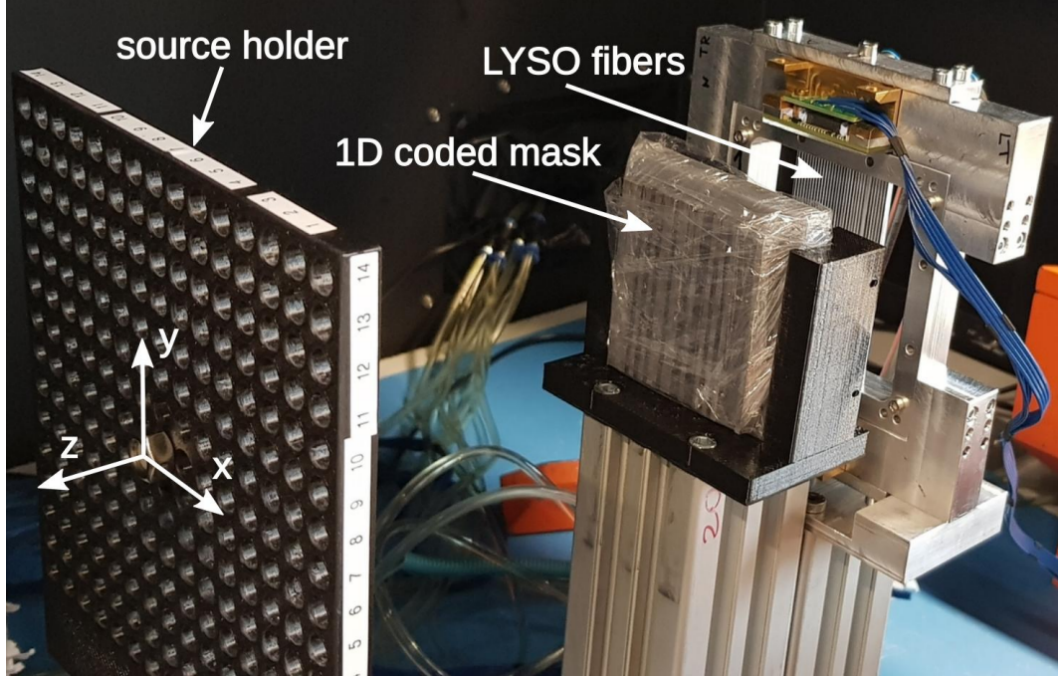


Figure 2.3: Experimental setup for 1D measurements with the small-scale prototype of a CM gamma camera. Adapted from [54].

The mean reconstructed positions show a consistent offset of about 1.03(14) mm, which is caused by a systematic effect due to the limited alignment accuracy of the setup elements.

A further demonstration of the proof of principle for the CM approach to PGI was a simulation study of a full-scale setup, also described in [54]. It yielded a mean distal fall-off position (DFP) determination precision of 0.72 mm. This value was obtained for the beam energy range of 85.9-107.9 MeV, with the statistics of  $10^8$  protons. The image reconstruction algorithm used was MLEM.

The conclusion from both the experimental and the simulation study was that the CM imaging is a feasible option for proton therapy monitoring, and the precision of the method is comparable with the precision of knife-edge-shaped and multi-slit cameras - other solutions being investigated for this purpose (see 1.2.6.2).

### 2.3 DETECTOR COMPONENTS

In the following, the building blocks of the first full-scale detector module are presented.

### 2.3.1 Scintillators

The active part of the detector module is a block of scintillating fibres, stacked in 7 layers, 55 fibres each, 385 fibres in total. We refer to a fibre either by its absolute ID (0-384), as indicated in the bottom plot of Figure 2.4, or by its address. The address requires three numbers instead of one, but has the benefit of being more informative about the actual position of a given fibre within the fibre stack. The address is comprised of module  $m$ , layer  $l$ , and fibre  $f$ , which are defined as follows:

1. module: ID of the detector module; 0 - scatterer, 1 - absorber. In the course of this thesis, as we are using only one module (the scatterer), thus the module ID is always 0.
2. layer: ID of the fibre layer, increasing with distance from the radioactive source (along the  $z$  axis); range 0-6.
3. fibre: fibre number within a layer, range: 0-54. A group of fibres with the same value of the fibre number is called a *column*.

The structure of the fibre block (top view) is marked in red in Figure 2.4. The dimensions of a single scatterer pixel (i.e. a bare, unwrapped fibre) are  $1.94 \times 1.94 \times 100 \text{ mm}^3$ , the fibres are stacked together so that the long walls touch each other. Each fibre is wrapped in an aluminium foil type 1060 [95],  $30 \text{ }\mu\text{m}$  thick. The pitch between subsequent pixels is 2 mm in both  $x$  and  $z$  directions ( $x$  is the dimension along a single layer,  $z$  is the one across the layers (see Figure 2.4), with the exception of the gaps after each 8 fibre columns: there, the pitch is  $100 \text{ }\mu\text{m}$  larger, which comes from the requirement to match the distance between the borders of SiPMs from two different arrays. The remaining space between the fibres after wrapping with the foil was filled with an ESR foil ( $0.085 \text{ mm}$  thick) and a glue layer ( $0.015 \text{ mm}$  thick) to match the required pitch. The fibres are made of LYSO:Ce,Ca. The entire stack of fibres was manufactured by Taiwan Applied Crystals [96]. The LYSO:Ce,Ca material and the wrapping material were chosen based on a previous study within the SiFi-CC project; see Section 2.2.1.

### 2.3.2 SiPM arrays

In this study, Broadcom AFBR-S4N44P164M  $4 \times 4$  SiPM arrays [97] were used. They were coupled to fibre ends on both sides of the scintillation fibre stacks. The size of each SiPM pixel was  $4 \times 4 \text{ mm}^2$  (with the photosensitive area of  $3.72 \times 3.62 \text{ mm}^2$ ), so one SiPM was coupled to four fibre ends. There were two custom-made PCBs, one on the top side of the fibre stack and one on the bottom side. Each PCB housed 7 SiPM arrays arranged in a row. The geometry details of the fibre stack are presented in Figure 2.4. There, in the bottom panel, one can see that the SiPM arrays are shifted with respect to one another by half a pitch in the diagonal direction. Such an arrangement is advantageous in the process of identification of the fibre that generated the signal: each fibre is coupled to a unique pair of SiPMs. If there is an event in which only those two SiPMs registered a signal, one can immediately deduce which fibre was active.



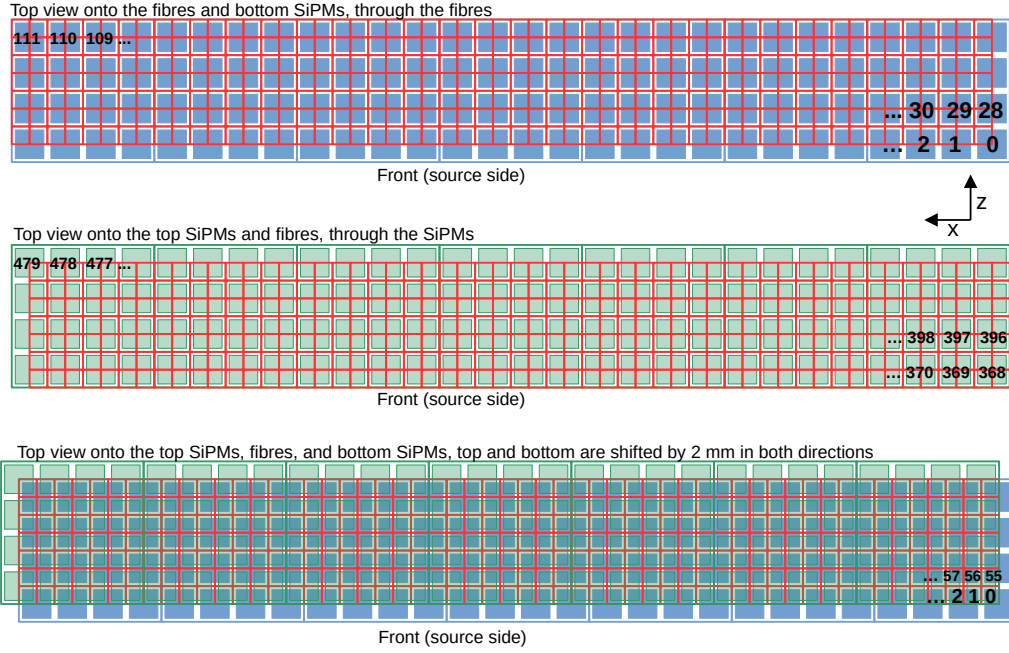


Figure 2.4: Geometry of the fibre stack constituting the sensitive part of the constructed detection module. Top panel: the bottom SiPM array with respect to the fibres (bottom SiPMs in blue, fibre contours in red), with bottom SiPMs numbering scheme; middle panel: the top SiPM array with respect to the fibres (top SiPMs in green, fibre contours in red), with top SiPMs numbering scheme; bottom panel: both the top and bottom SiPM arrays and the fibres, with fibres numbering scheme. The bottom panel illustrates the architecture of 4-to-1 coupling - 4 fibres coupled to one SiPM on each side, with one SiPM board shifted by  $\frac{1}{2}$  of a SiPM pitch with respect to the other SiPM board, in both  $x$  and  $z$  directions.

### 2.3.3 Silicon rasters

In a previous study [87], several types of coupling between fibre ends and SiPMs were examined and it was concluded that the coupling that provides both good light transmission and stability over time are optical pads made of transparent silicon or equivalent material. Thus, in the present setup, we used 0.5 mm thick aluminium rasters filled with silicon material Elastosil RT 604 [91] (see Figure 2.5). The rasters were placed between the fibre ends and the SiPM arrays. The openings in rasters match exactly the SiPM borders, to reduce inter-SiPM crosstalk.

### 2.3.4 Masks

The coded mask is the MURA pattern of the 467th order. The 2D mask (Figure 2.1c) is made up of 57 central pixels from the entire array horizontally and 45 central pixels vertically. The 1D mask (Figure 2.1b) has the same dimensions, but the central row pattern is repeated over the 45 vertical pixel rows. Ensuring opacity for PG is nontrivial, thus the PG collimators are usually built out of thick, high- $Z$  materials. In our case, the opaque part of the mask is made of 20-mm-thick

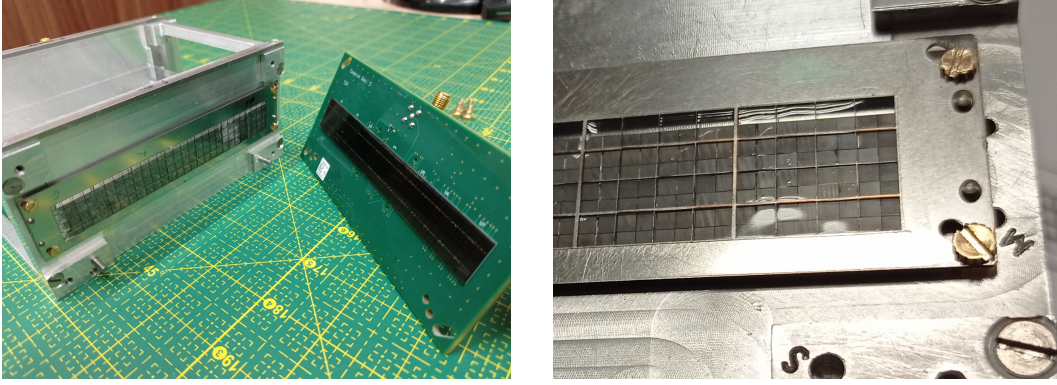


Figure 2.5: Left panel: the fibre stack with the attached optical-interface raster visible on the left, and the SiPM-housing PCB visible on the right; right panel: zoom on the raster.

tungsten. A 3D printed mould with the mask pattern, made of 3D Jake Aqua Clear resin [98], was designed as a mask skeleton. The mould is 13 mm thick and has 10-mm-deep holes for the pixels that should be filled with mask material. The resin is a low-Z material, so it can be treated as approximately transparent for the high-energy gammas. The raster is filled with removable tungsten rods of size  $2.26 \times 2.26 \times 20 \text{ mm}^3$ , building the opaque pixels. Due to this design, the mask can be easily reconfigurable. When the mask is put vertically, it has to be supported on the front side by an additional thin, removable sheet of polymethyl methacrylate (PMMA) so that the tungsten rods do not slide out.

## 2.4 FRONT-END ELECTRONICS AND DATA ACQUISITION SYSTEM

A front-end electronics (FEE) and DAQ system suitable for both modes (CC and CM) of the SiFi-CC detector should preferably have the following features:

- dead time not larger than a few  $\mu\text{s}$
- independent processing of data from each channel
- programmable coincidence scheme (allowing for channel-to-channel coincidences)
- scalability.

In order to find the optimal system, after a thorough market survey, we have selected several DAQ systems that meet at least part of the criteria listed above. Those were: A5202, DT5742 (as a reference only), KLauS6b, TOFPET2c, Twin-Peaks+TRB5sc. Their properties were investigated experimentally in a comparative manner to select the optimal DAQ system for the SiFi-CC project.<sup>3</sup> The methodology, results and conclusions from these tests are described in detail in this section, and the major points have been published in [99].

<sup>3</sup> The DAQ comparison study was done by the author of this thesis in collaboration with M. L. Wong and they contributed equally to the presented work.

### 2.4.1 *SiPM readout systems*

#### 2.4.1.1 *A5202*

FERS-5200 [100] is a scalable readout system for various detector types. The A5202 [101] (see Figure 2.6a) is a 13-bit, 64-channel unit of this system, designed for SiPM readout. The core parts of such a unit are two 32-channel Citiroc-1A application-specific integrated circuits (ASICs) [102]. The ASIC can operate in several modes, depending on the use case:

- Counting mode: the system counts self-triggers of every channel separately. The maximum counting rate is 20 Mcps. It is the fastest of all modes, however, no energy or time information is provided.
- Timing mode: time stamps in each channel are registered, along with time-over-threshold, from which an approximate information on the pulse amplitude (and thus energy) can be extracted. The timing resolution in this mode is about 250 ps RMS. The acquisition is performed in packets - a packet is filled until it reaches a programmed size, then it is read out.
- Spectroscopy mode: optimised for energy measurement. The energy is retrieved from the pulse amplitude. This mode features a global trigger: once the trigger condition is met, the analog-to-digital converter (ADC) conversion starts in all channels. The cost of accurate energy information is a significant dead time: 10  $\mu$ s due to conversion.
- Spectroscopy and timing mode: combines the two preceding modes.

In this study, mainly the spectroscopy mode was used, except for the timing properties test, where we made use of the spectroscopy and timing mode. A major advantage of this system is the moderately flexible coincidence scheme, allowing for precise selection of the events of interest (e.g. channel-to-channel coincidences). However, the channel numbers that can be matched are hard-coded (0 & 32, 1 & 33 etc.) which requires appropriate matching of physical channels to ASIC channels, only then this feature can be exploited. Another advantage of the system is a tunable gain, with two ranges available: high gain and low gain. Each of them has 64 steps. The setup comes with the Janus software, one of its convenient features being the live plotting of the collected spectra. Up to 16 A5202 units can be daisy-chained, larger numbers of channels require the use of a data concentrator DT5215 [103], to which up to 128 A5202 units can be connected.

#### 2.4.1.2 *DT5742*

The DT5742 [92] (see Figure 2.6b) is a desktop-form digitiser, its basic mode of operation is waveform recording. It offers 16 input channels and one channel for external trigger, 12-bit ADC and 5 GS/s sampling frequency. The device is based on the DRS4 switched capacitor array chip [104]. The maximum range of the signal amplitude is 1 Vpp, but also 2 Vpp range is available on demand at the time of ordering. The user can select from 4 available frequencies: 5 GHz, 2.5 GHz, 1 GHz, and 0.75 GHz. The acquisition window is always 1024 samples. Once the trigger



condition is met, the ADC conversion starts for all channels, causing dead time of 110  $\mu$ s or 181  $\mu$ s, depending on whether the trigger channel is also digitised. In our studies, we used external trigger, but other options are also available (software trigger, self-trigger, low-latency trigger). Due to limited scaling options, the device was used only as a reference. It is nevertheless a good solution for applications requiring full waveforms, e.g. for detecting pile-ups or noise or examining signal shape. An earlier performance study of the DT5742 can be found in [105].

#### 2.4.1.3 *KLauS6b*

The KLauS6b (see Figure 2.6c) is an ASIC originally prepared for the Analogue Hadronic Calorimeter (AHCAL) [106] and ScECAL [107] within the CALICE [108] [109] collaboration. It is manufactured in UMC 180 nm CMOS technology. It is designed to operate with SiPMs with high density of cells. Such SiPMs feature a high dynamic range, but a low intrinsic gain of the order of  $10^5$ . KLauS6b can be either auto- or externally triggered. There are 36 channels per unit, with selectable ADC precision of 10 or 12 bits. There are two charge integration branches, high or low gain. Each branch consists of a passive integrating circuit and a low-pass filter. The charge information is conveyed by the amplitude of the output signal from either of the branches [110]. One can select the preferred branch in software, then only output from this branch is digitised. The available interfaces to send data off the chip are I<sup>2</sup>C (up to 20 Mbit/s) or LVDS (up to 160 Mbit/s). The main dead-time contributions are the front-end processing time and the ADC conversion time, which are estimated by the producer to be below 800 ns [110]. The acquisition software, operating on Linux, is provided by the producer.

#### 2.4.1.4 *TOFPET2c*

The TOFPET2c (see Figure 2.6d) is a SiPM readout and digitisation system [111]. It has been optimised for time-of-flight (TOF) measurements with PET. Its main advantages are low power consumption and low noise. The system consists of a FEB/A board housing an ASIC, an interface board FEB/I, FEB/D (which manages powering, configuration and synchronisation of the ASICs) and a clock board (which, together with the FEB/D, allows for coincidence detection). The ASIC is produced in the CMOS 110 nm technology. The basic unit (the ASIC) has 64 channels with independent readout. Each channel features a quad-buffered TDC and a charge integrating 10-bit ADC. The dynamic range declared by the producer is 1500 pC. Up to 16 ASIC units can be connected to a front-end board (FEB/D) [112] via interface boards (FEB/I). The system can be scaled up further by plugging multiple FEB/Ds to a Clock&Trigger unit. The data are transferred via an optical link to a Peripheral Component Interconnect Express (PCIe) data acquisition board and then to a PC. A Linux-operated acquisition software, provided by the PETSys company, is used to manage this process. The system is a complete product that is commercially available and can be used off-the-shelf.

#### 2.4.1.5 *TwinPeaks+TRB5sc*

This readout system (see Figure 2.6e) comprises a few devices: TwinPeaks [113], TRB5sc [114], and TRB3 [115]. The first one is an add-on board specially devel-

oped for the DESPEC experiment at GSI/FAIR [116]. It is a high-resolution charge-to-time amplifier. It is connected to TRB5sc, which features an ECP5 FPGA that can perform high-resolution TDC conversion. Multiple sets of TwinPeaks+TRB5sc boards can be connected via the TrbNet [117] protocol to TRB3, in order to build a scalable system of a tree-like structure. The TRB3 motherboard includes a trigger system that can send a timing signal to all connected boards, collect data recorded by them, and transfer the data to event-building software. There are 16 channels per TwinPeaks board, with ADC precision of 8 bits. The system comes with Linux-operated, custom software, DABC [118].

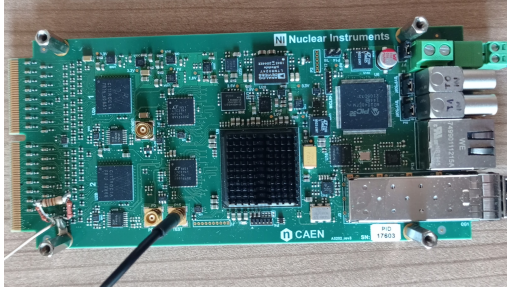
#### 2.4.2 Experimental setup

We designed and constructed two setups to test the performance of the readout systems. The first setup involved a bunch of 64 LYSO:Ce,Ca fibres of size  $1.28 \times 1.28 \times 100 \text{ mm}^3$  each, produced and stacked by Taiwan Applied Crystals [96] in 4 layers, 16 fibres per layer. Each fibre was coupled at both ends to a pair of AFBR-S4K11C0125B SiPMs [90] (formerly PM1125-WB produced by KETEK GmbH), which were read out by the tested readout system. A radioactive  $^{22}\text{Na}$  source was placed at half the length of the fibre stack and another LYSO:Ce crystal was placed opposite to the fibre stack as a reference (Figure 2.7a). The only registered signals were the ones in coincidence with the reference crystal, forming the electronic collimation setup similar to the one in [119]. The other setup used for readout systems testing was an SiPM-like pulse generator (Figure 2.7b), consisting of a 81160A Pulse Function Arbitrary Generator [120] and either a 33 pF or a 600 pF capacitor (depending on the readout system).

#### 2.4.3 Performance metrics

The readout systems were compared in terms of five major features: energy resolution, dead time, dynamic range, efficiency, and coincidence timing resolution.

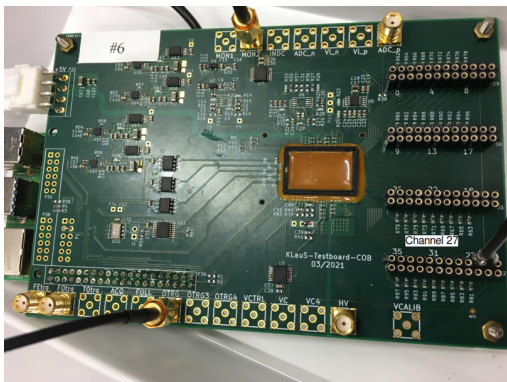
- **Energy resolution** The QDC or ADC (depending on the readout system) spectra were recorded with a  $^{22}\text{Na}$  source (Figure 2.8c). The averaged  $Q_{\text{av}}$  ( $A_{\text{av}}$ ) is defined as the geometric mean of QDCs (ADCs) recorded by the SiPMs on both sides. In the  $Q_{\text{av}}$  ( $A_{\text{av}}$ ) spectrum, the neighbourhood of the 511 keV peak was fit with a combination of a Gaussian describing the peak, and an exponent with a constant offset representing the background. The standard deviation (sigma) of the Gaussian, normalised by its mean position, defines the energy resolution (ER).
- **Dead time** We define the dead time  $\tau$  of the system as the minimum time between two subsequent registered hits. We determine this parameter by plotting a histogram of time difference between consecutive hits in one of



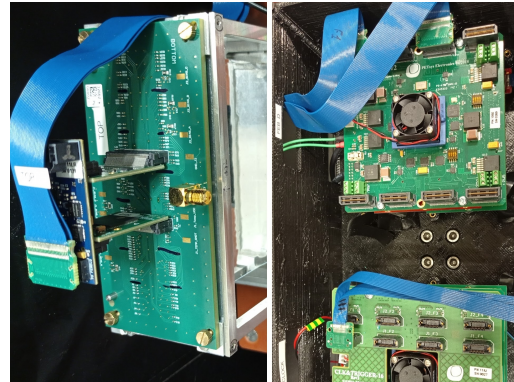
(a) A5202



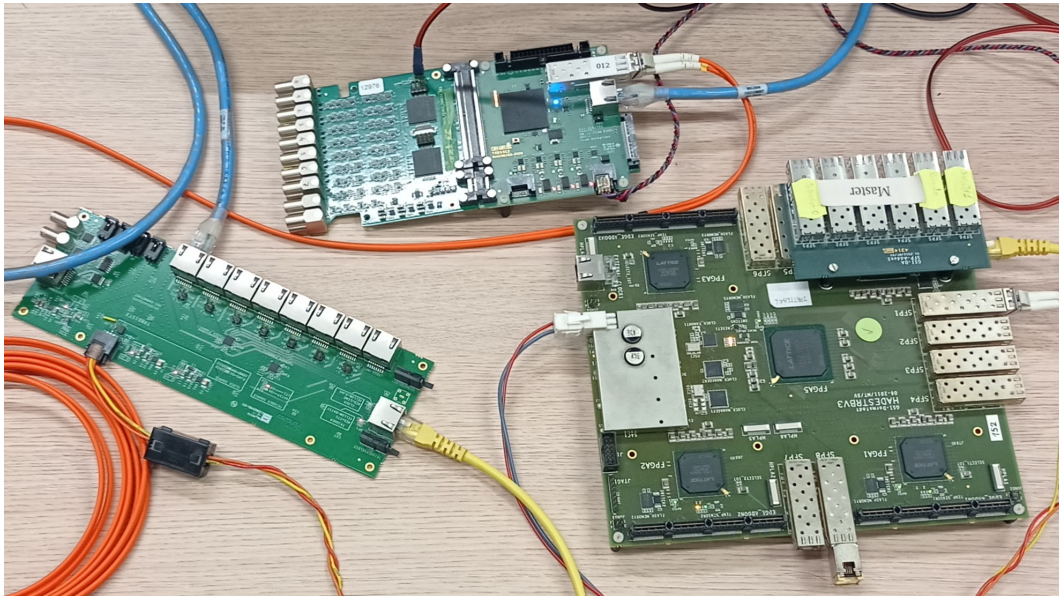
(b) DT5742



(c) KLauS6b



(d) TOFPET2c



(e) TwinPeaks+TR5Bsc

Figure 2.6: The data acquisition systems.

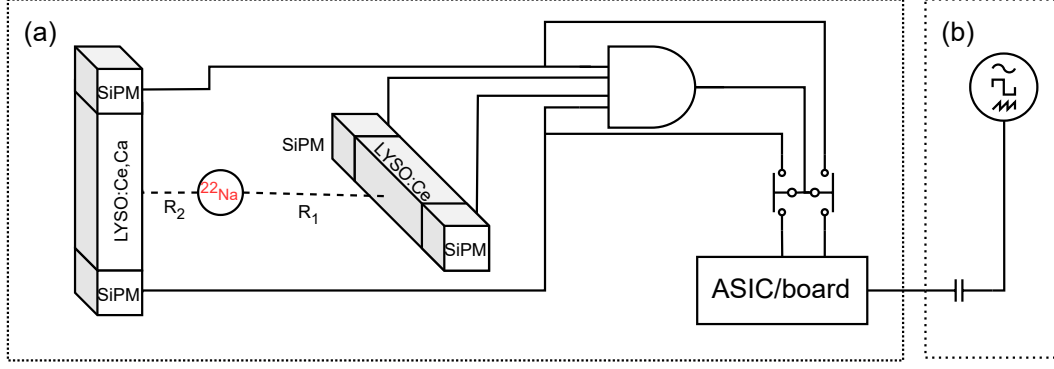


Figure 2.7: Experimental setups for DAQ comparison tests with a single fibre. Adapted from [99].

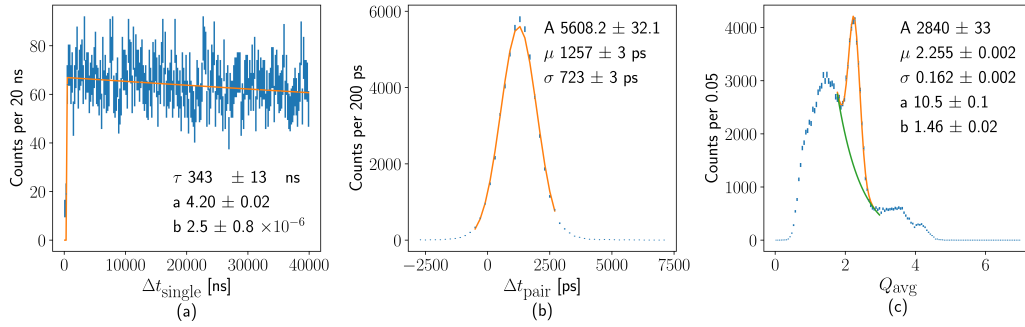


Figure 2.8: Methodology of the DAQ comparative study. Adapted from [99].

the channels and determining the width of the gap near zero, by fitting the following function:

$$y = \begin{cases} 0 & \text{if } \Delta t_{\text{single}} < \tau, \\ e^{a-b(\Delta t_{\text{single}}-\tau)} & \text{otherwise.} \end{cases} \quad (3)$$

The  $\tau$ ,  $a$  and  $b$  are the fit parameters. An example of such a fit is presented in Figure 2.8a. The dead time in this case was found to be  $0.343(13)$   $\mu\text{s}$ .

- **Dynamic range** To quantify the dynamic range of a readout system, we probe it by sending artificial pulses of different amplitudes and thus, different injected charge. We use a square pulse from a generator and put it through a capacitor, to mimic the SiPM signal shape. The experimental setup is depicted in Figure 2.7b. We plot the injected charge ( $Q_{\text{in}}$ ) vs. the response of the system (in ADC, QDC or TOT units, depending on the system; details of the procedure can be found in [99]) and look for  $Q_{\text{in}}$  value where the dependence deviates from linearity (see Figure 2.9). Such a  $Q_{\text{in}}$  value defines the upper limit of the dynamic range of the investigated system.
- **Efficiency** For efficiency measurement, we use the same setup as for dynamic range determination, but in this case the signal amplitude is fixed to 300 mV, while the frequency of the signals is gradually increased. We de-



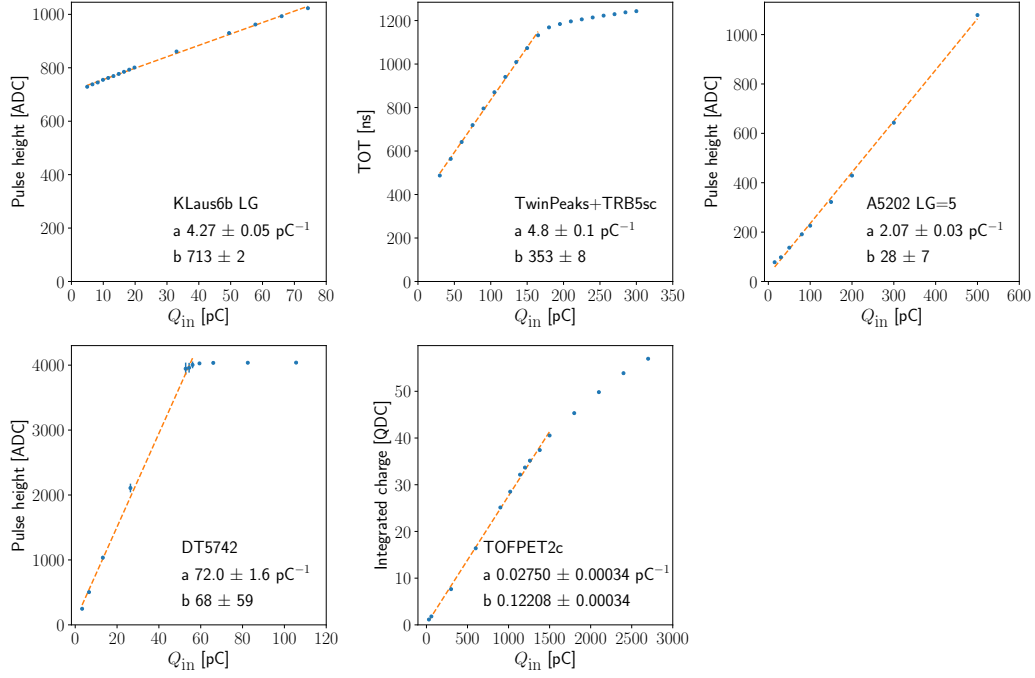


Figure 2.9: Dynamic range for all tested DAQ systems. Adapted from [99].

fine the efficiency as a ratio of the registered and injected (true) rate  $r$ . It is quantified by fitting a sigmoid:

$$\epsilon = \frac{1}{1 + e^{a+b(r-r_0)}}, \quad (4)$$

where  $r_0$  is the middle point of the falloff, while  $a$  and  $b$  are the remaining fit parameters and the efficiency limit is defined as the rate at which the efficiency curve drops to 90%.

- **Coincidence timing resolution** We define the coincidence timing resolution of the system (CTR) by plotting a time difference between the SiPM signals at both fibre ends. To diminish the walk effect, for this plot we choose only events from within  $3\sigma$  around the 511 keV peak in the  $Q_{av}$  ( $A_{av}$ ) spectrum. The coincidence timing resolution is the standard deviation of the Gaussian fit to such a plot. For this analysis, the setup in Figure 2.7a was used.

#### 2.4.4 FEE and DAQ: results

We have evaluated the readout systems in terms of the performance metrics described in Section 2.4.3. The values obtained are collected in Table 2.1 and in Figures 2.9 and 2.10.

- **Energy resolution** In terms of energy resolution, TOFPET2c performed the best: the resolution obtained with this system was 7.2(1)%. It is followed by DT5742 with 20% poorer resolution (for exact values, see Table 2.1), then A5202 (30% poorer), TwinPeaks+TRB5sc (60% poorer), and finally KLauS6b (75% poorer).

- **Dead time** Two systems presented comparably low dead time: TOFPET2c and KLauS6b ( $0.343(13) \mu\text{s}$  and  $0.352(77) \mu\text{s}$ , respectively). The next system in this category was TwinPeaks+TRB5sc with  $0.870(9) \mu\text{s}$ , followed by A5202 ( $44(4) \mu\text{s}$ ) and DT5742 ( $443(97) \mu\text{s}$ ).
- **Dynamic range** The system that performed the best in this category was again TOFPET2c with a dynamic range of up to  $1899 \text{ pC}$ . This is much higher than the next best system, A5202, for which the dynamic range was 4 times smaller. The rest of the systems' dynamic ranges were: 9 times smaller than TOFPET2c (TwinPeaks+TRB5sc), 25 times smaller (KLauS6b), and 30 times smaller (DT5742).
- **Efficiency** The efficiency plots are presented in Figure 2.10. The winner in

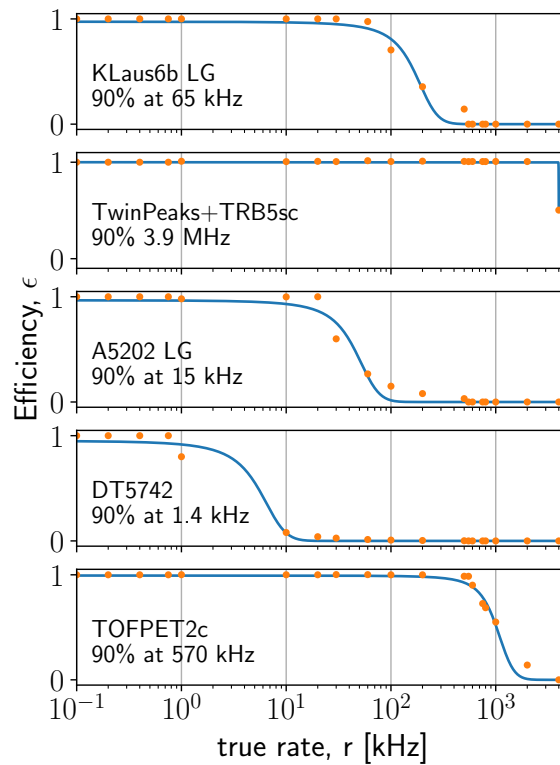


Figure 2.10: Efficiency for all tested DAQ systems. Adapted from [99].

this category was TwinPeaks+TRB5sc, which can operate with full efficiency at  $3.9 \text{ MHz}$  rate. TOFPET2c is the second-best with 7 times lower limit of full efficiency operation. It is followed by KLauS6b, A5202 and DT5742, with respectively 60 times, 260 times, and 2800 times lower maximal rate than the winner.

- **Coincidence timing resolution** The obtained coincidence timing resolution was the best for TOFPET2c:  $0.723(3) \text{ ns}$ . The next best result was obtained for DT5742 ( $1.152(1) \text{ ns}$ ), followed by KLauS6b ( $1.53(7) \text{ ns}$ ). The last ones

Table 2.1: Summary of the obtained values of performance metrics, as defined in Section 2.4.3, for the examined DAQ systems. ER - energy resolution, DR - dynamic range, Rate - rate at 90% efficiency, CTR - coincidence timing resolution, TP - TwinPeaks. The † marks the systems for which the deviation from linearity was not observed.

System	ER [%]	Dead time [ $\mu$ s]	DR [pC]	Rate [kHz]	CTR [ns]
KLauS6b	12.4(1)	0.352(77)	74.25 <sup>†</sup>	65	1.53(7)
TP+TRB5sc	11.1(13)	0.870(9)	202	3900	10.5(3)
A5202	9.4(3)	44(4)	500 <sup>†</sup>	15	3.0(2)
DT5742	8.55(4)	443(97)	62	1.4	1.152(1)
TOFPET2c	7.2(1)	0.343(13)	1899	570	0.723(3)

in this category were A5202 and TwinPeaks+TRB5sc, obtaining respectively coincidence timing resolution of 3.0(2) ns and 10.5(3) ns.

#### 2.4.5 FEE and DAQ: summary and discussion

The comparison of FEE+DAQ systems was initially just an auxiliary piece of work necessary before the purchase of an FEE+DAQ system for the SiFi-CC project. However, it evolved into a more general study, the results of which have been summarised in [99] and are valid for any application requiring the use of high-rate SiPMs readout. We selected the most promising solutions available on the market or in the development process and thoroughly examined them.

In the context of finding the DAQ system for the SiFi-CC project, TOFPET2c turned out to be optimal. It performed the best of all the systems in four out of five categories (dead time, energy resolution, dynamic range, coincidence timing resolution), being the second best choice for the last category (efficiency). However, it should be noted that none of the systems was optimised particularly for the SiFi-CC project, but for other applications (not necessarily fully consistent with our use case), so the systems' parameters varied vastly among one another, as various features were prioritised by the producers. For example, KLauS6b was optimised for high-density SiPMs, which can achieve high dynamic range at the cost of a relatively low single-pixel gain ( $10^5$ ). In our study, it obtained second-lowest dead time, which makes it a good choice for high-rate applications. A5202, even though it did not obtain competitive results in our comparison, has a very good peak separation in the single photoelectron spectrum. Thus, it can be useful when the focus of the study is in the low-intensity region and the rate is not too high. TwinPeaks+TRB5sc proved to have excellent efficiency, much higher than any other system. Thus, it is the optimal choice for applications where rate capability is crucial, and the coincidence timing resolution is not prioritised. Finally, DT5742 (which was included as a reference system, due to limited scalability options) has the second-best energy- and coincidence timing resolution. It is a good choice for applications with a small number of readout channels, where full wave-

forms are required, e.g. for SiPM performance studies or particle identification via pulse-shape discrimination.

## 2.5 SETUP ASSEMBLY

The scatterer module consists of a stack of scintillation fibres, PCBs housing SiPM arrays and silicon rasters which couple the fibre ends to the SiPM arrays. For the tests, the module was mounted in a light-tight container, which can be seen in Figure 2.11. The container is made of black polyoxymethylene (POM) of

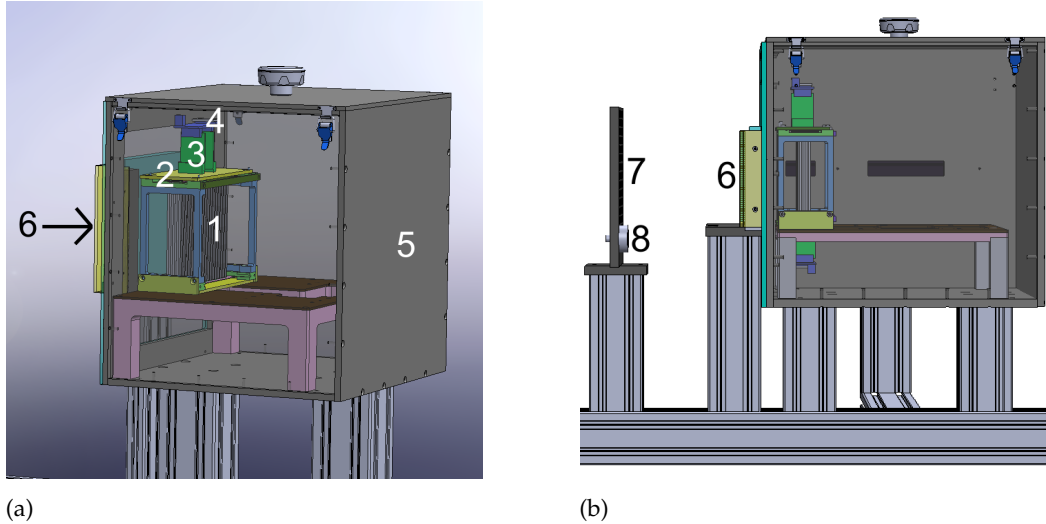


Figure 2.11: The experimental setup viewed at two different angles. (a) Fibre stack module (1, grey); SiPM PCBs (2, yellow); parts of the TOFPET2c system: FEB/A (3, green) and FEB/I (4, purple); light-tight box (5, dark grey); mask (6). (b) Side view of the experimental setup in a radioactive source-measurement configuration. Colour coding the same as in the left panel; additionally, there is the source raster (7, black) and the radioactive source (8, grey) in an example position below the setup central axis.

9 mm thickness, all the feedthroughs for cables were optically isolated with black tape. The top wall is a removable lid, for easy setup manipulation. The front wall of the container is made of black fabric [121], to minimise the scattering effect on the way to the detector. We checked the light-tightness of the container in two steps. First, by shining a strong torch onto the box from the outside and checking visually if any light leaked to the inside. After this test revealed no leaks, we took two short measurements of the SiPM signal, with the room light on and off, and compared if the registered count rate differed in the two situations. No such effect was observed, so we concluded that the container was sufficiently light-tight for our purpose. All parts of the experimental setup were mounted on a support structure, which was made of aluminium profiles with sub-millimetre positioning precision. The assembled experimental setup is presented in Figure 2.11. The height of the aluminium legs holding the light-tight box, the mask and the radioactive source raster (i.e., a raster allowing for mounting the radioactive source in different positions) were adjusted so that the central points of the setup elements are at the same level (the same position in  $y$ ) and at the same  $x$  position



(horizontal, perpendicular to the setup axis  $z$ ). The distance between the central points of the radioactive source and the mask was 170 mm, the distance between the central points of the mask and the fibre stack was 63 mm. The fully-coded field of view (FOV) resulting from the detector geometry was  $(176 \times 100) \text{ mm}^2$ . However, in the measurements described in this thesis, the analysis was restricted to FOV of  $(140 \times 100) \text{ mm}^2$ . The weight of the mask was 3 kg. The setup used in tests with the proton beam was analogous to the one for the radioactive source measurements, with the exception of a cuboidal PMMA phantom being placed instead of the radioactive source and the radioactive source raster. The geometric centre of the phantom was aligned with the central points of the mask and the fibre stack. The phantom was not placed on the aluminium support structure, but on a dedicated PMMA table instead.



## EXPERIMENTS

---

The experiments presented in this chapter, as well as the data analysis and results presented in the further chapters of this thesis, have also been partially described in [122]; the preprint has been submitted to Physics in Medicine and Biology in January 2025. The author of this thesis is also the first and corresponding author of the said preprint.

### 3.1 LABORATORY TESTS

#### 3.1.1 Calibration

##### 3.1.1.1 Position calibration along the fibre

As mentioned in the detector description (Section 2.1.1), the reconstruction of the hit position along the  $x$  and  $z$  axes of the fibre stack is performed by identifying the fibre that was hit. Along the  $y$  axis (i.e. along the fibre), determination of the hit position is more complex, as one needs to reconstruct it from charges collected by SiPMs at both fibre ends. This is based on the fact that the light collection on the SiPM depends on the point of interaction along the fibre, due to the attenuation of the scintillation light within the fibre. The procedure of  $y$ -position calibration is described in [88]. The measure of this procedure's accuracy is the position resolution along the fibre. In principle, the position along the fibre could also be determined based on the time information from both SiPMs, but the obtained time resolutions result in a position resolution of about 7 cm only, thus we discarded this method.

Before the measurements with the proton beam, we performed a preliminary study of the light attenuation along the fibre (which is connected to the position resolution). The study showed that the light attenuation (and therefore the position resolution along  $y$ ) in the present experimental setup was not sufficient, which would also impede the performance of the two-dimensional coded mask (2D CM) setup (Figure 2.1c). Thus, we decided to focus on examining the performance of the one-dimensional coded mask (1D CM) setup (Figure 2.1b). There, the fibres can be treated as pixels and the mask pattern is the same along  $y$ , so the position along  $y$  is not needed.

The  $y$ -position calibration of the detector was performed only after the proton beam measurements<sup>1</sup>. It was done by placing an electronically collimated  $^{22}\text{Na}$  source (the electronic collimation principle can be found in [119]) in different positions along the fibre (at 10 mm intervals) and registering SiPM signals from both ends of the fibre. Each measurement was 15 min long to collect enough statistics. With the electronic collimation scheme, the length of the irradiated slice of the fibre is determined by the geometry of the reference detector and source-detector

---

<sup>1</sup> The position calibration was conducted by K. Rusiecka

distances. In this case, for a single source position a fibre slice of 2.4 mm length was irradiated, which also defined the hit position uncertainty. Due to the 4-to-1 coupling between fibres and SiPMs, for a calibration measurement one needs to select only single-fibre events, i.e. those in which there was only one fibre active, i.e. with one top and one bottom SiPM active. In the data, there were also other event classes present, with multiple active fibres. The details of how they were handled can be found in Section 4.3.4. The calibration measurement was done for all fibres simultaneously; data samples representing responses of individual fibres were identified and the calibration procedure for each fibre was performed separately. The detailed calibration procedure was developed within the group during previous fibre tests and is described in [87]. A custom model of light propagation along the fibre is fit to the data. The hit position along the fibre and the energy deposit are reconstructed event-by-event, based on that model, and the charge information from SiPMs at both fibre ends. The distribution of the hit position residuals and energies yields the position and energy resolutions. From this measurement, an energy resolution of  $6.5 \pm 0.5\%$  and a position resolution of  $74 \pm 10$  mm were obtained. These values differed significantly from what was expected based on extensive tests of both single fibres and small-scale fibre stacks. The energy resolution improved, while the position resolution deteriorated, which suggests that the attenuation of optical photons in the fibres of the full-scale module was much smaller than in the previously tested fibres. After an extensive experimental survey, we identified the reason for such a change of fibre properties: the manufacturer has changed the type of the wrapping aluminium foil (8011 [123] to 1060 [95]) without any notice, when moving to thicker fibres (cross section of  $1.28 \times 1.28$  mm<sup>2</sup> to cross section of  $1.94 \times 1.94$  mm<sup>2</sup>).

The issue with position resolution was addressed in the construction of the next version of the scatterer (and the absorber for the CC mode): firstly, the aluminium foil type 8011 will be used; secondly, it was determined that covering one side of the fibre with white paint before wrapping it in the aluminium foil greatly increases the performance in terms of position resolution. Preliminary tests on single fibres<sup>2</sup> yielded very promising results: position resolution of 12 mm, and energy resolution of 8.3%. Thus, future versions of the detector will be assembled in this way.

### 3.1.1.2 Gain alignment of SiPMs

The alignment of SiPMs gains is a simplified form of energy calibration for the analysis of the 1D CM data. The SiPMs register charge in arbitrary QDC units. In order to rescale it to energy units and align the SiPMs' gains, an auxiliary measurement was done with a radioactive <sup>68</sup>Ge/<sup>68</sup>Ga source. The energy spectrum from this source contains the characteristic annihilation peak of 511 keV energy. We assumed there was no offset: zero charge corresponded to zero energy. We plotted charge spectra for all SiPMs separately (see example spectrum in Figure 3.1) and fit a Gaussian (with standard parameters  $\mu$  and  $\sigma$ ) on an exponential background in the 511 keV peak region. The mean value of the peak position for all SiPMs in QDC units was 9.563(18) a.u. The determined peak positions per SiPM were then

<sup>2</sup> The tests were conducted by K. Rusiecka and B. Pióro.

used to rescale the QDC values to energy. The energy calibration is incorporated in the low-level reconstruction (LLR) software.

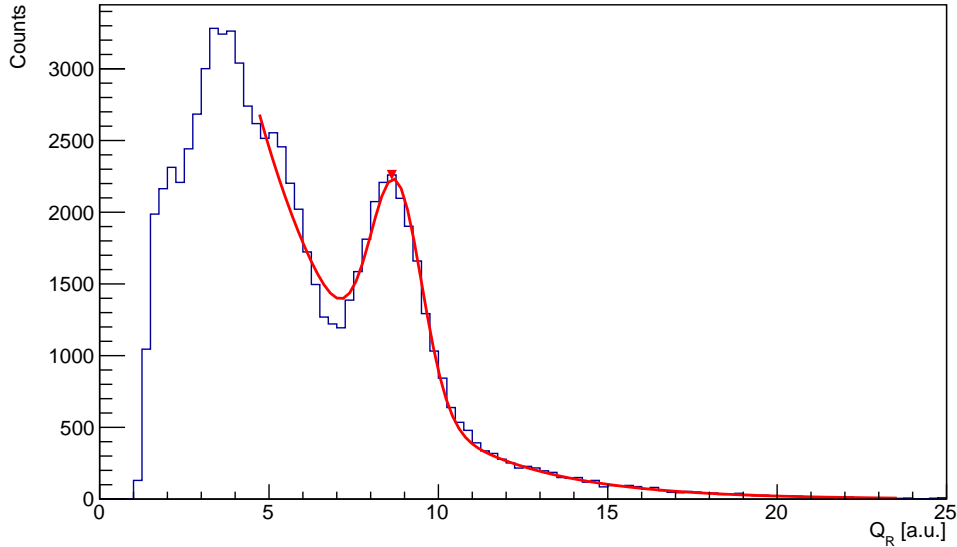


Figure 3.1: An example QDC spectrum (for SiPM 5 in layer 0 on the top side of the detector) with the fit function for gain alignment.

### 3.1.2 Dead SiPM issue

The assembly of the PCBs housing the SiPM arrays was done by an external company, that did not comply with the soldering method described by the producer in the product specification. This resulted in the fact that gradually, more and more SiPMs were losing electrical contact and became inactive. As a consequence, during all measurements involving the Broadcom SiPMs [97] described in this thesis, there were acceptance gaps present (see the IDs of the dead SiPMs in Table A.1 and the IDs of fibres that were connected to the dead SiPMs<sup>3</sup> in Table A.2). We acknowledge that such a fault of the experimental setup limits the detector performance in various aspects. Therefore, we took measures to compensate for this issue:

- as most gaps occurred on the sides, we have studied the effect of eliminating these detector parts in the analysis,
- we have adapted the simulations to the experimental conditions by filtering out the responses of the SiPMs that were dead during the experiment.

Moreover, we studied to what extent the issue of dead SiPMs deteriorates the image reconstruction quality by comparing the results obtained for full simulation (Section 5.7) with those obtained for the simulation with dead SiPMs excluded (Section 5.6).

<sup>3</sup> For simplicity, we refer to them as "dead fibres" or "dead pixels" in the further parts of the thesis.

### 3.2 MEASUREMENTS WITH A PROTON BEAM

The objective of the proton beam measurements was to evaluate the performance of the detector in the 1D CM modality. This was achieved by means of the following characterisation steps:

- The adequacy of the detector dynamic range for PG registration was evaluated and the optimal bias voltage was determined.
- The detector rate capability was assessed by performing a beam intensity scan.
- A phantom (see Section 3.2.2.2) was irradiated with beams of different energies, PG depth profiles were reconstructed and based on them, the accuracy of the image reconstruction as well as beam range retrieval capabilities were assessed.

#### 3.2.1 Conditions at Heidelberg Ion Beam Therapy Center

In January 2023, the SiFi-CC group<sup>4</sup> performed a series of tests of the scatterer module at the Heidelberg Ion Beam Therapy Center (HIT) [124, 125]. The experiments were carried out in an experimental hall equipped with a horizontal beam line. Part of the experimental hall, with the beam nozzle visible, can be seen in Figure 3.2b. The facility offers a wide set of pencil beams of variable energy, lateral beam size (so-called focus), and intensity. Several ion types are available in the facility: protons and carbon ions are used for both therapeutic and research purposes, while helium and oxygen ions are currently only exploited for research. The particles are accelerated by a combination of a linac and a synchrotron of 20 m diameter, delivered by Siemens [125]. For protons, beam energies between 47.80 MeV and 219.57 MeV are available, in 255 steps. In our tests, we exploited protons in the range of energies between 70.51 MeV and 108.15 MeV, with the focus range of 14.5-22.5 mm. We also tested a few different beam intensities:  $8 \times 10^7$  protons/s,  $6 \times 10^8$  protons/s, and  $3.2 \times 10^9$  protons/s.

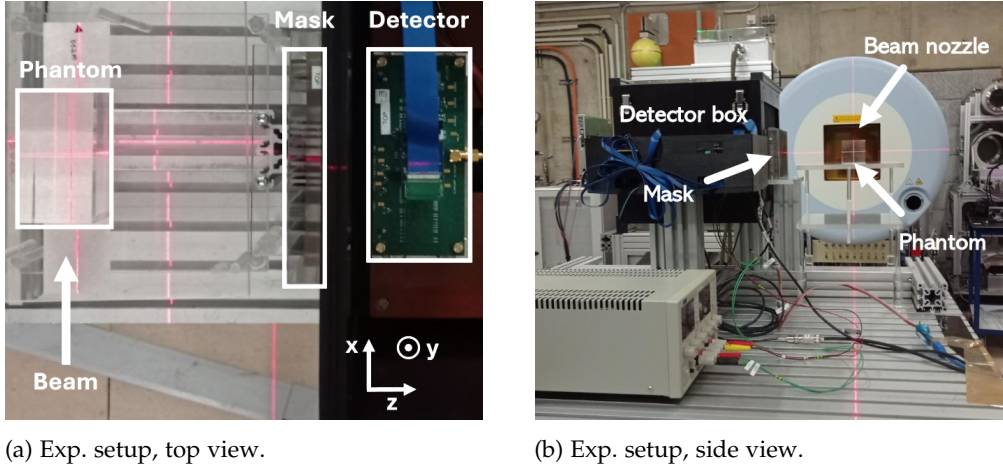
#### 3.2.2 Experimental setup

##### 3.2.2.1 Overview

The experimental setup used in the HIT measurements is presented in Figures 3.2a and 3.2b. It consisted of a PMMA phantom, 1D CM, the detector module (placed in a light-tight box), and the DAQ system.

The coded mask and the detector module are described in detail in Sections 2.3.4 and 2.3.1, the DAQ system is presented in Section 2.4.1.4, and the phantom in Section 3.2.2.2. We also summarise the detector operation in Section 3.2.2.3. The distances between the parts of the setup were: 170 mm between the phantom centre and the mask centre, and 63 mm between the mask centre and the detector centre. These distances were chosen to be as close to the optimum (found in [54]) as

<sup>4</sup> The SiFi-CC group members participating on-site: G. Farah, A. Fenger, R. Hetzel, B. Kołodziej, M. Kołodziej, K. Rusiecka, M. L. Wong, A. Wrońska



(a) Exp. setup, top view.

(b) Exp. setup, side view.

Figure 3.2: The experimental setup viewed from the top (a) and from the side (b). Key setup components are marked with white boxes or arrows and labelled.

possible, given the spatial constraints resulting from the presence of the light-tight box and the support structure. The measured mask horizontal size was 128.3 mm, while the horizontal size of the detection module was 100.6 mm.

#### 3.2.2.2 Phantom

We used a PMMA phantom of the dimensions  $50 \times 50 \times 90 \text{ mm}^3$ , of the density  $1.19 \text{ g/cm}^3$ . It was positioned centrally in the FOV of the detector, the longest phantom dimension along the beam direction. The phantom rested on a table also made of PMMA (Figure 3.2b).

#### 3.2.2.3 Detector operation

The values of parameters of the TOFPET2c DAQ system used can be found in Table A.3 in Appendix. The DAQ was operated manually with a graphical user interface (GUI). The raw data were saved on a local PC and then copied to a data server. All measurement metadata were saved in an SQL database.

The scheme of data taking with the proton beam was the following: we started the data collection with the TOFPET2c GUI, requested the beam of desired parameters from the control room, and collected data for the preset time. The measurement time was set according to the expected duration of beam delivery, to embrace the whole beam signal. The beam irradiated the phantom, the detector was placed to the side of the beam axis, in front of the phantom (see Figure 3.2a), so that the prompt gammas emitted from the phantom could be registered.

#### 3.2.2.4 Irradiation plan

The phantom irradiation was done according to the plan (presented in Figure 3.3), the exact BP positions and beam energies for the S1-S7 points (so-called beam spots) can be found in Table 3.1. The measurements were made with the highest available beam intensity ( $3.2 \times 10^9$  protons/s) and the smallest available lateral beam size at the given energy (14.5-22.5 mm). The default proton statistics was  $10^{10}$  protons per measurement, and the time of measurement was 30 s - longer

Table 3.1: Summary of measurements (runs) in the 1D CM modality. The BP position was calculated from PSTAR [126]. The runs are in a chronological order.

Beam spot	Run ID	E [MeV]	Focus [mm]	BP pos. [mm]	$N_{\text{protons}}$
S4	567	90.86	17.2	(0, 0, 56.093)	$10^{10}$
S4	568	90.86	17.2	(0, 0, 56.093)	$10^{10}$
S1	569	70.51	22.5	(0, 0, 35.63)	$10^{10}$
S2	570	81.20	19.3	(0, 0, 45.882)	$10^{10}$
S3	571	86.14	18.2	(0, 0, 50.992)	$10^{10}$
S5	575	95.40	16.4	(0, 0, 61.185)	$10^{10}$
S6	576	99.78	15.7	(0, 0, 66.269)	$10^{10}$
S7	577	108.15	14.5	(0, 0, 76.462)	$10^{10}$
S4a	578	90.86	17.2	(0, 10, 56.093)	$10^{10}$
S4b	579	90.86	17.2	(0, -10, 56.093)	$10^{10}$
S4c	580	90.86	17.2	(10, 0, 56.093)	$10^{10}$
S4d	581	90.86	17.2	(-10, 0, 56.093)	$10^{10}$
S4'	582	90.86	17.2	(0, 0, 56.093)	$10^{11}$
S2'	583	81.20	19.3	(0, 0, 45.882)	$10^{11}$
S3'	584	86.14	18.2	(0, 0, 50.992)	$10^{11}$

than the proton irradiation time, as we also wanted to register the background before and after the irradiation. The beam spots were chosen to be quite sparse, to cover a large part of the detector FOV along the beam axis, and to check if the image reconstruction performance changes with the position within the FOV. Furthermore, several measurements (S4a-d) were made for the same energy but at a different position along the  $x$  or  $y$  axes. The measurements for the beam spots S2-S4 were also repeated with 10 times larger statistics ( $10^{11}$  protons) than the rest of the measurements (and correspondingly a longer measurement time). They are marked with a prime: S2'-S4'.

### 3.2.3 Online results

Several preliminary measurements were performed to ensure the setup's operability under clinical conditions and to find optimal settings for the main measurement series, which was the performance test of the gamma camera in the 1D CM modality. They are summarised in the following sections.

#### 3.2.3.1 Rate capability

High rate capability is one of the crucial features of a PG detector for proton therapy monitoring, as described in Section 1.3.3. To study the rate capability of our detector, we performed a series of measurements for two beam energies (90.86 MeV and 108.15 MeV) and three intensities ( $I_1 = 8 \times 10^7$ ,  $I_2 = 6 \times 10^8$ , and



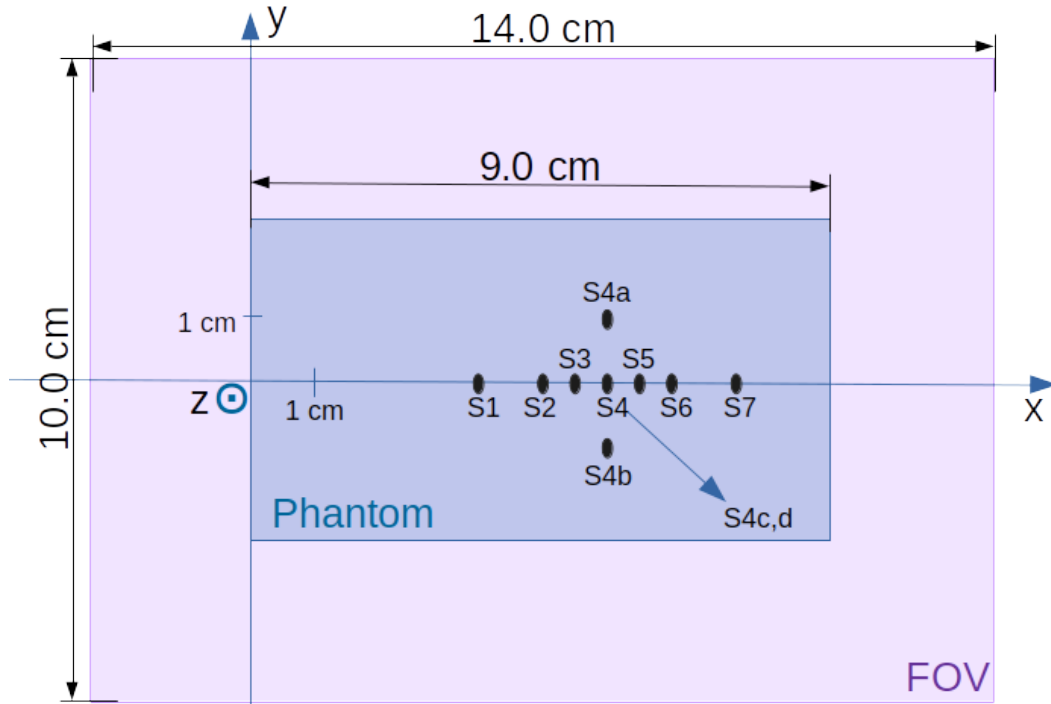


Figure 3.3: Irradiation plan of the measurements with the proton beam in HIT. The proton beam direction is along z axis, the phantom and the detector's FOV are shown.

$I_3 = 3.2 \times 10^9$  protons/s), the duration of measurements was 300 s, 60 s and 40 s respectively, to match the beam duration. Then, the data corresponding to beam (so-called spills) were separated from the background (the details of the separation procedure can be found in Section 4.2.4).

Then, we compared the number of spill counts for different beam intensities. The list of runs for this measurement can be found in Table A.4 (in the Appendix). The goal of this measurement was to check if there is a substantial decrease in the total counts when moving to higher beam intensities due to dead time. If so, it would be a sign of reaching the limit of the rate capability.

For the beam energy of 90.86 MeV, the number of spill counts for the maximum investigated intensity  $I_3$  was 6.3% lower than for the minimum intensity  $I_1$ , but the spill counts for the middle intensity  $I_2$  was 0.9% higher than for  $I_1$ . For both pairs of intensities ( $I_1$  and  $I_2$ ;  $I_1$  and  $I_3$ ) one can observe that they are not equal within statistical uncertainties (presented in Table A.4). Based on this observation, we suspect that there is a significant uncertainty associated with estimating the spill counts in this manner (not taken into account in the statistical uncertainty calculation), as the increase in the number of spill counts is not expected when increasing the intensity from  $I_1$  to  $I_2$ . Basing on the fact that the number of spill counts grows when increasing the intensity from  $I_1$  to  $I_2$ , we assume that at  $I_2$ , the rate capability limit is not reached.

A similar trend can be observed for the higher beam energy of 108.15 MeV: the number of spill counts for  $I_3$  was 7.6% lower than for  $I_1$ , while the spill counts for the middle intensity  $I_2$  was 1.4% higher than for  $I_1$ . For both beam energies, the number of counts was lower for  $I_3$  than for  $I_2$ , but it was unknown whether

the cause of such behaviour was reaching the rate capability limit. To investigate whether the limit is reached at  $I_3$ , we compared the relative increase of spill counts between the two investigated energies for  $I_2$  and  $I_3$ . A smaller increase for the higher intensity would mean that the rate capability limit is reached. For  $I_2$ , the number of spill counts for 108.15 MeV is 30% higher than for 90.86 MeV. An analogous comparison for  $I_3$  also yields a 30% increase. Thus, we concluded that the rate capability is sufficient even for the highest beam intensity used clinically on site and we performed the rest of the measurements at that intensity. However, it is not entirely clear what is the cause of the observed fluctuations of the number of spill counts when changing the beam intensity. A discussion of the detector's maximum potential rate capability is presented in Section 5.1.

### 3.2.3.2 Overvoltage scan

An overvoltage scan was performed to find the optimal bias voltage to power the SiPMs. The bias voltage is a sum of two parameters: breakdown voltage, which can vary between 32-33 V according to the producer (for simplicity, we assumed the same fixed value of 33 V for all SiPMs), and overvoltage, which we varied in a range between 4 and 14 V. This range was smaller than the maximum safe range provided by the producer (0-16 V), but we did not want to test the extreme values, assuming that they will not be optimal anyway. The differences in SiPM gain that originate, among others, from the spread of actual breakdown voltage values are corrected for later, as described in Section 3.1.1.2. The runs in this measurement series are listed in Table A.5. We compared them by inspecting the raw SiPM charge spectra (see Figure 3.4). There, one can see that for the overvoltage of 4 and 6 V, the spectra are squeezed and the structure (multiple wide peaks) at lower QDC values ( $< 10$  a.u.) is not clearly visible. The structure becomes more pronounced at 8 V overvoltage. Going even higher with overvoltage, a saturation effect is observed at higher QDC values ( $> 60$  a.u.): the spectra for 12 and 14 V overvoltage have the right-most parts of the spectrum very close to each other. Thus, the optimal bias voltage was found to be 8 V and this value was used in all the subsequent measurements. It should be noted that it was rather a rough estimate of the optimal overvoltage, sufficient for this particular measurement campaign, rather than a comprehensive study of the SiPM properties. A detailed application note on the correlations between various SiPM parameters, including overvoltage, can be found in [127].

### 3.2.4 Auxiliary measurements

Apart from the series of measurements with the coded mask, auxiliary measurements were needed for detector efficiency calculation (see Section 4.7.3), as well as for simplified energy calibration (see Section 3.1.1).

The first auxiliary measurement was a reference measurement with uniform irradiation of the detector plane. For this purpose, a linear radioactive source ( $^{68}\text{Ge}/^{68}\text{Ga}$ ) was placed horizontally in front of the detector, in the middle of its height, at a distance of 226 mm from the centre of the detection module. The coded mask was removed from the setup. The radioactive source was of cylindrical shape: 3.2 mm of external diameter and 192 mm of length. Its active part formed

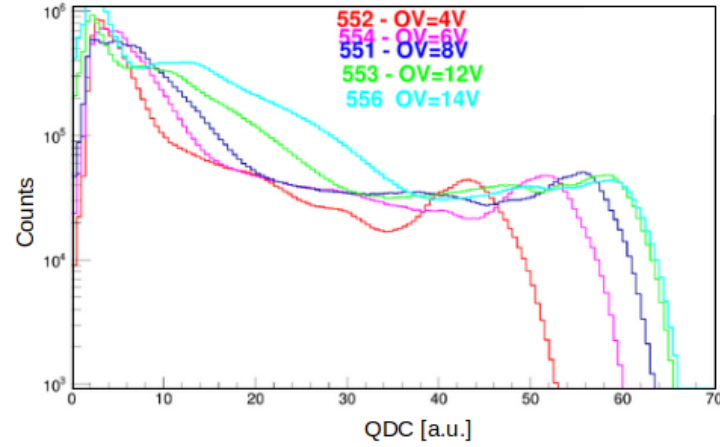


Figure 3.4: Comparison of QDC spectra for different values of overvoltage. No correction of non-linearity was applied.

a smaller cylinder located centrally inside the larger one, of 184 mm length and 1.6 mm diameter. At the time of measurement, the source activity was 10.7 MBq.

The other auxiliary measurement was the background in the absence of the beam, registered over 30 minutes after the last beam run, to exclude the background component from activation of the experimental setup parts. In such a case the detector response is due to the internal activity of the scintillation fibre material, LYSO:Ce,Ca. The main transitions in LYSO:Ce,Ca are at 307 keV, 202 keV, and 88 keV; they are usually detected in combinations [128].

The auxiliary measurements are referred to as run 596 (reference) and run 597 (background). The DAQ settings during these runs were the same as for the beam runs (see Table A.3), each of the runs lasted 300 s.



## 4.1 OVERVIEW

In this chapter, all the steps needed to obtain prompt-gamma depth profiles from raw experimental data are described in detail, along with the method of correlating those profiles with the beam range. The processing and use of data from auxiliary measurements is also presented. Figure 4.1 shows the general data processing scheme for both experimental and simulation data. Its individual steps are discussed in detail in the following sections.

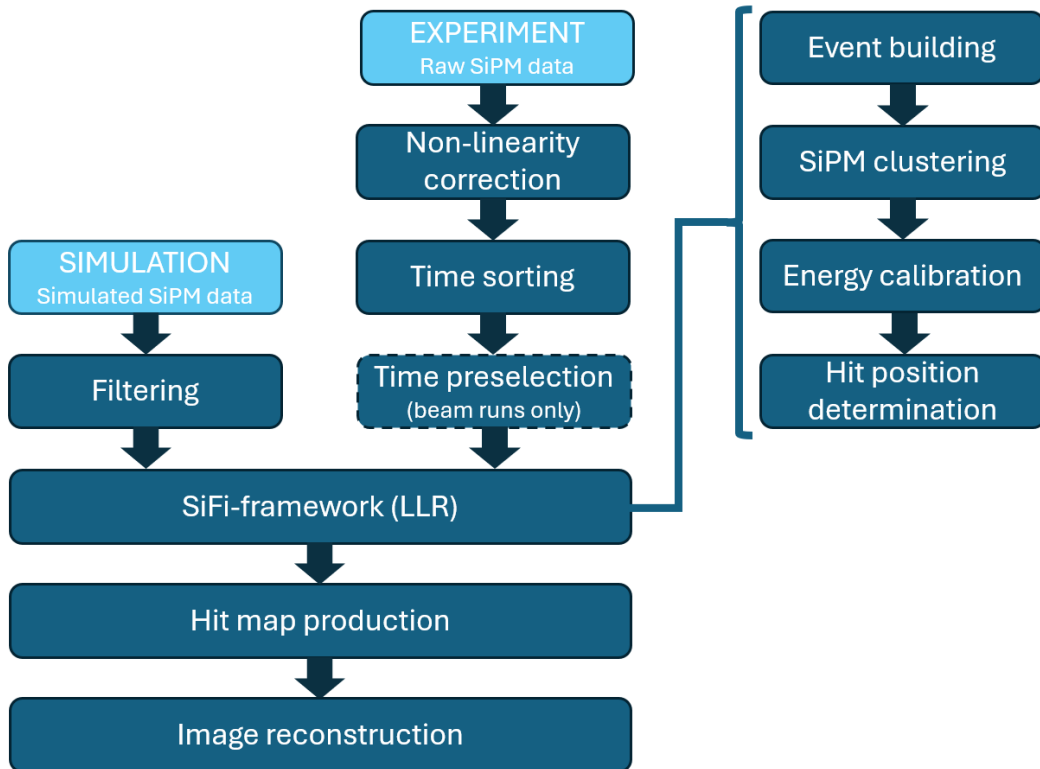


Figure 4.1: The general processing scheme of the data from the 1D CM measurements and simulations.

## 4.2 PREPROCESSING

### 4.2.1 Conversion of raw data to root trees

The DAQ software provided by the producer as part of the TOFPET2c DAQ system [129] was adapted to our needs<sup>1</sup>. The version of the code used to process

<sup>1</sup> The software was adapted by M. L. Wong.

the data described here is available in [130]. The software includes scripts and programmes that allow one to manage the data acquisition, save the data in a raw format, and process them to a desired format, e.g. a root tree. Conversion of the raw data is fast (in comparison with the processing time of the next analysis steps) due to the implementation of parallel processing. In our case, the raw data in the .rawf format are processed into .root files, and we refer to them as *TOFPET trees* in the following sections.

#### 4.2.2 Nonlinearity correction

As indicated in the TOFPET2c Software User Guide [131], the response of the ASIC charge-to-digital converter (QDC) preamplifier is nonlinear. Thus, the authors of the manual suggest either to perform one's own calibration with radioactive sources, or to linearise the dependence of energy  $E$  versus measured charge  $Q$  with the use of Equation (5):

$$E = P_0 \cdot P_1^{Q^{P_2}} + P_3 \cdot Q - P_0, \quad (5)$$

where  $(P_0, P_1, P_2, P_3) = (8, 1.04676, 1.02734, 0.31909)$  - see Equation (3.1), p. 25 in [131]. The authors claim that the formula allows for nonlinearity correction up to a level of 2-3% of the 511 keV peak energy resolution. We incorporated the correction into the modified DAQ software [130].

#### 4.2.3 Data splitting and sorting

For the data files above  $10^8$  entries there were memory issues in the LLR, so they were split into smaller batches of  $10^8$  entries. They were merged again in the analysis steps downstream of LLR. Another technical issue was that the entries in the TOFPET trees were in some cases not ordered by time. This occurred only in groups of entries that were very close in time. However, incorrect ordering, even when the entries' times do not differ much, can result in incorrect event building, and thus in loss of data. To avoid this problem, we sorted all TOFPET trees by time.

#### 4.2.4 Time preselection

A synchrotron beam is not continuous in time, but is delivered in spills, which can be observed on a time distribution of events in the detector (see the blue regions of higher counts in Figure 4.2) that reflects the time structure of the beam. The number of spills depends on the total number of protons and the beam intensity. The raw data from the measurements involving proton beam contain not only the information about interactions of PG quanta originating from the beam interaction with the phantom, but also the background before, after, and in between the spills (see the red hatched regions in Figure 4.2). In order to separate the spills from the background, time preselection was performed for all beam runs<sup>2</sup>: first,

<sup>2</sup> The time preselection and determination of background scaling factor were conducted by A. Wrońska and A. Fenger.

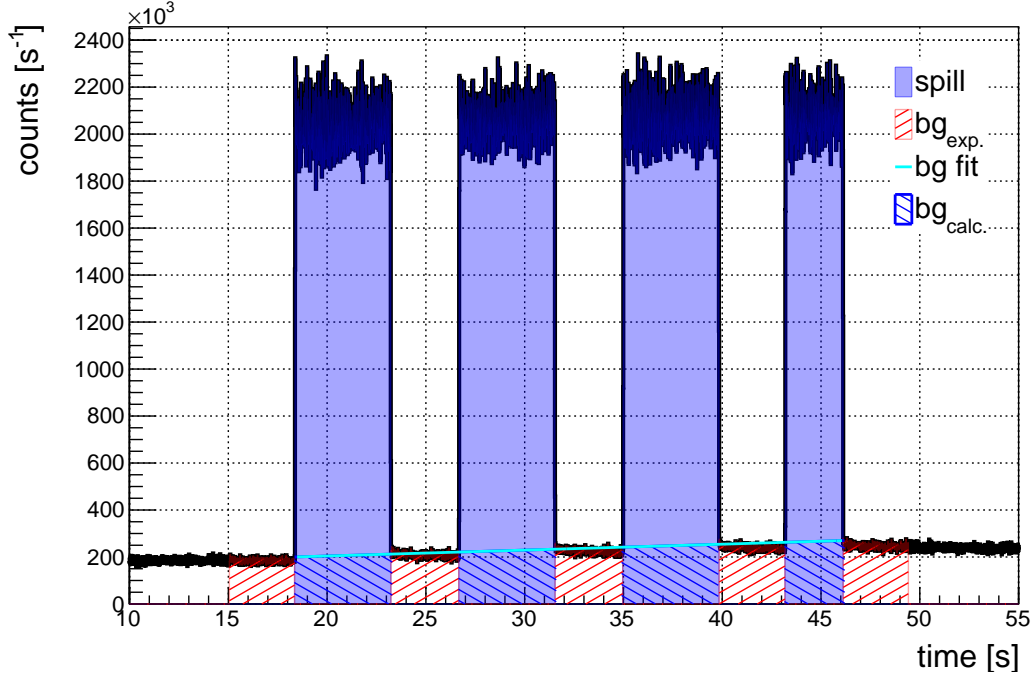


Figure 4.2: Example time distributions of events in the detector. The black line denotes the time structure of everything that was measured, spills are marked in blue, the region hatched in red is the experimental background, the one hatched in blue - the calculated background. The cyan line is the line of fit to the background parts.

the start and stop times of all spills in each beam run were determined. Then, the data between the start and stop times were labelled spills and saved as root trees. The inter-spill regions, as well as 3.3 s before the first and after the last spill, were labelled as background and also saved as root trees.

The energy spectra for an example run 569, divided into spills and background, can be seen in Figure 4.3. There, the background was normalised to match the spills with a scaling factor, determined the following way: firstly, the average counts of the background over 3.3 s before the first beam spill and the average counts over the same time after the last beam spill were calculated, making the  $y$  coordinates of 2 points in Figure 4.2. Then, the  $x$  coordinates of these points were assumed as the start time of the first spill and the stop time of the last spill, respectively. The line connecting these two points ("bg fit" line in Figure 4.2) was used to estimate the background (blue hatched lines in Figure 4.2). Let us denote number of counts in the experimental background as  $N_{\text{background exp.}}$  and number of counts in the calculated background (during spills) as  $N_{\text{background calc.}}$ . Then, the scaling factor  $c$  used to normalise the background to match the spill time is (Equation (6)):

$$c = \frac{N_{\text{background calc.}}}{N_{\text{background exp.}}} \quad (6)$$

The normalised background is later considered in the image reconstruction procedure (see Section 4.7.1), to obtain a clearer image.

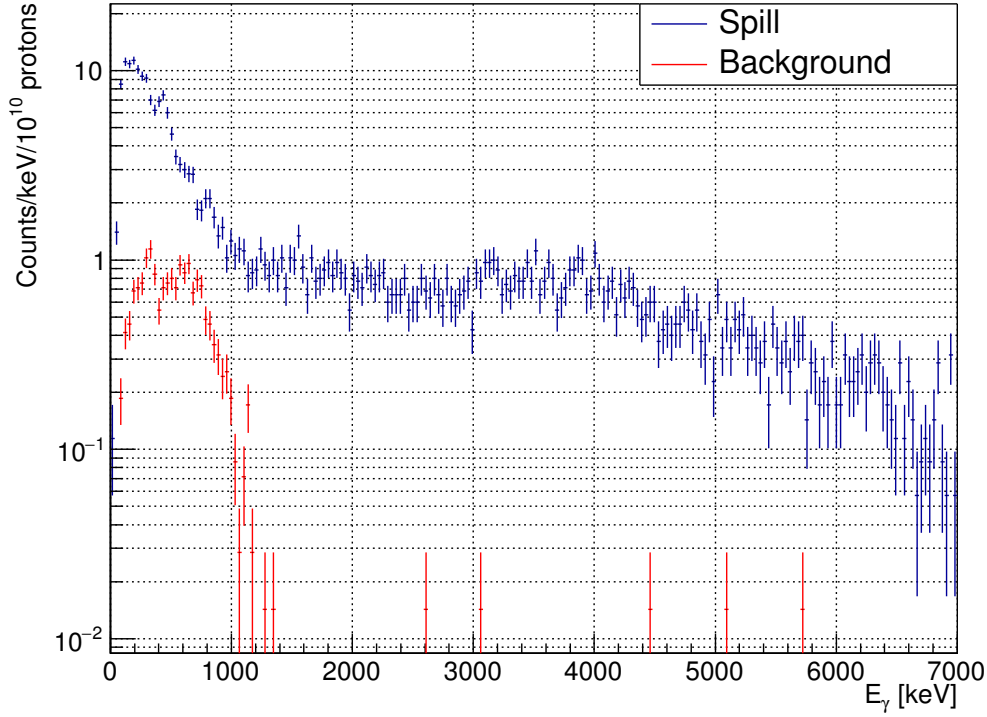


Figure 4.3: Energy spectrum for a selected fibre from run 569, divided into spill (blue) and background (red) parts based on the time information.

In Section 3.2.3.1, the spill counts ( $N_{\text{spill}}$ ) were determined using the scaling factor  $c$ , with Equation (7); there,  $K$  denotes number of spills,  $N_{i \text{ total}}$  - total counts in  $i$ -th spill, and  $N_{\text{background exp.}}$  - counts in the experimental background:

$$N_{\text{spill}} = \sum_i N_{i \text{ total}} - c N_{\text{background exp.}}, \quad i \in (1, \dots, K). \quad (7)$$

#### 4.2.5 Simulation filtering

A realistic simulation (see Section 4.6) was developed within the SiFi-CC group<sup>3</sup>, reproducing the experiment in the 1D CM mode. The simulation assumes that all the SiPMs work properly. However, in the experimental data, there were acceptance gaps caused by faulty SiPMs (see Section 3.1.2). To be able to directly compare the simulated and experimental results, we applied an additional pre-processing step to all the simulation data: entries associated with the SiPMs that were not responding during the experiment were excluded. The list of dead SiPMs can be found in Table A.1.

<sup>3</sup> The simulation was developed by R. Hetzel, M. Kercz and L. Mielke.



### 4.3 LOW-LEVEL RECONSTRUCTION

The *sifi-framework* is a custom data analysis software developed by the SiFi-CC group<sup>4</sup> [132], used for LLR. The software (in the version for the 1D CM modality) takes the TOFPET trees containing SiPM data as input and outputs trees containing fibre hit position information. The author of this thesis developed the following parts of this software that are relevant to the analysis of the 1D CM data: classes representing data objects (called categories) at different processing stages, data importer, SiPM clustering (in parts), fibre grouping, and the hit position determination [132].

#### 4.3.1 Structure and operation

The software is built out of three main types of classes: tasks, categories, and containers. The tasks process the data and write the result to categories, i.e. objects representing the data after a given processing stage. The containers store setup-specific data (SiPM-to-fibre mapping, calibration parameters, detector geometry details, etc.) and are used by the task classes. The detailed scheme of the *sifi-framework* (for the 1D CM modality) is presented in Figure 4.4, where the tasks are represented by rectangular blocks, the categories by the blocks with rounded corners, and the input and output data are marked with a different colour.

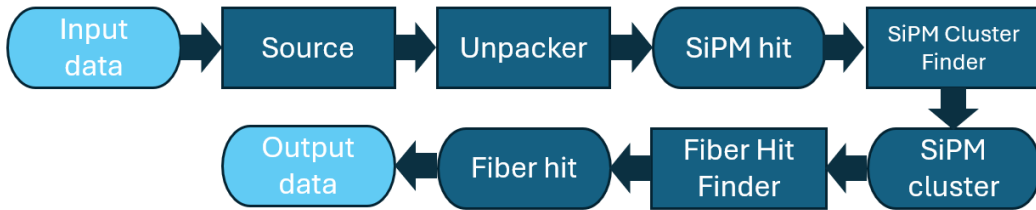


Figure 4.4: A scheme of the LLR software for the 1D CM modality.

#### 4.3.2 Reading in the data

The Source task reads in the data from a TOFPET tree in the form of entries, and the events are built: any entry belonging to a fixed trigger window of  $T_{TW} = 15$  ns, is assigned to the same event.

$T_{TW}$  was chosen based on an earlier study<sup>5</sup>, in which a wide trigger window was applied (50 ns) and the events were built. Then a histogram was filled with time differences between the first and the last entry within an event. The tail of the distribution of these differences ended at about 15 ns. Hence, we chose this value to be the trigger window in the analysis of all measurements in the 1D CM modality.

Each entry in the TOFPET tree contains:

<sup>4</sup> The core part of the software was developed by R. Lalik.

<sup>5</sup> The study was performed by K. Rusiecka.

1. ID of a DAQ channel,
2. time of signal detection, elapsed from the start of measurement, in picoseconds,
3. signal charge, expressed in arbitrary QDC units.

The time of each entry is rescaled from ps to ns. If there is a DAQ-related offset in the DAQ channel IDs (which is related to the PCIe board port ID used by TOFPET2c), it is subtracted so that the DAQ channel numbering starts at 0.

The data in this form are passed to Unpacker, where two containers are read in: for mapping and for energy calibration. First, the DAQ channel IDs are translated to SiPM IDs using the mapping container, then the charge is rescaled to energy units (see Section 3.1.1.2). Finally, the data in the modified form are saved to SiPM hit category. Any invalid hits (e.g. with a negative charge) are discarded at this stage.

#### 4.3.3 SiPM clustering

The SiPM hits need to be clustered to account for the situations in which the energy deposit extends over several neighbouring fibres and consequently, clusters of neighbouring SiPMs respond on both detector sides. The clustering is performed by the SiPM Cluster Finder. The task reads in the data from the SiPM hit category, performs clustering on its content, and writes the output to the SiPM cluster category. The clustering is performed on a set of SiPM hits as follows: an empty cluster is created, and the first SiPM hit is appended to it. We check this SiPM hit against all remaining SiPM hits and check if there are any neighbours of it (SiPMs are considered neighbours if they have a common edge or corner). If there are neighbours, we add them to the same cluster and continue checking all SiPMs in the cluster against all remaining SiPMs, if they are neighbours. If there are no more new neighbours after iterating through a whole cluster, a new cluster is created and the first unassigned SiPM hit is appended to it. Then the procedure of neighbour search is repeated as for the first cluster. The whole procedure is repeated until no unassigned SiPMs hits are left. Then, all the cluster characteristics are set:

1. cluster ID (starting from 0 and incrementing by 1 until all clusters are assigned an ID),
2. time: time of the earliest SiPM hit within the cluster,
3. module and side - rewritten from the first SiPM hit,
4. charge as the sum of all the charges from the SiPM hits constituting the cluster,
5. position, calculated as the centre of gravity (the address weighted by charges associated with participating SiPM hits).

The category SiPM Cluster is filled with those characteristics.

#### 4.3.4 Finding fibre hits

The next task takes SiPM clusters from the SiPM Cluster category, identifies fibres connected to them, builds fibre groups, assigns event types, and finds the fibre hit positions. Then, the fibre groups are written to Fibre hit category, which is the output of the LLR saved to a root tree. The Fibre hit category contains the following variables: module, layer, fibre, energy information on both fibre sides, time on both fibre sides, event type. The procedure for finding the fibre hits is as follows (performed for each event):

1. For each top-bottom cluster pair, common fibres are found. It is done using a parameter container that associates each SiPM ID to fibre IDs.
2. We check if the common fibres for each cluster pair are grouped together spatially. A fibre belongs to a group if it has at least one common side or one common corner with any other fibre from the group. Any events with more than one fibre group are excluded from further analysis.
3. Based on the number of SiPM clusters on both detector sides ( $c_{top}$ ,  $c_{bottom}$ ) and fibre multiplicity ( $m_f$ ) per cluster pair (i.e., how many fibres are assigned to a given cluster pair), the events are classified as belonging to one of five classes (see Figure 4.5):
  - a)  $c_{top} = 1$ ,  $c_{bottom} = 1$ ,  $m_f = 1$ : unique clusters, unique fibre.
  - b)  $c_{top} = 1$ ,  $c_{bottom} = 1$ ,  $m_f > 1$ : unique clusters, multiple fibres.
  - c)  $c_{top} = 2$ ,  $c_{bottom} = 1$ ,  $m_f > 1$ : top semi-unique cluster
  - d)  $c_{top} = 1$ ,  $c_{bottom} = 2$ ,  $m_f > 1$ : bottom semi-unique cluster
  - e)  $c_{top} > 1$ ,  $c_{bottom} > 1$ ,  $m_f > 1$ : ambiguous clusters
4. Based on the assigned class, the hit positions in  $x$  and  $z$  dimensions and energy deposits are found and assigned:
  - Type a: the hit position is simply the position of the only fibre, and the energy deposits on the top and bottom fibre ends are the deposits from the top and bottom clusters.
  - Type b: The hit position along the layer ( $x$ ) is defined as a weighted mean of active fibre IDs. The weight is defined as a geometric average of energy deposits in the SiPMs ( $E_{top}$ ,  $E_{bottom}$ ) at both fibre ends:  $\sqrt{E_{top}E_{bottom}}$ . The hit position across the layers ( $z$ ) is assigned as the frontmost detector layer containing an active fibre. Then, the hit position ( $x$ ,  $z$ ) is rounded to the ID of the closest fibre. The energy deposits are determined as the energy deposits in top and bottom cluster, respectively. Note that the whole energy deposit in a given event is assigned to a single "main" fibre.
  - Types c and d: the merged cluster energy deposit has first to be divided in two, according to the ratio of energy deposits in clusters on the other side. After the clusters separation, the procedure is the same as for b-type events.

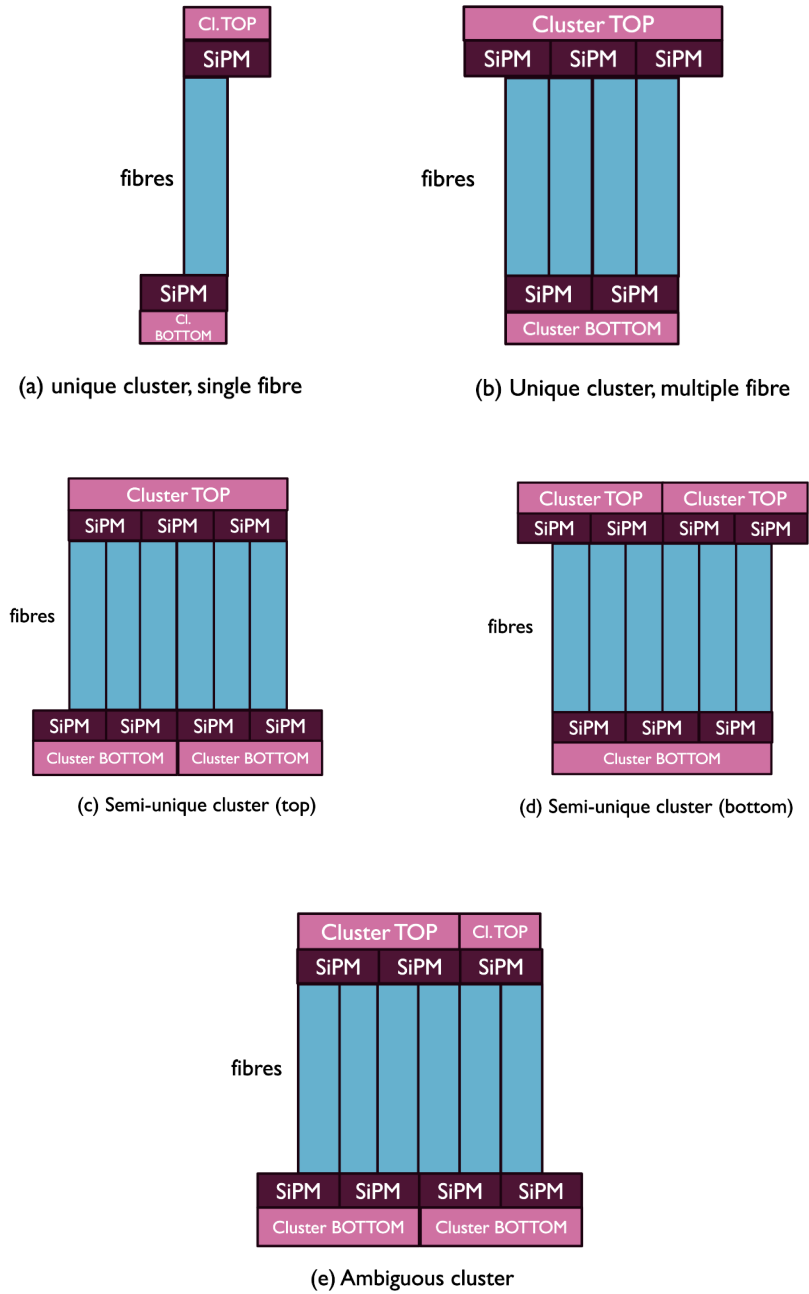


Figure 4.5: Classes of events in the LLR. This is a symbolic representation, as the actual clusters are formed in two dimensions.

- Type e: these events are excluded from further analysis, as there is currently no method implemented to determine the hit positions and energy deposits for them.

The time of the fibre hit is defined for all event classes as the time of the earliest SiPM hit in a given event.

5. The Fiber hit category is filled and saved in the tree. The data saved in this category form the output of LLR.

#### 4.4 HIT MAPS PRODUCTION

A convenient representation of the data after LLR is a hit map, i.e. a spatial hit distribution over the detector module. It is represented by a 2D histogram, integrated over the  $y$  coordinate. On the  $x$  axis, there is the fibre number within one layer (0-54), and on the  $y$  axis, there is the layer number (0-6). The colour scale denotes either the number of hits in each fibre, or the total energy deposit, depending on the map type. Example hit maps are presented in Figure 4.15, acceptance gaps due to several faulty SiPMs are visible. In the 1D CM modality, one fibre is one detector pixel (forming one bin of the hit map), and the hit position along the fibre is not needed. Thus, the hit map contains complete information about the detector response and can be input to the image reconstruction (see Section 4.7.1). To create the hit maps, we iterate over the output trees from the LLR event by event, and fill the hit maps if appropriate criteria are met. In this analysis step, 16 hit maps were produced for each run, varying the following conditions:

- 4 lower thresholds on energy deposits: 0, 500, 1000, 1500 keV (or the corresponding thresholds in the photon counts units in the simulation case; see Table 4.2 in Appendix),
- 2 sets of event classes considered: unique clusters only (Figure 4.5a,b) or both unique and semi-unique ones (Figure 4.5a-d),
- 2 filling options: if there was a hit in a given detector pixel, the corresponding bin is incremented by 1 (map of hits) or by the energy value (energy deposition map).

The best variant was then selected in the image reconstruction optimisation step. The upper threshold for hits included when filling all types of hit maps was fixed to 7000 keV; the reason for choosing this value is explained in Section 4.5.3.

#### 4.5 AUXILIARY STUDIES

In this section, various auxiliary studies are presented that provided insight into the 1D CM data. They are presented in this section along with their results to keep the logical order, since the conclusions from some of them influenced the main analysis chain.

#### 4.5.1 Fibre calibration parameter spread per SiPM

A fitting procedure similar to the one in Section 3.1.1.2 was also performed on charge spectra per fibre, after selecting only events with a single-fibre response (event type a, see Figure 4.5a). This method provides the calibration parameters with slightly lower uncertainty, compared to the SiPM gain alignment factors. However, the obtained fibre calibration parameters were not used in the main data analysis chain because they are suitable only for the single-fibre events (where a fibre which was hit can be uniquely identified), while it is favourable to apply the same method of gain alignment across all the event classes.

The calibration parameters obtained per fibre served for another auxiliary study of the spread of gains in the detector. Generally, there are two main sources of calibration parameters spread: structural imperfections in fibres and uneven gain of the SiPMs. To check which effect is stronger, we calculated the average calibration parameter spread for fibres coupled to the same SiPM and compared it with the calibration parameter spread for all fibres. The plots for several selected SiPMs are presented in Figure 4.6. The results are summarised in Table 4.1, separately for

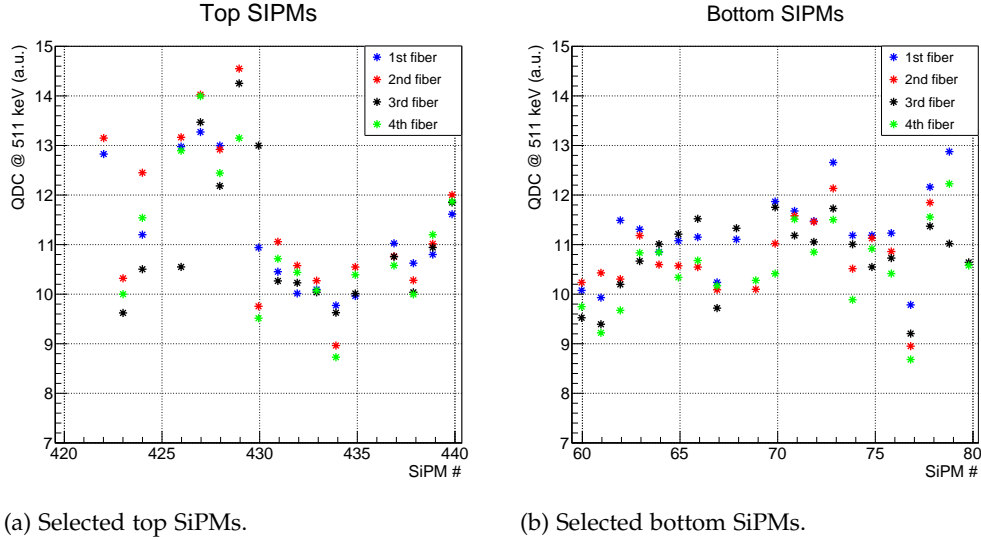


Figure 4.6: The spread of calibration parameters per fibre for selected SiPMs.

top and bottom SiPM boards. There, one can see that the fibre calibration parameter spread within one SiPM is about 50% of the total fibre calibration parameter spread, which implies that the remaining part of the effect can be attributed to differences between SiPMs. Therefore, the calibration parameter spread caused by fibre variability and the gain spread caused by SiPM variability are of the same order. The absolute spread is 28% for the top detector side and 24% for the bottom side; we did not study the origin of the spread difference between the sides. Overall, we find the magnitude of the spread effect to be acceptable for our purposes. In the data analysis, the effect is diminished by aligning the SiPM gains (see Section 3.1.1.2).

Table 4.1: Calibration parameter spread for fibres.

	Side	$\sigma$ of correction factor	Relative spread
fibres coupled to single SiPM	TOP	0.67	12%
all fibres	TOP	1.59	28%
fibres coupled to single SiPM	BOTTOM	0.76	13%
all fibres	BOTTOM	1.37	24%

#### 4.5.2 Photon counts calibration

In the simulation data, the charge collected by the SiPMs is expressed in photon counts. To be able to apply energy thresholds on simulation hit maps, we need to know the corresponding photon count values. For this purpose, we plot a 2D histogram of  $Q_{av}$ , which is a geometric mean of charges collected by the bottom and top SiPM, vs. energy deposited in the fibre, which is the MC truth data. In such a histogram (see Figure 4.7), a bright line is visible that marks the dependence between the SiPM charge and the true energy deposited in the fibre. The  $Q_{av}$  values for the needed energy thresholds were read out from the histogram, they are listed in Table 4.2. These thresholds were applied to the simulation hit maps, so that they matched the energy thresholds on the experimental hit maps.

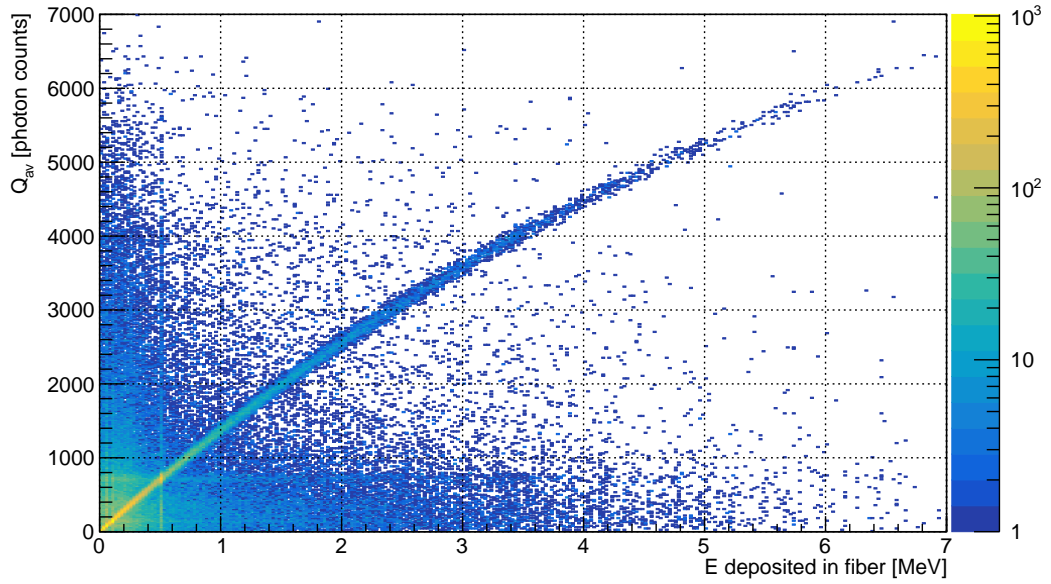


Figure 4.7: Geometric mean of charges collected by the top and bottom SiPM ( $Q_{av}$ ), versus energy deposited in the fibre (MC truth data).

Table 4.2: Energy thresholds applied to the hit maps from the experiment, and the corresponding values in photon count units, applied to the hit maps from simulation.

Energy [keV]	SiPM photon counts
0	0(20)
500	710(20)
1000	1362(20)
1500	2013(20)

#### 4.5.3 Inspection of fibre energy spectra

Looking at the hit maps created for the beam measurements without any energy cuts, we noticed unexpectedly high counts in some of the first fibre columns (region 1; see Figure 4.8) and in the first layer (region 2). To explain these effects, we investigated the energy spectra of individual fibres. Example fibre spectra from these regions can be found in Figure 4.9: (a) one of the first columns (region 1), (b) first layer (region 2), and (c) middle part of the detector (outside regions 1 and 2, for reference). In regions 1 and 2 we observed high-energy contributions in the spectra, up to a few tens of MeV, which was not the case for the middle part of the detector. Since these energies were too high to be deposited by PGs, there must have been another source of these contributions. The initial assumptions were that the effect in the first few columns was caused by beam protons scattered in the exit nozzle, whereas the effect in the first detector layer was caused by protons scattered in the phantom.

To verify the assumption for region 1, we checked how deep the particles penetrate the detector for the minimum and maximum beam energies used (S1 - 70 MeV; S7 - 108 MeV). For S1, the additional contribution in the spectrum was present up to the fourth column, which is 8 mm of range. For S7, it was seen up to the ninth layer, corresponding to 18 mm of range. Using SRIM [133], we calculated the proton energies that would correspond to such ranges in the scintillation material. We obtained the following values:  $\sim 65$  MeV for S1 and  $\sim 100$  MeV for S7, which are close to the beam energies used in these measurements. This is consistent with the assumption, that the effect of increased counts in the first few columns is caused by primary protons. As these additional counts are predominantly deposited in the high-energy region, which is not of our interest as we focus on PG detection, we can reduce this contribution by applying an upper threshold on energy deposits. Thus, an upper threshold of 7 MeV was applied to all measurements with the beam before putting them into the image reconstruction.

We repeated a similar study to explain the effect of increased counts in the first detector layer (region 2), but the expected range of secondary protons (up to 2 mm at the energy of up to 30 MeV, as only the first layer was affected) does not match the expected secondary proton energies: from the kinematics of the two-body scattering, any secondary protons reaching the detector would have a lower energy ( $\sim 1$  MeV), which corresponds to  $9.19 \mu\text{m}$  of range. This energy is much



lower than what we observe in the energy spectra, which span up to about 40 MeV. For now, the origin of the high-energy contribution in the first detector layer is unclear, but since it is also mostly present at higher energies, it can be eliminated by application of the same upper threshold on fibre hit energy deposits.

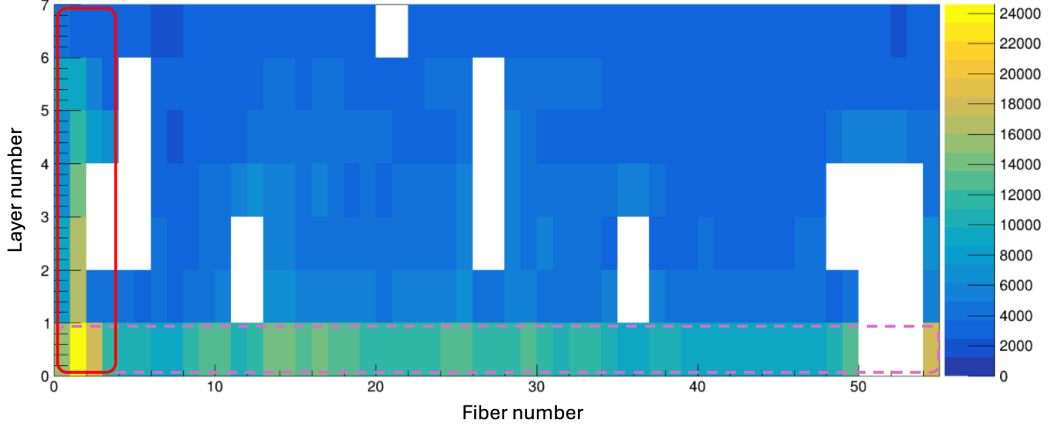


Figure 4.8: Hit map with no upper or lower energy threshold for an example run 569 (beam spot S1). Regions with unexpectedly high counts are marked: red contour, several first columns (region 1); dashed pink contour, first layer (region 2).

#### 4.5.4 Hit maps in different beam spots

The purpose of this study was to preliminarily assess the quality of the hit maps before inputting them to the image reconstruction. We investigated how the detector response changes with the beam penetration depth (beam spots S1-S7). The hit maps for these beam spots are presented in Figure 4.10a-g. There, one can see the number of entries increasing with penetration depth and that the further columns of the detector register more hits, which are the expected effects. On top of this, the irregular pattern is visible, which we attribute to the mask shape. Several other effects can be observed:

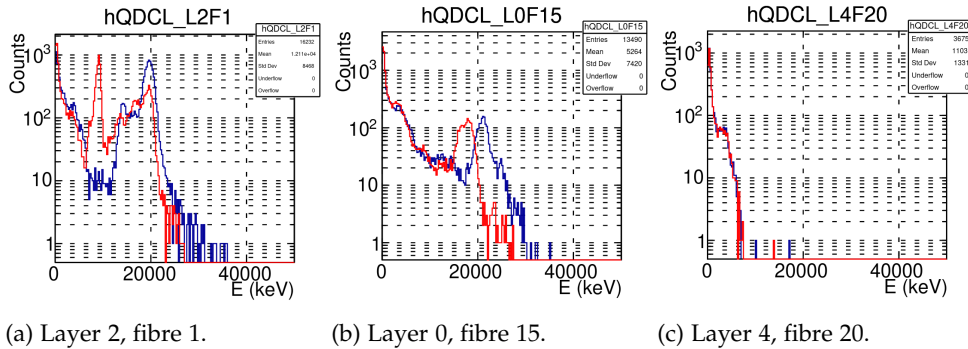


Figure 4.9: QDC spectra for selected fibres: region 1 (a), region 2 (b) and reference from the middle of the detector (c). The red spectrum is from the SiPM on the top side, the blue one from the SiPM on the bottom side.

1. increased counts in the bottom right pixel and increased counts in several pixels of the first few columns (especially pronounced for S1) - the reasons for this effect were studied in Section [4.5.3](#).
2. brighter spots behind the acceptance gaps (in the deeper layers) and darker spots in front of them (in the shallower layers).

These effects are unfavourable, because they do not originate from the PGs that are of interest, but are either background effects or artefacts of the analysis due to the acceptance gaps. The first effect is already mitigated by applying an upper threshold on the hit maps but is not completely eliminated. This is another reason for excluding the regions with increased counts from further analysis (see Section [4.7.5](#)). The other effect is a distortion of the hit map due to the applied algorithm that assigns SiPM hits to fibres and the presence of acceptance gaps; we did not study it further, but instead attempted to account for it (see Section [4.2.5](#)).

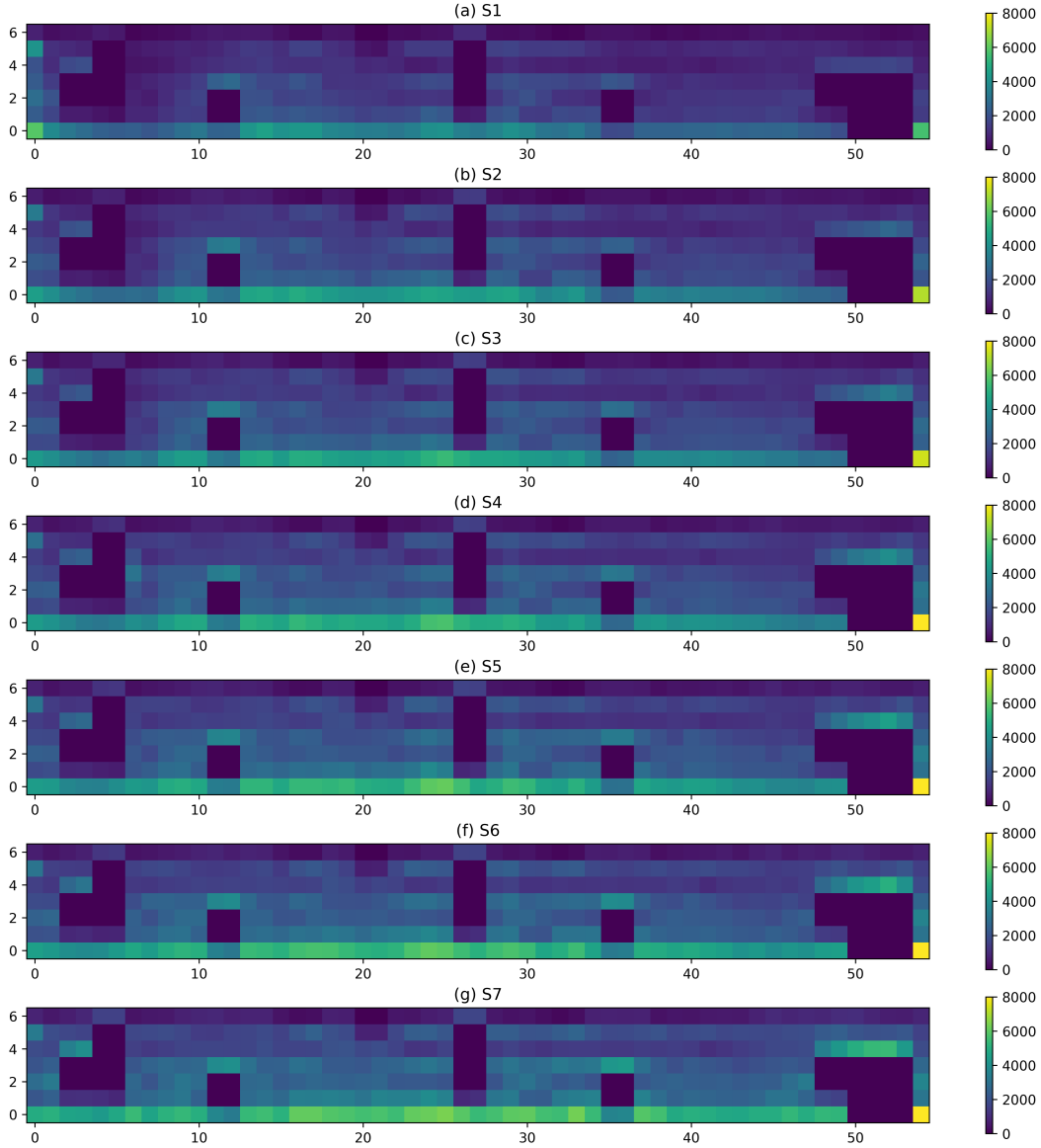


Figure 4.10: Hit maps (detector response) for beam spots S1-S7. Cuts on energy deposits: 1-7 MeV, colour scale of fixed range denotes the number of hits per detector pixel. Horizontal axis - number of fibre within a layer, vertical axis - layer number.

#### 4.5.5 System stability over time

For beam spots S2-S4, measurements were repeated roughly 30 minutes after the main measurement series with statistics increased 10 times (i.e., to  $10^{11}$  protons). We refer to them as S2'-S4'. The pairs of measurements ( $S_n, S_{n'}$ ) were used to assess the stability of the detection system over time. The hit maps for measurements S2'-S4' were first normalised to match the statistics of measurements S2-S4. Then, we created maps of the differences in entries per pixel ( $N_{S_n} - N_{S_{n'}}$ ) and checked if they are uniformly distributed or show irregular patterns. Then, we looked at 1D histograms of the said differences. We expect the differences to form a Gaussian shape around 0. A non-Gaussian shape or a large shift with respect to 0 could

be a sign of some unfavourable effects in the experimental setup, e.g. a noise contribution growing with time due to SiPM heating.

The maps of the differences ( $N_{\text{Sn}} - N_{\text{Sn}'}$ ) are presented in Figure 4.11. There,

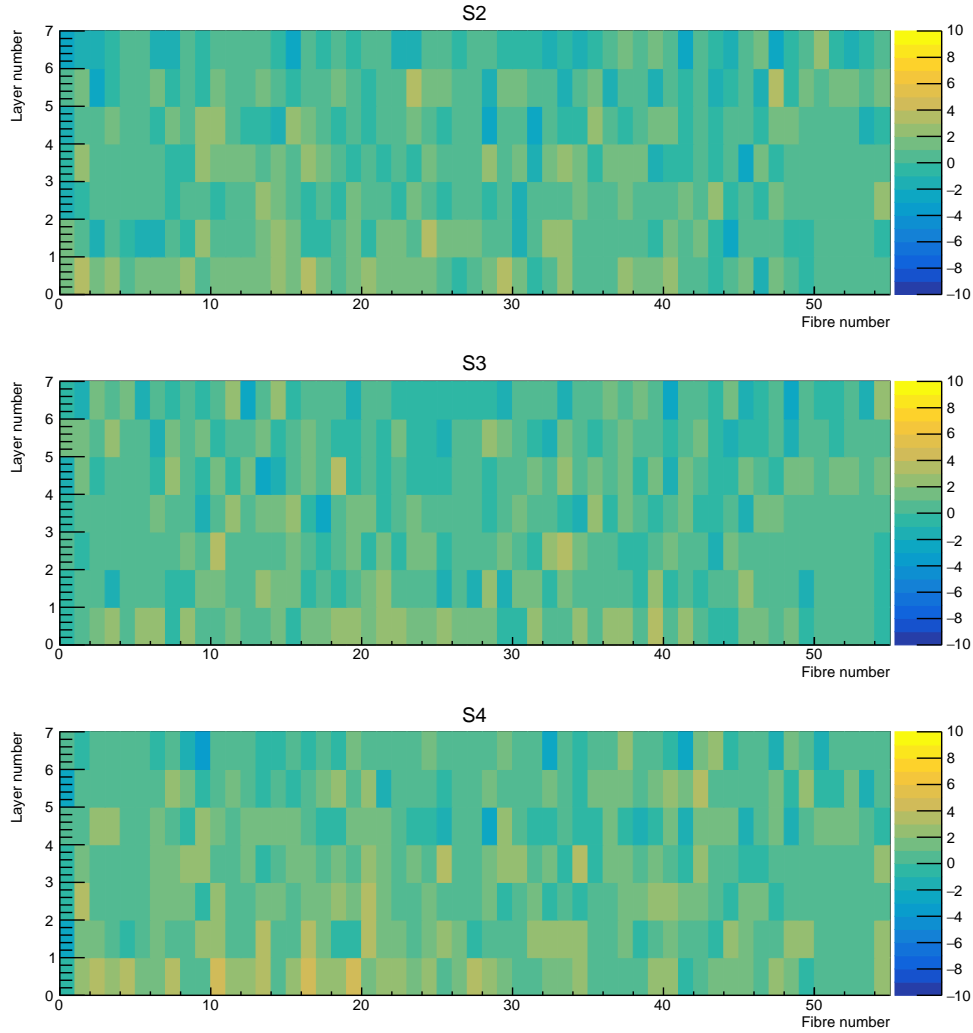


Figure 4.11: Maps of differences between numbers of events per pixel in two different measurements for the same beam spot, in units of standard deviation, normalised.

one can see that the differences are uniformly scattered for all beam spots, as expected. The histograms of the differences in entries per pixel ( $N_{\text{Sn}} - N_{\text{Sn}'}$ ) are presented in Figure 4.12, in units of standard deviation. The dead fibres were excluded. There, one can see that for all three investigated beam spots, the distribution of differences is Gaussian-like, as expected. It is not centred around 0, but instead shifted towards the positive values. Nevertheless, for all the examined beam spots, the shift ( $\mu$  in the histogram legend) is up to about 1 standard deviation, which we consider a small shift without significant influence on the main analysis. There is no clear trend in the shift values, but the largest shift occurs for the deepest beam spot examined (S4).

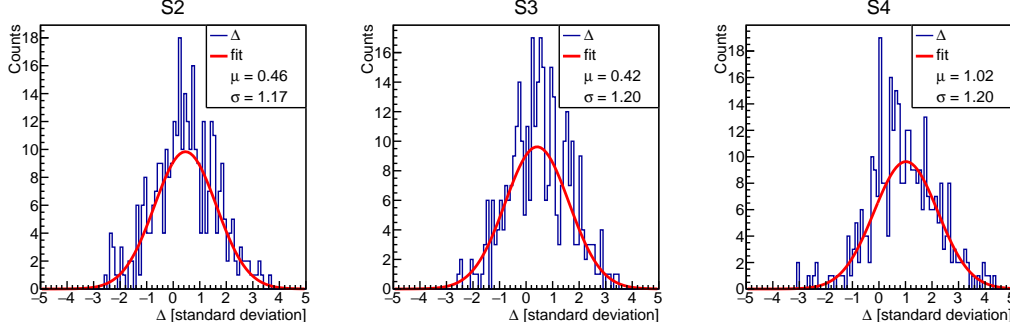


Figure 4.12: Distributions of differences ( $\Delta$ ) between numbers of hits per pixel in two different measurements for the same beam spot, in units of standard deviation. The red line denotes a Gaussian fit to the distribution.

#### 4.5.6 Background studies

The shape of the energy spectrum hints at the background origins. In Figure 4.13a, a comparison is presented of the background energy spectra before and after the beam spill. Both measurements lasted 3.3 s. There, one can see that the spectrum after the spill has higher intensity in the region up to 700 keV. Several peaks are visible in both spectra, corresponding to the peaks in the LYSO:Ce,Ca activity spectrum (see, for example, the simulation results in [128]). In the second spectrum, an additional peak of energy close to 511 keV can be observed, along with an increased contribution to the spectrum at energies below the peak energy. The difference of the two spectra (the spectrum before the spill was subtracted from the spectrum after the spill) is presented in Figure 4.13b. There, one can clearly see the annihilation peak at 511 keV, and the associated Compton continuum at lower energies. This confirms that production of  $\beta^+$  emitters is the main beam-generated background source to PG detection.

#### 4.5.7 Contributions of event classes in LLR

We examined the contributions of event types a-e (see Section 4.3.4) in the experimental data. The distribution of the event types is similar for both the spill and background part of run S4: the single-fibre events (type a) are about 41% of all events, the multi-fibre events with unique clusters (type b) are almost 50%, 10% are the semi-unique cluster events (types c and d), and the ambiguous events are up to 0.2% of the data sample. For run 596 with a radioactive source, there is a larger fraction of single-fibre events in the data sample: 62%, while the multi-fibre events form 32% of all events. Semi-unique events are 7% in total, while ambiguous events are only 0.05%. The exact values of the event type distributions are summarised in Table 4.3.

Based on the distribution of event types, we decided that the semi-unique cluster events (types c and d) form a significant part of the data sample, so we need to include them in the analysis. As the ambiguous events constitute only a small fraction of the data sample and including them would involve developing a dedicated procedure to separate the clusters, we decided to disregard them in the analysis.

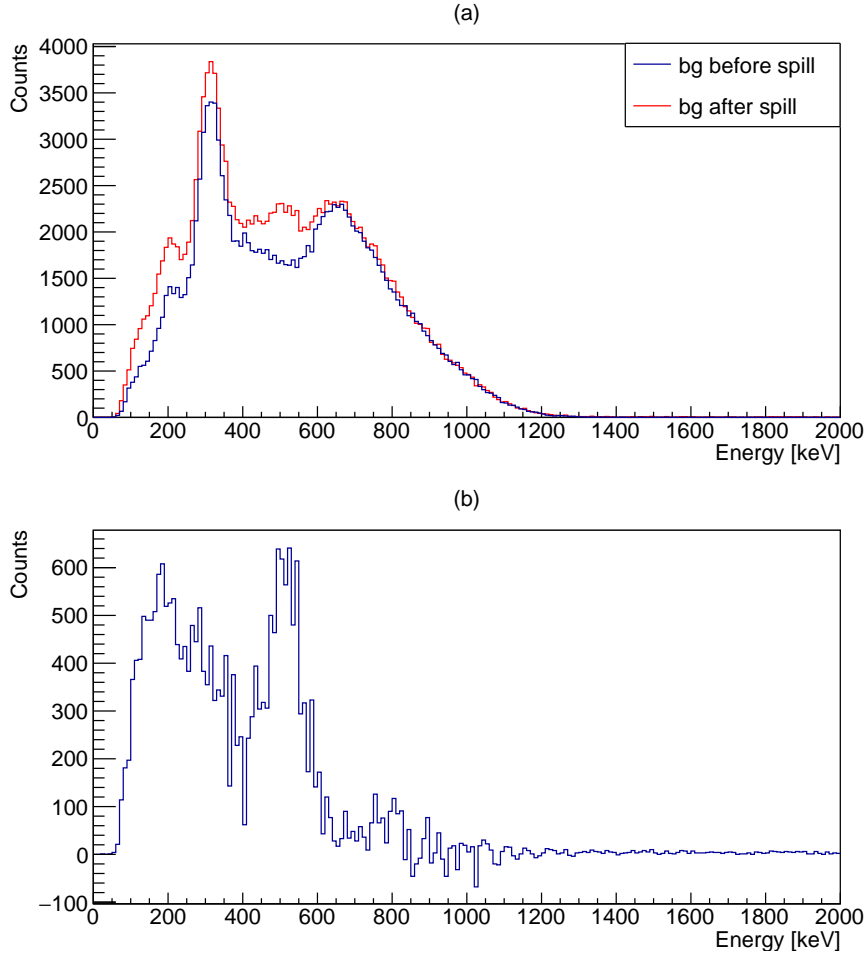


Figure 4.13: (a) Energy spectra of the background before (blue) and after (red) the beam spill for beam spot S4; (b) Difference of spectra from the plot in (a) - beam-induced background.

Table 4.3: Multiplicity of event types (a-e) in various run types.

	Type a [%]	Type b [%]	Type c [%]	Type d [%]	Type e [%]
S4 (spills)	40.86	49.28	5.58	4.07	0.21
S4 (background)	40.61	47.89	5.90	5.67	0.10
Source run (596)	61.87	31.28	3.32	3.49	0.05

#### 4.6 ANALYSIS OF MONTE CARLO DATA

In order to reproduce the experimental conditions of the beam tests of the detector in 1D CM modality, a realistic Geant4 [134] simulation was set up<sup>6</sup>. The simulation was based on the previous developments by J. Kasper, described in [89]. The version of the Geant4 code was 10.4.2, the physics list used was QGSP\_BIC\_HP\_EMZ (see [135]), an additional package was used to manage the

<sup>6</sup> The simulation was developed by R. Hetzel, M. Kercz and Linn. Mielke.

properties of scintillation crystals and SiPMs [136]. The simulation consisted of the following steps:

1. Interaction of the beam with the phantom: a simulated proton beam of fixed energy hits the phantom. The secondaries from beam-phantom interactions propagate in the phantom up to its borders. There, their data (i.e., direction, energy, and time) are saved as phase-space files.
2. Interactions of the secondary particles from the phantom with the detector: the secondary particles (saved as phase-space files in the previous step) are emitted outside the phantom and interact with the detector. The simulation stops when the SiPMs register the optical photons generated in the scintillation fibres. The output files from the simulation contain the data registered by the SiPMs, the information about the particles that triggered the detector, and the Monte Carlo truth information about the fibre hits.

The simulation data are adjusted to the experimental data by introducing the acceptance gaps that were present in the experiment (see Section 4.2.5), and then processed with the same analysis chain as the experimental data. In this way, we can directly compare the simulation and the experimental results. Additionally, the full simulation without the acceptance gaps is also processed and compared with the adjusted one, to estimate the influence of the acceptance gaps on the detector performance in terms of the image reconstruction quality.

## 4.7 IMAGE RECONSTRUCTION

### 4.7.1 MLEM algorithm

In order to reconstruct the PG image (which is in our case a 1D PG depth profile) from the detector response in the form of hit maps (described in Section 4.4), we use the MLEM [80, 81] algorithm, implemented in a custom software<sup>7</sup>. The MLEM algorithm is provided in Equation (8):

$$\mathbf{f}^{(k+1)} = \frac{\mathbf{f}^{(k)}}{S} \mathbf{A}^T \frac{\mathbf{y}}{\mathbf{A}\mathbf{f}^{(k)} + \mathbf{b}}, \quad (8)$$

where the system matrix is denoted with  $\mathbf{A}$ ;  $S$  is the sensitivity;  $\mathbf{y}$  denotes the measured detector response;  $\mathbf{b}$  stands for background; vectors  $\mathbf{f}^{(k)}$  and  $\mathbf{f}^{(k+1)}$  are the reconstructed PG depth profiles (projections) after iterations  $k$  and  $k + 1$ , respectively. The vector element  $f_j^{(k)}$  is the reconstructed number of PGs emitted from the FOV pixel  $j$ , the length of this vector  $J = 100$  equals to the number of FOV pixels. Elements of  $\mathbf{f}^{(0)}$  are initialised with ones.

The components of the formula are explained in the following section.

<sup>7</sup> The software for image reconstruction in the 1D CM modality was written by V. Urbanevych, and it was later modified and extended by the author of this thesis.

## 4.7.2 Input to the image reconstruction

### 4.7.2.1 System matrix

The system matrix (SM) is a fundamental concept in statistical iterative image reconstruction algorithms. It relates the image space to the projection space. An SM element  $a_{ij}$  expresses the probability that a particle emitted from the source pixel  $j$  is registered in the detector pixel  $i$  [137].

The SM for our purpose was generated<sup>8</sup> using the simulations described in Section 4.6. The first stage of the simulation was modified though: instead of a phantom interacting with the proton beam and generating secondary particles including PGs, a point-like gamma source was used as an event generator. The FOV of the detector (at  $y = 0$  and  $z = 0$ ) was divided into 100 bins (pixels) of equal length. Then, a gamma source was placed in the centre of the first pixel and the detector response was recorded. The procedure was repeated for source positions in all the FOV pixels. For each source position, the full detector response was saved, the hits from dead pixels were filtered out, the data were processed with the usual analysis chain and the hit maps were created. Then, the hit maps of dimensions 7 layers  $\times$  55 fibres were flattened<sup>9</sup> into vectors of length 385. Each of such vectors formed one column of the SM, which can be seen in Figure 4.14. There, SM is not normalised, each bin contains the number of hits for a given detector pixel. To be interpreted as probability, SM needs to be normalised to the total number of emitted gammas into the full solid angle (which was  $37.798 \times 10^6$ ). This is an ideal SM for uniform efficiency,  $\tilde{a}_{ij}$ . Before putting the SM in the MLEM formula, it was corrected for efficiency:  $a_{ij} = \epsilon_i \tilde{a}_{ij}$  (see the efficiency calculation in Section 4.7.3); moreover, the matrix elements corresponding to the response in dead fibres were excluded, so the resulting SM has dimensions of  $100 \times 303$ .

### 4.7.2.2 Sensitivity

The sensitivity is defined as the probability that a PG emitted from a given FOV pixel is registered by the detector. We calculate the sensitivity by summing up the system matrix elements column-wise over the detector pixels. The resulting vector has 100 elements, which is the number of FOV pixels.

### 4.7.2.3 Spills and background separation

After the time preselection (see Section 4.2.4), there are two types of files from the runs with the proton beam: spills and background. The flattened hit maps produced based on spill data are inputted into the MLEM formula (Equation (8)) as the measured detector response  $\mathbf{y}$ , while the flattened hit maps obtained for background, normalised according to the procedure described in Section 4.2.4, are put into the formula as background  $\mathbf{b}$ . Both  $\mathbf{y}$  and  $\mathbf{b}$  vectors have 303 elements, i.e., the number of all detector pixels (385) minus the dead pixels. The hit maps for the two parts of an example run 568 (beam spot S4) are presented in Figure 4.15a for spills and in Figure 4.15b for background.

<sup>8</sup> The SM was generated by M. Kercz.

<sup>9</sup> Here and in the further parts of this thesis, flattening a hit map means creating a vector by appending the hit map rows to it, one after another.



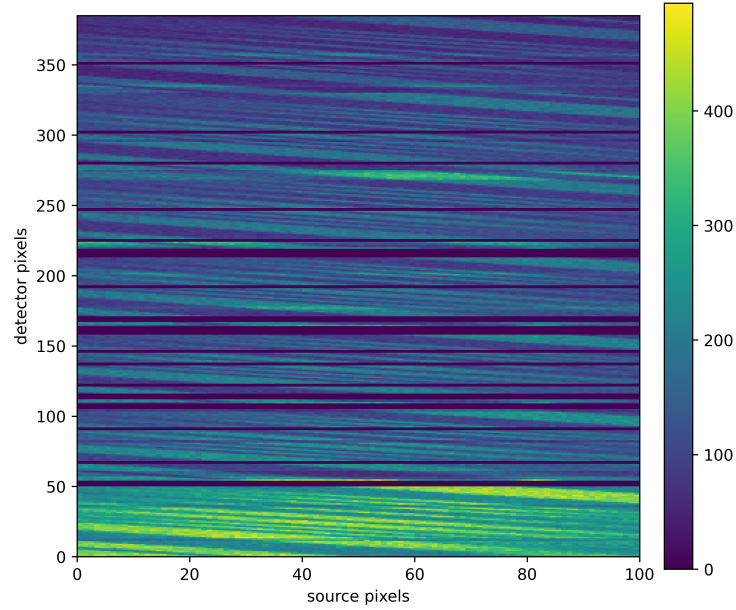


Figure 4.14: The system matrix (before normalisation and removal of elements corresponding to dead fibres), used in the reconstruction of images from the 1D CM modality detector tests.

#### 4.7.3 Efficiency correction

Detection efficiency can vary for each detector pixel due to various hardware imperfections, e.g., non-uniformities in the fibre structure, different thicknesses of the coupling layer, or some dead cells in the SiPMs. To correct for these effects, it was necessary to perform an auxiliary measurement with uniform detector irradiation (reference), a simulation reproducing conditions of such a measurement (simulated reference), and a measurement of background. Both measurements were described in Section 3.2.4. The hit map for the reference measurement is presented in Figure 4.15c, the background hit map can be found in Figure 4.15d.

A simulation reproducing the reference measurement was performed<sup>10</sup>. The simulated detection setup was identical to the experimental one, the number of simulated particles was  $4 \times 10^8$  and the particle emission angle was limited to  $35^\circ$ , so that particles from all regions of the source contribute to the data. The simulated reference hit map is presented in Figure 4.15e.

All three data sets (reference, simulated reference and background) were processed in the same way with the LLR reconstruction software and hit maps were created, with selected hit energies within  $2\sigma$  around the 511 keV peak - the main peak in the registered energy spectra from the used radioactive source. The hit maps were flattened into vectors. As a result, we obtained three vectors of 303 elements each:  $R$  - reference measurement,  $SR$  - simulated reference measurement, and  $B$  - background. For the detector element  $i$ , the efficiency  $\epsilon_i$  was calculated according to Equation (9):

$$\epsilon_i = \frac{R_i - B_i}{SR_i}. \quad (9)$$

<sup>10</sup> The simulation was prepared by R. Hetzel.

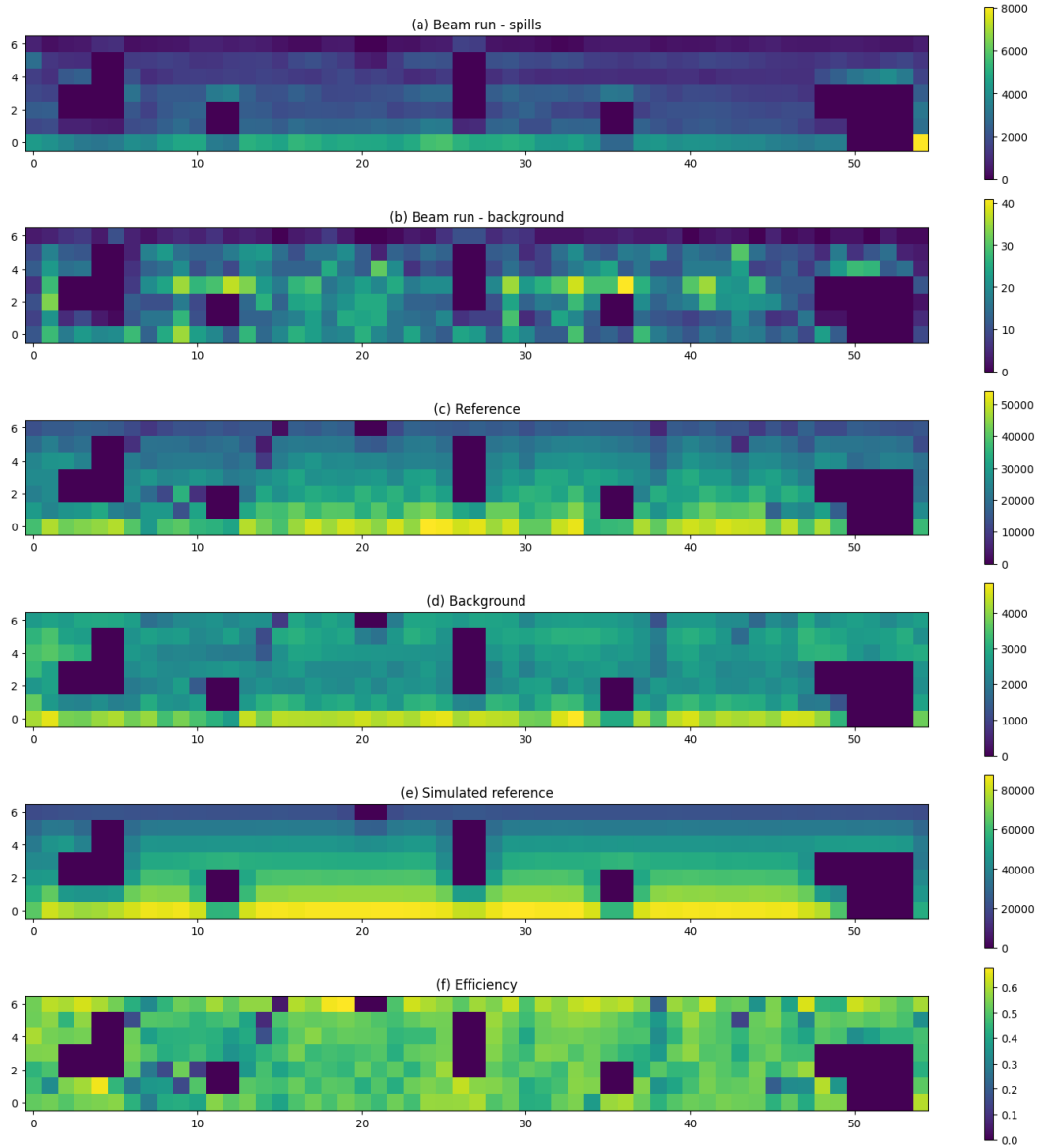


Figure 4.15: Example hit maps; detailed description in the text. Horizontal axis - number of fibre within a layer, vertical axis - layer number.

The efficiency map obtained, normalised to unity in its maximum, can be found in Figure 4.15f. In the calculations, it was flattened to one dimension, but it is presented as a 2D hit map for visualisation purposes, with the dead pixels manually set to 0. The efficiency is included in the system matrix.

#### 4.7.4 Distal falloff position determination

The MLEM formula was applied to the data for the chosen number of iterations, and the PG depth profiles were obtained for each of the beam spots (S1-S7). A PG depth profile represents the distribution of the PG emission vertices from the phantom, we use the standard normalisation to unity in the profile maximum. The distal falloff of a PG depth profile is strongly correlated with the proton beam

range [37], so it is the crucial part of the profile. The determination of DFP is done according to the procedure described in [138]. A spline is fit to the PG depth profile, the distal falloff is the part of such a profile between the global maximum of the profile and a first following downstream minimum (in our representation, this corresponds to the profile part to the right of the maximum). We then define the DFP as the depth ( $x$  position) of the point with a half value between the maximum and the minimum. This value is compared with the proton range, calculated with the use of PSTAR [126], for PMMA of the  $1.19 \text{ g/cm}^3$  density, and the proton beam energies used in the experiment.

#### 4.7.5 Optimisation of image reconstruction

The components of the MLEM formula presented in Section 4.7.2 have previously been optimised according to the principles described in this section.

##### 4.7.5.1 Optimisation targets

In the course of finding the optimal set of input parameters of image reconstruction, we tested combinations of the following options:

1. number of iterations: 1-1000,
2. threshold of energy deposit in maps:
  - lower threshold: 0, 500, 1000, 1500 keV,
  - upper threshold: 7 MeV or none,
3. post-processing - PG depth profile smoothing function (from the `scipy.ndimage` package [139]):
  - smoothing function: Gaussian, median or none,
  - standard deviation of the kernel (corresponding to degree of smoothing): 1-10 pixels,
4. excluded detector regions:
  - dead fibres, listed in Table A.2 in Appendix,
  - empty fibres: if there were any pixels with no entries (apart from the dead fibres), they were excluded,
  - $n$  first and last columns,  $n \in (0, 7)$ ,
  - $m$  layers (starting from the one most distant from the source or phantom),  $m \in (0, 6)$ ,
5. classes of events included: only unique (types a and b) or unique and semi-unique (types a-d),
6. type of the detector response map: hit maps or maps of energy deposits,
7. summing up the maps layer-wise or not,
8. application of the efficiency correction: to the measured data or to SM,

9. accounting for the presence of background: subtraction on the input level prior to the image reconstruction or inclusion of the background term in the MLEM formula.

The quality of the parameter sets was assessed based on the values of the performance metrics (see Section 4.7.5.2), calculated for each image reconstruction variant.

For some of the parameter options listed above (e.g. number of iterations, energy thresholds, smoothing method), it is understandable that they needed to be tested and optimised; others may require some explanation of the reason why they were included in the optimisation.

We started parameter optimisation with the options that worked well in a previous study involving CM image reconstruction [54]: summing the data across layers, subtracting the background from the measured data before feeding them to the MLEM algorithm, and applying the efficiency correction to the measured data (and not to the SM). However, these options were ruled out in the optimisation procedure, as other approaches tested were found to give better results (see Section 5.4). We decided to try to exclude lateral columns, as due to the lack of detector shielding we observed signals generated by primary protons in several upstream detector columns (see Section 4.5.3).

The number of iterations was first roughly optimised independently of the other parameters, yielding a range of values to be considered. Next, the other parameters were compared in direct parameter scans: several parameter sets were chosen, image reconstructions were done looping over the parameter values, and the obtained performance metrics were compared. Several options, e.g. subtracting the background before applying the MLEM formula or thresholds 0 and 1500 keV, yielded consistently worse results across all parameter scans, so they were excluded from the list of possible parameter values. Two parameters: classes of events included and type of detector response map, did not have significant influence on the image reconstruction quality. Thus, we decided to include more event classes (types a-d), as it is generally preferred to use all available information, and chose hit maps over maps of energy deposits. The hit maps content is governed by the Poissonian counting statistics, which is one of the assumptions on which the derivation of the MLEM formula is based, thus this choice is better justified from the mathematical point of view. Finally, a wide scan of the number of iterations was performed again, based on which this parameter was fixed.

#### 4.7.5.2 Performance metrics

The following metrics were used to assess the performance of image reconstruction:

1. Pearson correlation coefficient ( $PCC$ ) between the determined DFPs and calculated proton ranges (PRs) for beam spots S1-S7,
2. Coefficient of determination ( $R^2$ ) between DFPs and PRs for beam spots S1-S7,

3. Root mean squared error (*RMSE*):

$$\text{RMSE} = \sqrt{\frac{\sum_{i,j} (\Delta_{\text{PR}} - \Delta_{\text{DFP}})^2}{2n}}, \quad (10)$$

$$\Delta_{\text{PR}} = \text{PR}_i - \text{PR}_j \quad (11)$$

$$\Delta_{\text{DFP}} = \text{DFP}_i - \text{DFP}_j \quad (12)$$

where  $n = 21$ , number of all pairs of measurements, and  $i, j \in [1, 7]$ , number of beam spots,

4. Standard deviation (*SD*) of the DFPs of the spots with the same  $x$  coordinate ( $S4, S4', S4a-d$ ),

5. Slope of the linear fit to DFPs vs. PRs for all spots ( $s$ ).

The *PCC* quantifies the level of correlation between two variables. It takes values from a range of  $(-1, 1)$ . A strong positive correlation between the DFP and the Bragg peak position was demonstrated experimentally, so it is preferred in our study to have *PCC* as close to 1 as possible.

The  $R^2$  takes values from a range of  $(0, 1)$ . The closer it is to 1, the better the assumed model replicates the measured data. Thus, it is also preferred to be as close to 1 as possible.

The standard deviation *SD* of the profiles of the same depth is a preliminary measure of the image reconstruction reproducibility on different data sets, so it is preferred to be as low as possible.

The *RMSE* can be interpreted as the accuracy of the image reconstruction; thus it is the crucial metric and it was our priority to minimise it.

Finally, the slope  $s$  of the fit line should be close to 1, different slope would mean that an additional calibration would be needed to translate the measured DFP shifts into PR shifts. We did not impose any limit on the intercept, because the DFP is known to be shifted with respect to the BP position, and there could also be a physical shift in the setup.

To select the parameter sets that provided the best image reconstructions, we applied the following cuts on the performance metrics:

- $C_C > 0.99$ ,
- $C_D > 0.8$ ,
- $SD < 1$ ,
- $RMSE < 1.88$ ,
- $0.98 < s < 1.02$ .

After selecting the parameter sets that fulfil the above criteria, we chose the best ones, looking at the shape of the PG depth profiles and the stability of the performance metrics (if a slight change in the parameter value, e.g. incrementing the iteration number by 1, does not cause a drop of performance).

#### 4.8 ANALYSIS OF STATISTICAL PRECISION

The measurements for the beam spots S1-S7 were performed for  $10^{10}$  impinging protons, which is much more than administered to a typical spot during irradiation in proton therapy ( $10^8$ , see Section 1.3.3). Therefore, there was a need to check the image reconstruction performance also for lower proton statistics. Such a study was carried out on subsets of data corresponding to the following statistics: (20, 10, 4, 2, 1)  $\times 10^8$  protons. For each of these statistics, 100 subsets (in the form of LLR output trees) were created with the use of bootstrapping [140]. Then, image reconstruction was performed on each of the subsets, and the spread of the reconstructed DFPs (quantified as a standard deviation) was considered a measure of the statistical precision in DFP determination for a given subset statistics.

## RESULTS

---

In this chapter, we present the results of the 1D CM detector performance test in proton beam conditions. Then, we compare the experimental results with those obtained from the simulated detector response. Finally, we examine the performance of the detector without acceptance gaps based on simulated data.

### 5.1 RATE CAPABILITY

Based on the measurements described in Section 3.2.3.1, average channel occupation for the maximum beam intensity used for patient treatment at HIT was calculated to be 26.4 kcps (assuming uniform channel occupation), while the limit declared by the DAQ manufacturer is 480 kHz [141]. Therefore, the detector can potentially work with up to 18 times higher beam intensities.

### 5.2 DETECTION EFFICIENCY

The map of the detection efficiency per pixel is presented in Figure 4.15f. The mean value of relative pixel efficiencies, after excluding the dead pixels, yielded 0.746. The relative standard deviation of pixel efficiency was 11.39%.

### 5.3 DYNAMIC RANGE

In Figure 5.1, we present an example of a SiPM energy spectrum from an example beam spot S4, for the statistics of  $10^{11}$  protons. The spectrum was calibrated according to the procedure described in Section 3.1.1.2 and corrected for DAQ non-linearity (see Section 4.2.2). In the spectrum, we can see a hint of the characteristic PG peak at the energy of 4.4 MeV. There is no hint of the 6.1 MeV peak though, which could be attributed to too low statistics. The registered energy deposits do not exceed 11 MeV and there is an increase in counts starting from about 6 MeV, which is a sign of saturation. Therefore, we assume that above this value, the energy information obtained could not be considered fully reliable. Nevertheless, the image reconstruction presented in this thesis is not affected by saturation, since it does not exploit the energy information. However, the region of interest for detecting the PG characteristic peaks is not significantly affected by the saturation effect. Hence, we conclude that the detector has an appropriate dynamic range to register PG spectra in proton therapy.

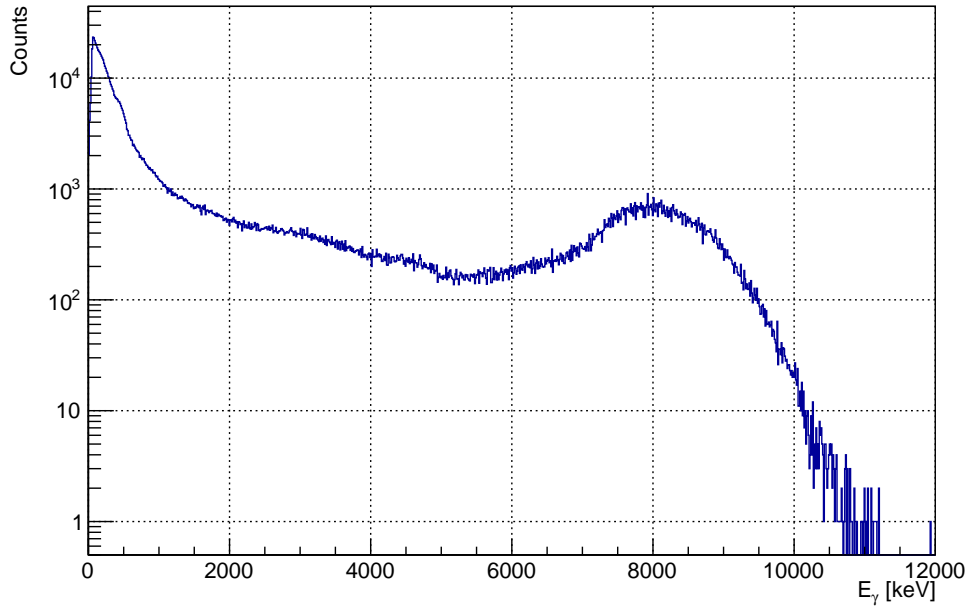


Figure 5.1: Charge spectrum from SiPM 11 of the first layer on the top side of the detector, rescaled to energy units.

#### 5.4 RECONSTRUCTED IMAGES

The image reconstruction was optimised, as described in Section 4.7.5. The following parameters provided the best image reconstruction performance, as well as its stability and good-quality PG depth profiles:

1. number of iterations: 23,
2. threshold of energy deposit in hit maps:
  - lower threshold: 1000 keV,
  - upper threshold: 7 MeV,
3. Post-processing: smoothing with a Gaussian filter with kernel standard deviation of 3 pixels,
4. excluded detector regions:
  - dead fibres,
  - empty fibres,
  - $n = 3$  first and last columns,
  - $m = 0$  further layers,
5. classes of events included: unique and semi-unique (types a-d),
6. input type: hit maps - filled with entries per fibre,
7. not summing up the hit maps layer-wise,



8. efficiency correction applied to: the SM,
9. background considered in: the MLEM formula.

The values of the performance metrics obtained for this configuration of the image reconstruction are summarised in Table 5.1. The profiles for the beam spots S1-

Table 5.1: The values of the performance metrics, obtained for the optimal set of image reconstruction parameters. Full simulation is the simulation with all SiPMs active, i.e. without the acceptance gaps (see Section 5.7). The number of iterations of image reconstruction is given in the last row.

	Experiment	Simulation	Full simulation
$PCC$	0.996	0.9981	0.9998
$R^2$	0.902	0.992	0.992
$RMSE$ [mm]	1.7	1.6	0.4
$SD$ [mm]	0.48	-	-
Slope $s$	1.0102(16)	0.94351(68)	0.999981(92)
Intercept [mm]	3.63(45)	1.01(19)	-1.070(25)
Number of iterations	23	23	600

S7 are presented in Figure 5.2 (top). There, one can see that the distal edge shifts with the beam energy, as expected. The dependence between the distal falloff positions and the corresponding proton ranges is illustrated in Figure 5.2 (bottom), along with a linear fit and a residual plot. In the middle plot, six profiles for the same depth coordinate are presented. One can observe that the shape of the profiles is consistent, the reproducibility of the profile shape and lack of its dependence from the beam lateral position within the range of  $\pm 1$  cm. The variation of the obtained profiles here is quantified by the  $SD$  parameter (described in Section 4.7.5.2). Apart from the desired behaviour of the distal edge, the rest of the profile presents some unfavourable effects. Although the profile widens with beam energy, as expected, additional wide peaks appear in the profile structure. Moreover, the reconstructed gamma intensity is too small in the entrance region: we would expect to see the rising edge of the profile around the phantom border and then a slow increase in the middle region of the profile (see, e.g., the profile in Figure 1.4). There are also some artefacts in the regions outside the phantom: the relative gamma count increases towards the image edges, even though we do not expect any events there. Despite all the described flaws of the profiles, we conclude that the image reconstruction performs very well, as indicated by the parameter metrics: the  $RMSE$  yields 1.7 mm. This metric defines the image reconstruction accuracy. The reconstructed DFPs are strongly correlated with the calculated proton ranges, as indicated by high values of both the  $PCC = 0.996$  and  $R^2 = 0.902$ . The slope of the DFP-proton range dependence is close to unity: 1.0102(16), the intercept is positive: 3.63(45) mm. The standard deviation of the same-depth profiles' DFP equals 0.48 mm.

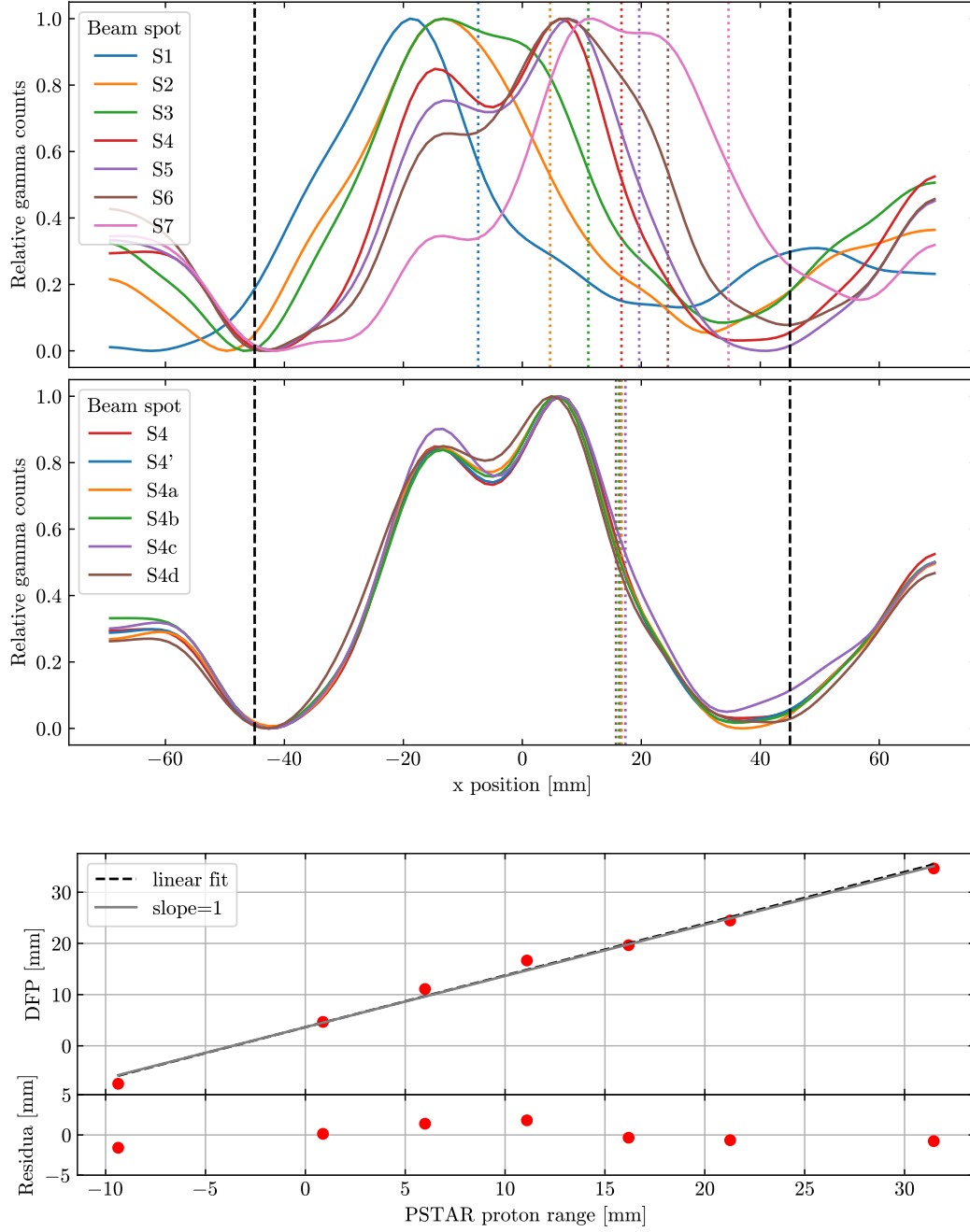


Figure 5.2: Top: PG depth profiles for S1-S7, black dashed line marks the phantom borders and the dotted colour lines correspond to the DFP positions determined for the corresponding profiles; middle: PG depth profiles for S4, S4', S4a-d; bottom: DFP vs. PSTAR proton range, with a linear fit (dashed line) and a reference line with a slope equal to 1 (solid line).

### 5.5 ANALYSIS OF STATISTICAL PRECISION

For each of 100 subsets of the experimental data (created for each investigated sample size, according to the procedure described in Section 4.8), image reconstruction was performed. The configuration of the image reconstruction was the same as for the image reconstruction of the full-size data samples. We summarise

the results of these image reconstructions in a box plot, presented in Figure 5.3 for beam spots S1-S7 (arranged left to right). In each panel, the distribution of the reconstructed DFP values is presented for each sample size. The rectangle (box) marks the interquartile range (IQR) between the quartiles Q1 and Q3. The orange line on the rectangle denotes the median. The whiskers extend to the furthest data point that falls into a range of  $1.5 \times \text{IQR}$ , starting from the box edge. Outliers are marked with empty circles. There, one can see that the trend is, with some exceptions, that the smaller the data sample, the larger the IQR, which is expected, since the image reconstruction suffers from the statistical fluctuations in the input data. The IQR for beam spots S1-S6 is below 3 mm, while for the deepest spot S7 it is larger, up to about 5 mm for the lowest investigated statistics. Another observed effect is the drift of median with sample size, while we would expect it to be constant. The magnitude of the effect is between 0.46 mm (S3) and 1.8 mm (S6). No clear pattern is observed regarding the decrease or increase of the median value with sample size.

Another, more popular in the literature, measure of the image reconstruction quality is the standard deviation of the obtained DFPs:  $\sigma_{\text{DFP}}$ . The standard deviations for all beam spots and examined sample sizes are presented in Figure 5.4. There, one can see that  $\sigma_{\text{DFP}}$  depends not only on the sample statistics, but also on the Bragg peak position in the phantom. One can observe a consistent pattern across all the sample sizes: the  $\sigma_{\text{DFP}}$  is the lowest in spots S1 and S4; in spots S2, S3, S5 and S6, the  $\sigma_{\text{DFP}}$  is higher, in the range of 1–2.5 mm, and the highest  $\sigma_{\text{DFP}}$  is observed for spot S7 (the deepest one). A possible explanation for such behaviour can be the irregularity of the collimator pattern. The broader the slits in certain collimator region, the worse the imaging resolution would be in the corresponding detector region. This is the possible cause for the worse performance in the last spot. Moreover, the neutron background is larger at higher energies, which could also contribute to the deterioration of the achieved DFP precision.

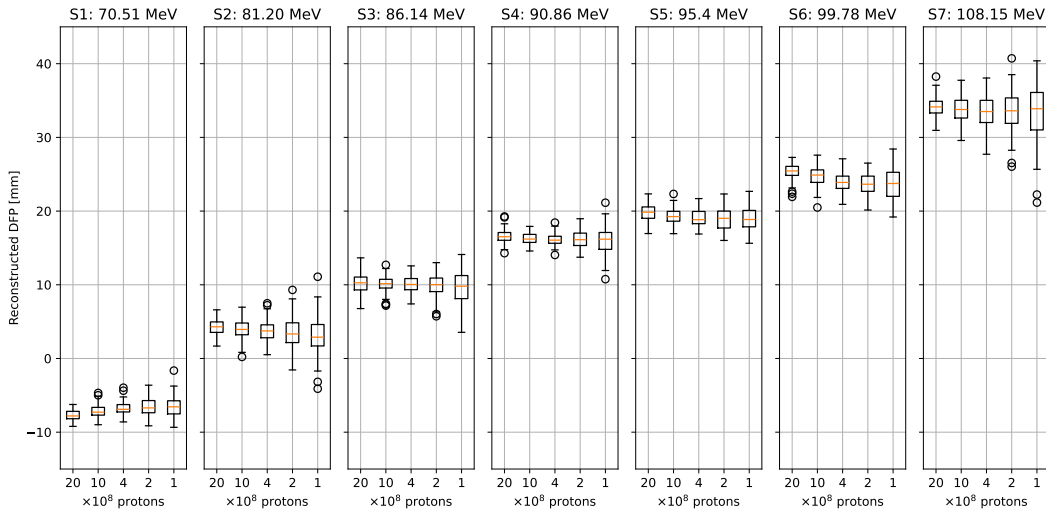


Figure 5.3: Reconstructed DFP vs. sample size for beam spots S1-S7.

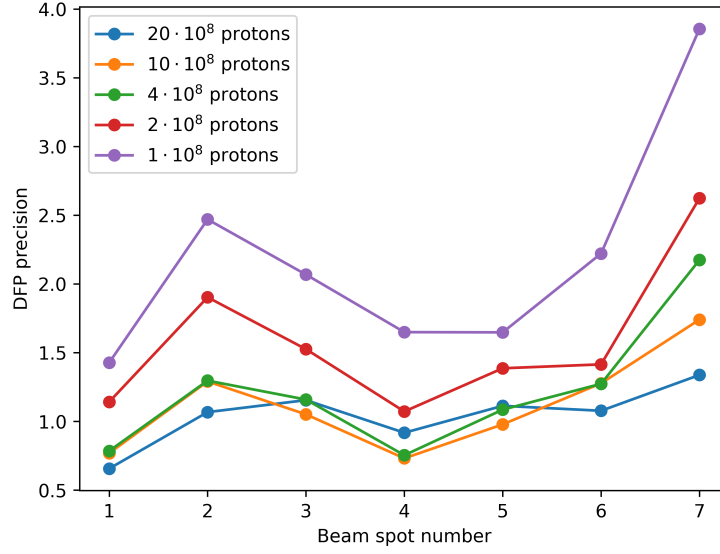


Figure 5.4: DFP precision ( $\sigma_{\text{DFP}}$ ) vs. number of the beam spot. Different line colours correspond to different statistics of data used as input (see legend).

## 5.6 SIMULATION VS. EXPERIMENT

To verify the results of the experimental detector tests, data from a realistic simulation reproducing the experimental setup were prepared. The data files from the simulation were processed in the same way as the experimental ones and the image reconstruction was performed on both data sets with the same parameters (found in a process of optimisation on experimental data). The resulting PG depth profiles are presented in Figure 5.5, and the obtained values of performance metrics are summarised in Table 5.1. The *RMSE* for the simulation data is 1.6 mm, slightly better than for the experimental data (1.7 mm). Both the *PCC* and *R*<sup>2</sup> were also better (0.9981 and 0.992, respectively), but the slope was further away from 1. The intercept lowered with respect to the experimental data to 1.01(19) mm. The standard deviation of the same beam spot profiles was not determined, as only one data set was simulated per beam spot. The simulated profiles presented in Figure 5.5 are very similar to the experimental ones, all the effects present in the experimental results are also observed in the simulation: the change of the profile shape with beam energy, the wide peaks in the profiles, the artefacts in the regions outside of the phantom. Based on these observations and on the similarity of the performance metrics, we can conclude that the simulation is accurate and correctly predicts all major effects observed in the analysis of experimental data.

## 5.7 NON-FILTERED SIMULATION

An additional study was performed to assess the influence of the acceptance gaps on the image reconstruction performance: the full simulated data set without accounting for acceptance gaps (referred to as non-filtered) was processed in the same way as the experimental data, with the same software configuration. Only the number of iterations was re-optimised and the new optimum was found to be

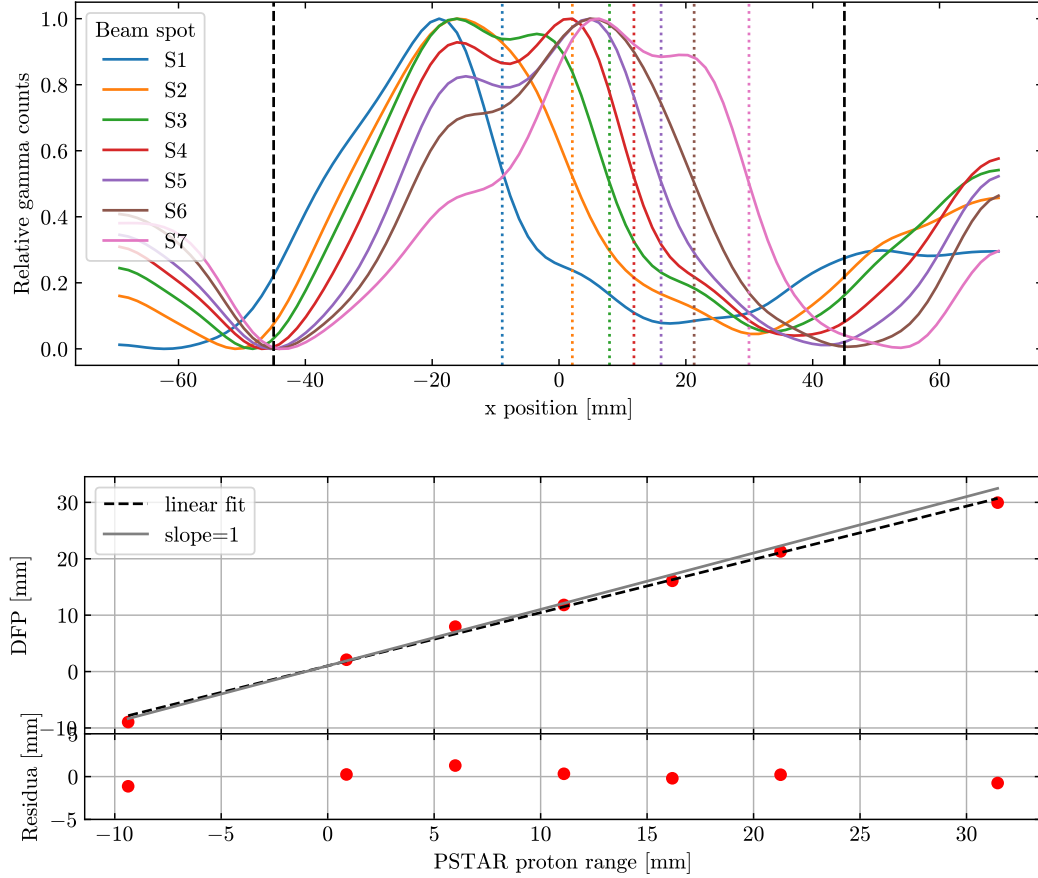


Figure 5.5: Top: Simulated PG depth profiles for S1-S7, colour coding the same as in Figure 5.2; bottom: simulated DFP vs. PSTAR proton range, with a linear fit (dashed line) and a reference line with a slope equal to 1 (solid line).

much higher: 600 iterations. The resulting PG depth profiles are presented in Figure 5.6. The profiles are of much better shape than the ones reconstructed from data with acceptance gaps, both simulated and experimental. Firstly, the profiles start earlier: the rising edges are located at the phantom proximal border, as expected, and do not shift with the beam energy, which is also physically correct, as the gammas are emitted along the whole proton path, regardless of the range. No artefacts are present in the regions outside the phantom. Moreover, the performance metrics are better than for the filtered case (see Table 5.1), with *RMSE* of 0.4 mm, *PCC* of 0.9998, slope *s* of 0.999981(92) (equal to 1 within uncertainty) and slightly negative intercept of  $-1.070(25)$  mm.

The increase of the iteration number for the non-filtered simulation was only possible, because there were no distortions or wide peaks in the profiles. These distortions were present in both the experimental data and the filtered simulation, and were amplified with each iteration, leading to the deterioration of the image reconstruction performance. For completeness, in the appendix A we present the image reconstruction after 600 iterations for the experimental data in Figure A.1 and for simulated data with acceptance gaps in Figure A.2. In both cases, one can see the amplified artefacts in the PG depth profiles. Moreover, one can observe that the residua associated with the linear fit to the dependence of DFPs vs.

proton ranges are larger than in Figure 5.2 (where the number of iterations was optimal), which is a sign of a poorer image reconstruction performance. The values of performance metrics associated with the presented reconstructed images were also consistently poorer than for the optimal number of iterations. We also present the full simulation profile after 23 iterations (the number optimal for data with acceptance gaps) in Figure A.3. There, one can see that the profiles are smooth, but their shape is not yet optimal, definitely more iterations are needed.

The comparison of the image reconstruction performance for filtered and non-filtered data leads us to the conclusion that all the unfavourable effects in the experimental profiles, along with the poorer values of the performance metrics, are likely to have their origin in the presence of the acceptance gaps.

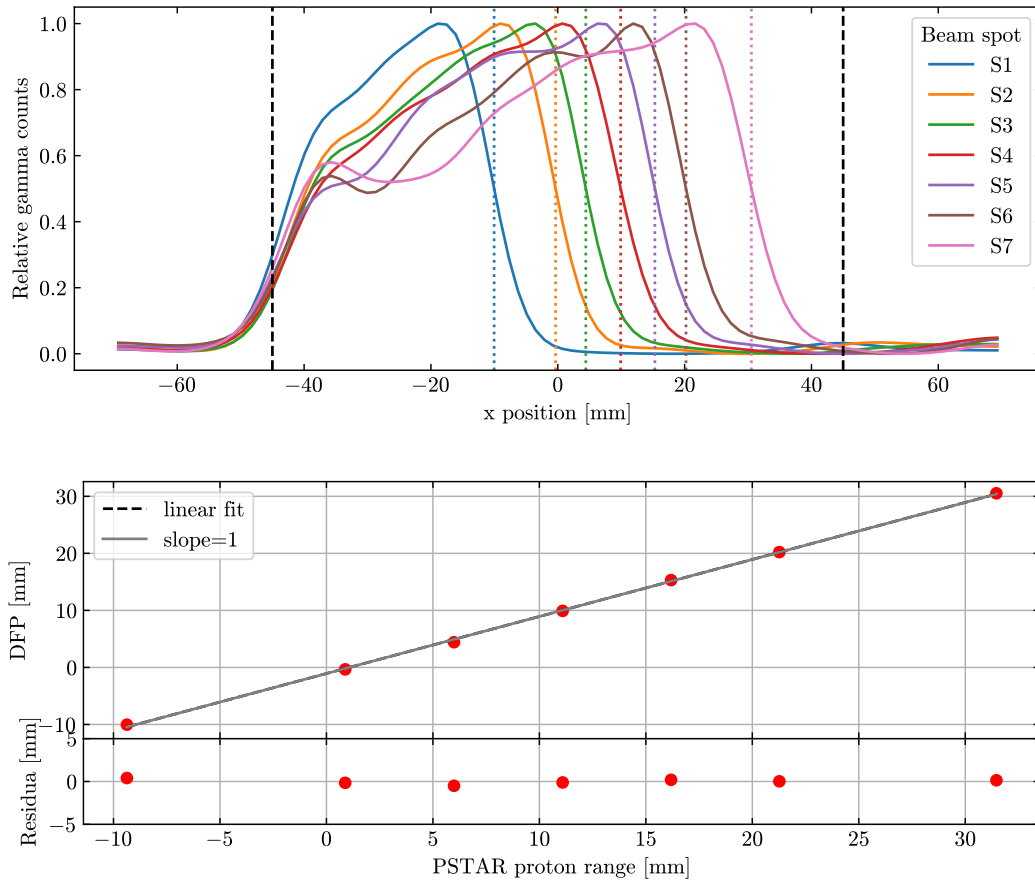


Figure 5.6: Same as in Figure 5.5, but the simulation results were not filtered.

## DISCUSSION AND OUTLOOK

---

### 6.1 DETECTOR PERFORMANCE

Based on the rate capability study described in Section 5.1, we conclude that the detector is operable rate-wise under synchrotron conditions. The channel occupation at maximum possible intensity of the synchrotron beam was 18 times lower than the DAQ limit. Therefore, it can be assumed that the detector can operate also in cyclotron conditions, where the beam intensities, and thus also the detector rates, are about 10 times higher than at a synchrotron [55].

In the analysis of the DFPs of the profiles obtained for different lateral positions of beam spots (S4, S4', S4a-d, see Figure 5.2, middle panel), we obtained the DFPs standard deviation of 0.48 mm, which is below the  $\sigma_{\text{DFP}}$  obtained for the nearest investigated statistics corresponding to  $10^9$  protons. Thus, we confirm that the detector is not sensitive to changes in the lateral spot position of the beam by  $\pm 1$  cm.

The main flaw in the experimental setup, which limited the detector performance, was the presence of acceptance gaps due to several non-working SiPMs (the issue was described in Section 3.1.2). When we repeated the analysis and image reconstruction on a simulated data set with all SiPMs working (Section 5.7), we obtained much better profile shapes, as well as the performance metrics. Notably, *RMSE* decreased from 1.6 mm (simulation with acceptance gaps) to 0.4 mm, suggesting that eliminating acceptance gaps could improve detector precision in terms of range shift determination up to 4 times. This number has to be taken with caution, because we reason based on the simulated data. We conclude that in the next detector generation particular care must be taken to ensure that all detector pixels are active, as it turned out to be crucial for the detector performance.

### 6.2 PG DEPTH PROFILES - EXPERIMENTAL AND SIMULATED

The simulated profiles are very similar to the experimental ones, both qualitatively, by looking at the profiles' shapes, and quantitatively, by comparing the performance metrics. Particularly, similar *RMSE* values (1.7 mm for the experimental data and 1.6 mm for the simulated data) were obtained. We conclude that our simulation realistically and accurately reproduces the 1D CM experiment.

### 6.3 CLINICAL FEASIBILITY, SIGNIFICANCE

The study described in this thesis is the first experimental test of a coded-mask gamma camera used for beam range verification in proton therapy in clinical conditions. Prior to this test, two articles were published on the coded-mask approach to proton beam monitoring: [53] (presenting simulation data) and [54] (presenting simulation data and the results of laboratory tests), the latter published by

our group. The achieved precisions declared in these articles for the statistics of  $10^8$  protons were, respectively, 2.1 mm (for the lowest tested beam energy of 122.7 MeV) and 0.72 mm (averaged over several beam spots in the energy range of 85.9-107.9 MeV).

There are also several solutions comparable to ours that were investigated experimentally or by means of simulations: knife-edge slit (KES) systems [40, 27], and multi-parallel slit (MPS) systems [50, 51]. Of these two approaches, the KES systems are the most mature, with a record of in-human tests [27, 142]. We compare the beam range reconstruction precision ( $\sigma_{\text{DFP}}$ ) obtained by these systems in the conditions as close as possible to the conditions of our experiment. In [40], a precision of 2 mm at a beam energy of 160 MeV was obtained (there, the statistics was slightly larger:  $1.4 \times 10^8$  protons). The other clinical solution [27] provides also 2 mm precision for aggregated spots, with an energy range of 100-160 MeV, for  $10^8$  protons. In a simulation study [50], the precision is 1.30-1.66 mm, depending on the camera geometry settings. This was verified for the energy 160 MeV and the standard statistics of  $10^8$  protons. The experimental study of a MPS setup by another group [51] yielded a precision of 1.5 mm at 99.68 MeV with  $10^8$  protons. Our result of 1.7 mm precision with  $10^8$  protons and 90.86 MeV is comparable to the precisions obtained by the presented detectors. However, removing the acceptance gaps is expected to significantly improve our detector's performance, yielding better precision than any of the presented systems.

#### 6.4 PROSPECTS OF MOVING TO 2D CM IMAGING

The setup can be extended to enable 2D imaging, provided that the method of determining the position in the dimension along the fibre is improved. Currently, it is not sufficient, due to reasons described in Section 3.1.1. The planned modification of the active detector part in the next detector iteration is increasing the attenuation along the fibre, which is expected to enhance the position resolution.



## SUMMARY AND CONCLUSIONS

---

In this thesis, a process of construction of a coded-mask gamma camera and the results of its first experimental test under proton beam conditions are presented.

Chapter 1 provides the theoretical background and the motivation for building a coded-mask gamma camera as a solution for proton beam range verification in proton therapy.

In Chapter 2, we characterise the SiFi-CC project and discuss how it addresses the issues observed in prompt-gamma-based monitoring of proton therapy; we also describe the process of optimising setup components, particularly the DAQ system. We conclude that the optimal DAQ system among the tested options is the TOFPET2c and should therefore be used in the experimental setup. We also outline the previous steps that led to the development of the current version of the detector, including a small-scale prototype and a pilot CM study with radioactive sources.

In Chapter 3, the detector setup and experimental conditions for studying the CM gamma camera with a proton beam are presented. The test was carried out under clinical conditions at HIT. During the test, a PMMA phantom was irradiated with proton beams of energies ranging from 70.15 MeV to 108.15 MeV and of three beam intensities of  $8 \times 10^7$ ,  $6 \times 10^8$ , and  $3.2 \times 10^9$  protons/s. The PGs emitted from the phantom were registered with the scintillation-fibre-based CM gamma camera operating in 1D-imaging modality.

Chapter 4 contains the description of data analysis methods and algorithms used (e.g. LLR, MLEM, DFP determination), along with a summary of several auxiliary studies aimed to better understand the data and the detector low-level performance. Also, the configuration of the simulation application is provided in this part.

In Chapter 5, the results obtained based on both experimental and simulation data are confronted, followed by their detailed discussion in Chapter 6. The CM gamma camera in the 1D modality achieved the precision of the DFP determination of 1.7 mm with statistics of  $10^8$  protons, which is comparable to the typical statistics per distal beam spot in clinical irradiation. The beam energy for this irradiation was 90.68 MeV. The experimental results were shown to be consistent with those obtained for simulation data: the shape of the reconstructed profiles and the obtained performance metrics were very similar in both cases. In the experiment, the detector had acceptance gaps, which were also accounted for in the simulation by filtering out the dead pixels. However, the same simulation without the filtering (i.e., with all detector pixels active) proved to achieve 4 times better performance in terms of the range shift determination. Therefore, there is still space for improving the detector performance. In terms of hit rate, the setup proved to be compatible with synchrotron conditions, with the prospect of working also under the more demanding cyclotron conditions. The performance of the setup is already comparable to that of similar available solutions for PG proton therapy

monitoring (KES, MPS), and it can be further improved if the conclusions from the present work are applied.

The main objective of this thesis was to demonstrate the feasibility of using a coded-mask gamma camera for proton therapy monitoring. The presented research constitutes a proof-of-principle for this proposed solution and thus provides a basis for a novel method of monitoring the beam range with potential for clinical application.

## APPENDIX

Table A.1: List of dead SiPMs.

Dead SiPM IDs	Side
34	bottom
46	
462	top
426	
437	
397	
398	
409	
420	
421	
422	
393	

Table A.2: List of dead fibers, i.e. the fibers that were connected to dead SiPMs.

Layer ID	Fiber ID	Layer ID	Fiber ID
0	50	2	51
0	51	2	52
0	52	2	53
0	53	3	2
1	11	3	3
1	12	3	4
1	35	3	5
1	36	3	26
1	50	3	27
1	51	3	48
1	52	3	49
1	53	3	50
2	2	3	51
2	3	3	52
2	4	3	53
2	5	4	4
2	11	4	5
2	12	4	26
2	26	4	27
2	27	5	4
2	35	5	5
2	36	5	26
2	48	5	27
2	49	6	20
2	50	6	21

Table A.3: DAQ parameters.

General DAQ settings	
Overvoltage	8 V
Preset time	30 s
Pre BDV	30 V
BDV	33 V
Threshold T1	20
Threshold T2	20
Threshold E	22
Hardware trigger settings	
type	builtin
threshold	1
pre_window	3
post_window	15
coincidence_window	3
single_acceptance_period	1000
single_acceptance_length	0
global.disc_lsb_T1	60

Table A.4: List of runs for rate capability assessment. I - intensity;  $N_{\text{total}} = \Sigma_i N_{i \text{ total}}$  - total counts in the spill regions;  $N_{\text{background calc.}}$  - background contribution to the spill regions, calculated according to Equation (7) in Section 4.2.4;  $N_{\text{spills}} = N_{\text{total}} - N_{\text{background calc.}}$  - counts associated with beam spills.

Run ID	I [protons/s]	E [MeV]	$\Sigma_i N_{i \text{ total}}$	$N_{\text{background calc.}}$	$N_{\text{spills}}$
496	$3.2 \times 10^9$	108.15	30 201 200	844 945	$29\,356\,300 \pm 5500$
495	$6 \times 10^8$	108.15	36 139 700	3 865 110	$32\,274\,600 \pm 6300$
494	$8 \times 10^7$	108.15	58 006 100	26 205 400	$31\,800\,700 \pm 9600$
493	$3.2 \times 10^9$	90.86	23 217 000	730 090	$22\,486\,900 \pm 4900$
492	$6 \times 10^8$	90.86	27 696 600	3 461 950	$24\,234\,700 \pm 5600$
491	$8 \times 10^7$	90.86	48 503 600	24 504 200	$23\,999\,400 \pm 9000$

Table A.5: List of runs for rate overvoltage scan.

Run ID	Overvoltage [V]
552	4
554	6
551	8
553	12
556	14

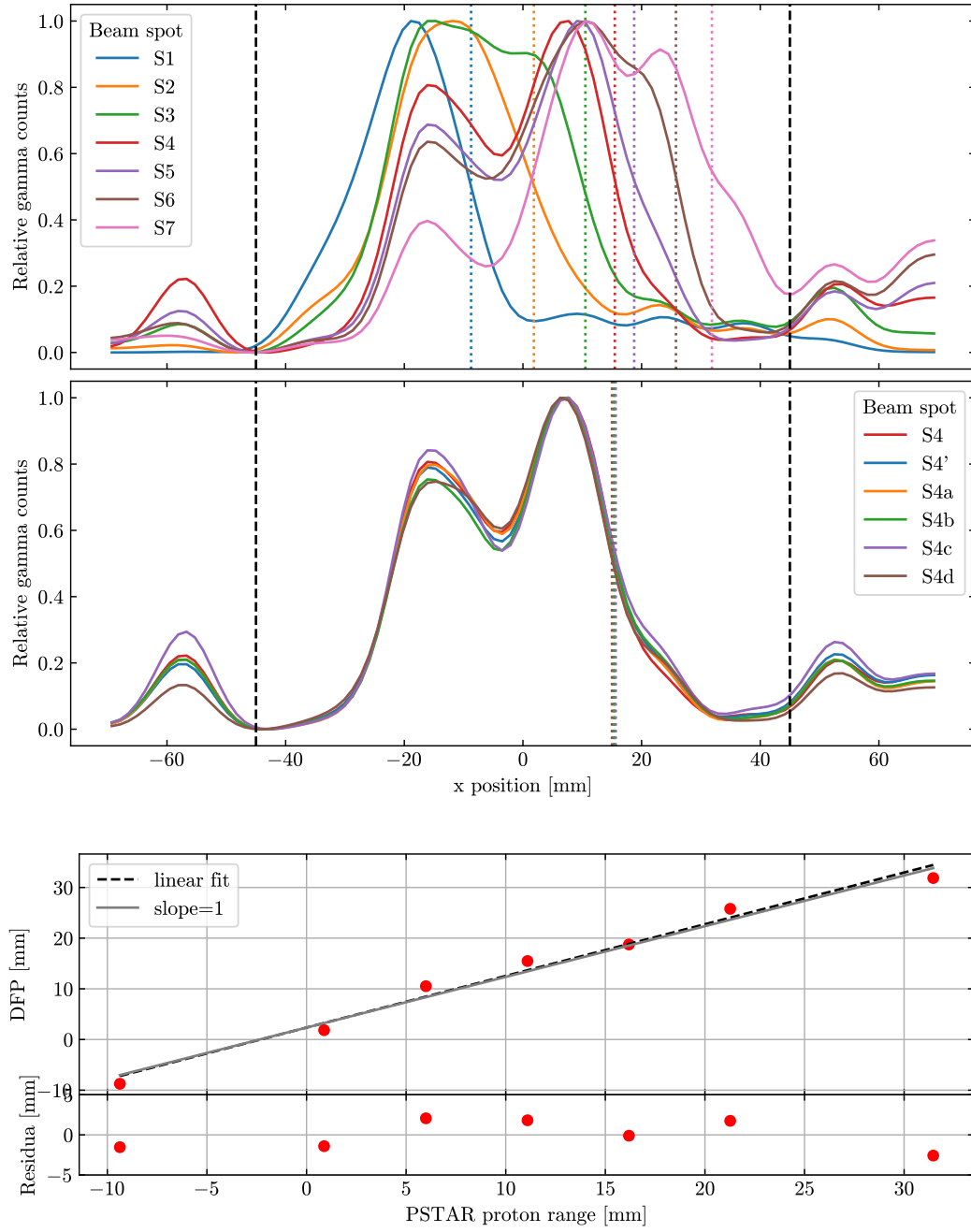


Figure A.1: Same as in Figure 5.2, but the number of iterations is 600.

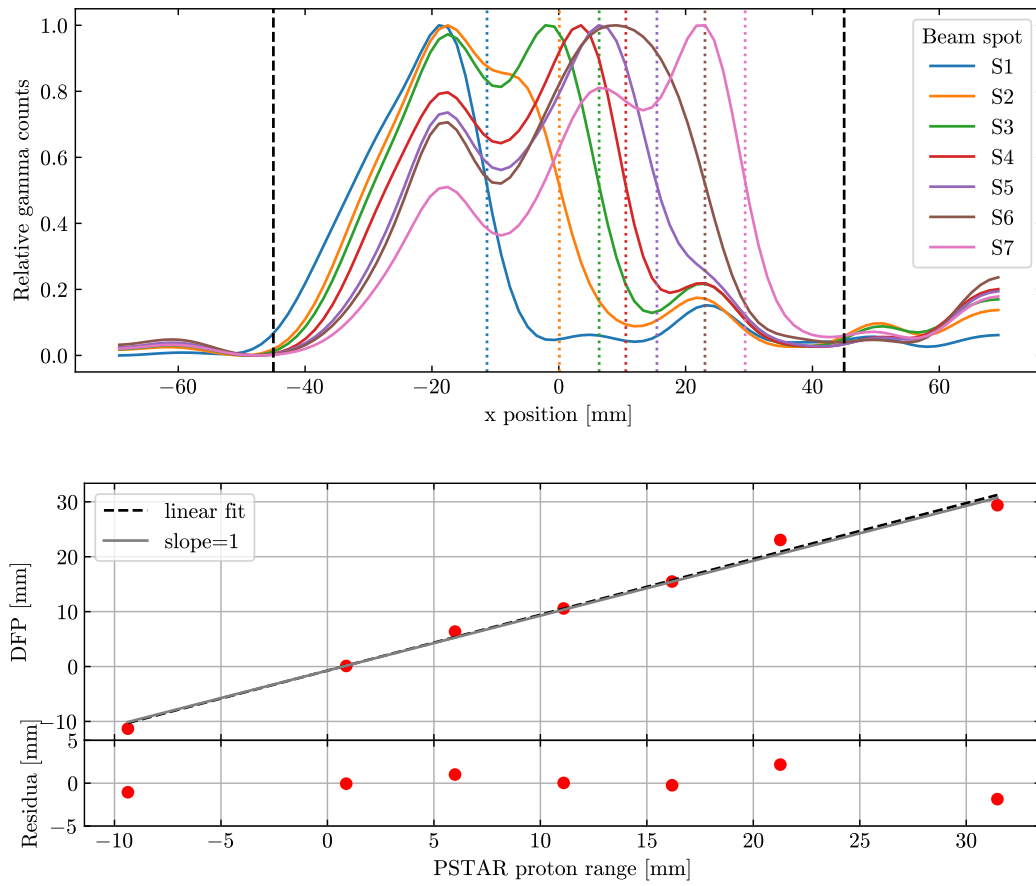


Figure A.2: Same as in Figure 5.5, but the number of iterations is 600.



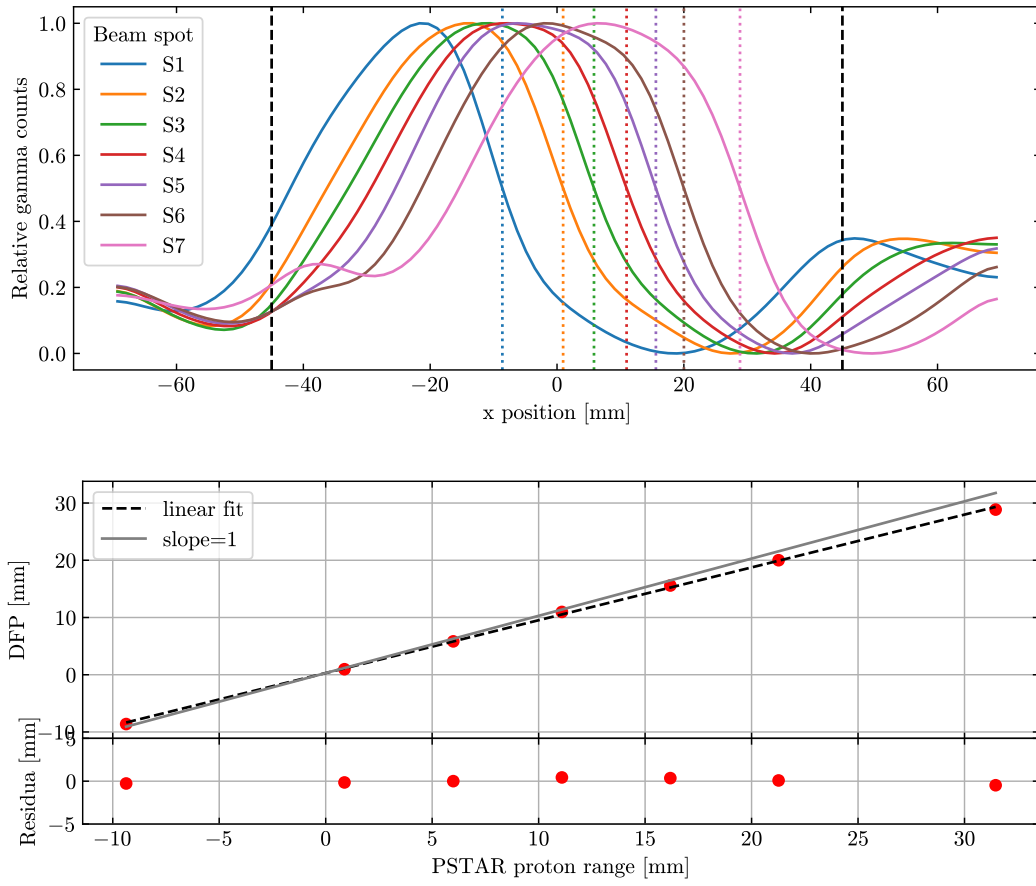


Figure A.3: Same as in Figure 5.6, but the number of iterations is 23.



## BIBLIOGRAPHY

---

- [1] Eurostat. Causes of death statistics. [https://ec.europa.eu/eurostat/statistics-explained/index.php?title=Causes\\_of\\_death\\_statistics](https://ec.europa.eu/eurostat/statistics-explained/index.php?title=Causes_of_death_statistics) (Accessed: 2024-31-12).
- [2] Rebecca L. Siegel, Kimberly D. Miller, Hannah E. Fuchs, and Ahmedin Jemal. Cancer statistics, 2021. *CA: A Cancer Journal for Clinicians*, 71(1):7–33, January 2021.
- [3] C.-M.C. Ma and T. Lomax. Proton and carbon ion therapy. CRC Press, 2012, <http://dx.doi.org/10.1201/b13070>.
- [4] Bleddyn Jones. Why RBE must be a variable and not a constant in proton therapy. *The British Journal of Radiology*, 89(1063):20160116, July 2016.
- [5] Kaitlyn Lapen and Yoshiya Yamada. The development of modern radiation therapy. *Current Physical Medicine and Rehabilitation Reports*, 11(2):131–138, April 2023.
- [6] H. Paganetti. Proton Therapy Physics. CRC Press, 2012, <http://dx.doi.org/10.1201/b22053>.
- [7] Wayne D Newhauser and Rui Zhang. The physics of proton therapy. *Physics in Medicine and Biology*, 60(8):R155–R209, 2015.
- [8] H. Bethe. Zur theorie des durchgangs schneller korpuskularstrahlen durch materie. *Annalen der Physik*, 397(3):325–400, January 1930.
- [9] Particle Data Group. The review of particle physics (2022), passage of particles through matter. <https://pdg.lbl.gov/2022/reviews/rpp2022-rev-passage-particles-matter.pdf> (Accessed: 2024-31-12).
- [10] Harald Paganetti. Relative biological effectiveness (RBE) values for proton beam therapy. Variations as a function of biological endpoint, dose, and linear energy transfer. *Physics in Medicine and Biology*, 59(22):R419–R472, October 2014.
- [11] Harald Paganetti. Relating proton treatments to photon treatments via the relative biological effectiveness—should we revise current clinical practice? *International Journal of Radiation Oncology\*Biophysics*, 91(5):892–894, April 2015.
- [12] Harald Paganetti, Eleanor Blakely, Alejandro Carabe-Fernandez, David J. Carlson, Indra J. Das, Lei Dong, David Grosshans, Kathryn D. Held, Radhe Mohan, Vitali Moiseenko, Andrzej Niemierko, Robert D. Stewart, and Henning Willers. Report of the AAPM TG-256 on the relative biological effectiveness of proton beams in radiation therapy. *Medical Physics*, 46(3), February 2019.

- [13] Armin Lühr, Cläre von Neubeck, Mechthild Krause, and Esther G.C. Troost. Relative biological effectiveness in proton beam therapy – current knowledge and future challenges. *Clinical and Translational Radiation Oncology*, 9:35–41, February 2018.
- [14] Stephen Joseph McMahon. The linear quadratic model: usage, interpretation and challenges. *Physics in Medicine and Biology*, 64(1):01TR01, 2018.
- [15] Robert R. Wilson. Radiological use of fast protons. *Radiology*, 47(5):487–491, November 1946.
- [16] J. H. Lawrence and C. A. Tobias. Pituitary irradiation with high-energy proton beams: a preliminary report. *Cancer Research*, 18(2):121–134, February 1958.
- [17] Börje Larsson, Lars Leksell, Bror Rexed, Patrick Sourander, William Mair, and Bengt Andersson. The High-Energy Proton Beam as a Neurosurgical Tool. *Nature*, 182(4644):1222–1223, November 1958.
- [18] R N Kjellberg, W H Sweet, W M Preston, and A M Koehler. The Bragg peak of a proton beam in intracranial therapy of tumors. *Transactions of the American Neurological Association (U.S.)*, 87, 1 1962.
- [19] Particle Therapy Co-Operative Group. Particle therapy facilities in clinical operation. <https://www.ptcog.site/index.php/facilities-in-operation-public> (Accessed: 2024-31-12).
- [20] A. Koehler, R. Schneider, and J. Sisterson. Range modulators for protons and heavy ions. *Nuclear Instruments and Methods*, 131(3):437–440, December 1975.
- [21] A. M. Koehler, R. J. Schneider, and J. M. Sisterson. Flattening of proton dose distributions for large-field radiotherapy. *Medical Physics*, 4(4):297–301, July 1977.
- [22] Tatsuaki Kanai, Kiyomitsu Kawachi, Yoshikazu Kumamoto, Hirotugu Ogawa, Takanobu Yamada, Hideo Matsuzawa, and Tetsuo Inada. Spot scanning system for proton radiotherapy. *Medical Physics*, 7(4):365–369, July 1980.
- [23] Eros Pedroni, Reinhard Bacher, Hans Blattmann, Terence Böhringer, Adolf Coray, Antony Lomax, Shixiong Lin, Gudrun Munkel, Stefan Scheib, Uwe Schneider, and Alexander Tourovsky. The 200-MeV proton therapy project at the Paul Scherrer Institute: Conceptual design and practical realization. *Medical Physics*, 22(1):37–53, January 1995.
- [24] Binwei Lin, Feng Gao, Yiwei Yang, Dai Wu, Yu Zhang, Gang Feng, Tangzhi Dai, and Xiaobo Du. FLASH Radiotherapy: History and Future. *Frontiers in Oncology*, 11, May 2021.
- [25] E.C. Daugherty, A.E. Mascia, M.G.B. Sertorio, Y. Zhang, E. Lee, Z. Xiao, J. Speth, J. Woo, C. McCann, K. Russell, L. Levine, R. Sharma, D. Khuntia,

- J.P. Perentesis, and J.C. Breneman. FAST-01: Results of the First-in-Human Study of Proton FLASH Radiotherapy. *International Journal of Radiation Oncology \*Biology\*Physics*, 114(3):S4, November 2022.
- [26] Anthony E. Mascia, Emily C. Daugherty, Yongbin Zhang, Eunsin Lee, Zhiyan Xiao, Mathieu Sertorio, Jennifer Woo, Lori R. Backus, Julie M. McDonald, Claire McCann, Kenneth Russell, Lisa Levine, Ricky A. Sharma, Dee Khuntia, Jeffrey D. Bradley, Charles B. Simone, John P. Perentesis, and John C. Breneman. Proton FLASH Radiotherapy for the Treatment of Symptomatic Bone Metastases: The FAST-01 Nonrandomized Trial. *JAMA Oncology*, 9(1):62, January 2023.
- [27] Jonathan Berthold, Chirasak Khamfongkhrua, Johannes Petzoldt, Julia Thiele, Tobias Hölscher, Patrick Wohlfahrt, Nils Peters, Angelina Jost, Christian Hofmann, Guillaume Janssens, Julien Smeets, and Christian Richter. First-In-Human Validation of CT-Based Proton Range Prediction Using Prompt Gamma Imaging in Prostate Cancer Treatments. *International Journal of Radiation Oncology \*Biology\*Physics*, 111:1033--1043, 11 2021.
- [28] Nuclear Physics European Collaboration Committee. Nuclear Physics For Medicine. <https://www.nupec.org/pub/npm2014.pdf> (Accessed: 2024-31-12).
- [29] Jaeman Son, Se Lee, Youngkyung Lim, Sung Park, Kwanho Cho, Myonggeun Yoon, and Dongho Shin. Development of Optical Fiber Based Measurement System for the Verification of Entrance Dose Map in Pencil Beam Scanning Proton Beam. *Sensors*, 18(1):227, January 2018.
- [30] Katia Parodi and Jerimy C. Polf. *In vivo* range verification in particle therapy. *Medical Physics*, 45(11), November 2018.
- [31] M. Fischetti, G. Baroni, G. Battistoni, G. Bisogni, P. Cerello, M. Ciocca, P. De Maria, M. De Simoni, B. Di Lullo, M. Donetti, Y. Dong, A. Embriaco, V. Ferrero, E. Fiorina, G. Franciosini, F. Galante, A. Kraan, C. Luongo, M. Magi, C. Mancini-Terracciano, M. Marafini, E. Malekzadeh, I. Mattei, E. Mazzoni, R. Mirabelli, A. Mirandola, M. Morrocchi, S. Muraro, V. Patera, F. Pennazio, A. Schiavi, A. Sciubba, E. Solfaroli Camillocci, G. Sportelli, S. Tampellini, M. Toppi, G. Traini, S. M. Valle, B. Vischioni, V. Vitolo, and A. Sarti. Inter-fractional monitoring of  $^{12}\text{C}$  ions treatments: results from a clinical trial at the CNAO facility. *Scientific Reports*, 10(1), November 2020.
- [32] Renato Félix-Bautista, Laura Ghesquière-Diérickx, Pamela Ochoa-Parra, Laurent Kelleter, Gernot Echner, Jürgen Debus, Oliver Jäkel, Mária Martišková, and Tim Gehrke. Inhomogeneity detection within a head-sized phantom using tracking of charged nuclear fragments in ion beam therapy. *Physics in Medicine and Biology*, 69(22):225003, November 2024.
- [33] M. Marafini, L. Gasparini, R. Mirabelli, D. Pinci, V. Patera, A. Sciubba, E. Spiriti, D. Stoppa, G. Traini, and A. Sarti. MONDO: a neutron tracker for particle therapy secondary emission characterisation. *Physics in Medicine and Biology*, 62(8):3299–3312, March 2017.

- [34] Sonja M. Schellhammer, Ilker Meric, Steffen Löck, and Toni Kögler. Hybrid treatment verification based on prompt gamma rays and fast neutrons: multivariate modelling for proton range determination. *Frontiers in Physics*, 11, December 2023.
- [35] Gabriela Llosá and Magdalena Rafecas. Hybrid PET/Compton-camera imaging: an imager for the next generation. *The European Physical Journal Plus*, 138(3), March 2023.
- [36] Maria Giuseppina Bisogni, Andrea Attili, Giuseppe Battistoni, Nicola Belcari, Niccolò Camarlinghi, Piergiorgio Cerello, Silvia Coli, Alberto Del Guerra, Alfredo Ferrari, Veronica Ferrero, Elisa Fiorina, Giuseppe Giraud, Eleftheria Kostara, Matteo Morrocchi, Francesco Pennazio, Cristiana Peroni, Maria Antonietta Piliero, Giovanni Pirrone, Angelo Rivetti, Manuel D. Rolo, Valeria Rosso, Paola Sala, Giancarlo Sportelli, and Richard Wheadon. INSIDE in-beam positron emission tomography system for particle range monitoring in hadrontherapy. *Journal of Medical Imaging*, 4(1):011005, December 2016.
- [37] Chul-Hee Min, Chan Hyeong Kim, Min-Young Youn, and Jong-Won Kim. Prompt gamma measurements for locating the dose falloff region in the proton therapy. *Applied Physics Letters*, 89(18), October 2006.
- [38] Laurent Kelleter, Aleksandra Wrońska, Judith Besuglow, Adam Konefał, Karim Laihem, Johannes Leidner, Andrzej Magiera, Katia Parodi, Katarzyna Rusiecka, Achim Stahl, and Thomas Tessonier. Spectroscopic study of prompt-gamma emission for range verification in proton therapy. *Physica Medica*, 34:7–17, February 2017.
- [39] Christian Richter, Guntram Pausch, Steffen Barczyk, Marlen Priegnitz, Isabell Keitz, Julia Thiele, Julien Smeets, Francois Vander Stappen, Luca Bombelli, Carlo Fiorini, Lucian Hotoiu, Irene Perali, Damien Prieels, Wolfgang Enghardt, and Michael Baumann. First clinical application of a prompt gamma based *in vivo* proton range verification system. *Radiotherapy and Oncology*, 118(2):232–237, February 2016.
- [40] Yunhe Xie, El Hassane Bentefour, Guillaume Janssens, Julien Smeets, François Vander Stappen, Lucian Hotoiu, Lingshu Yin, Derek Dolney, Stephen Avery, Fionnbarr O’Grady, Damien Prieels, James McDonough, Timothy D. Solberg, Robert A. Lustig, Alexander Lin, and Boon-Keng K. Teo. Prompt Gamma Imaging for In Vivo Range Verification of Pencil Beam Scanning Proton Therapy. *International Journal of Radiation Oncology\*Biophysics*, 99(1):210–218, September 2017.
- [41] Julien Smeets, Frauke Roellinghoff, Guillaume Janssens, Irene Perali, Andrea Celani, Carlo Fiorini, Nicolas Freud, Etienne Testa, and Damien Prieels. Experimental Comparison of Knife-Edge and Multi-Parallel Slit Collimators for Prompt Gamma Imaging of Proton Pencil Beams. *Frontiers in Oncology*, 6, June 2016.

- [42] Ayako Koide, Jun Kataoka, Takamitsu Masuda, Saku Mochizuki, Takanori Taya, Koki Sueoka, Leo Tagawa, Kazuya Fujieda, Takuya Maruhashi, Takuya Kurihara, and Taku Inaniwa. Precision imaging of 4.4 MeV gamma rays using a 3-D position sensitive Compton camera. *Scientific Reports*, 8:8116, 12 2018.
- [43] E. Draeger, D. Mackin, S. Peterson, H. Chen, S. Avery, S. Beddar, and J. C. Polf. 3D prompt gamma imaging for proton beam range verification. *Physics in Medicine and Biology*, 63(3):035019, 2018.
- [44] V. Babiano, J. Balibrea, L. Caballero, D. Calvo, I. Ladarescu, J. Lerendegui, S. Mira Prats, and C. Domingo-Pardo. First i-TED demonstrator: A Compton imager with Dynamic Electronic Collimation. *Nuclear Instruments and Methods in Physics Research Section A: Accelerators, Spectrometers, Detectors and Associated Equipment*, 953:163228, 2020.
- [45] Enrique Muñoz, Ana Ros García, Marina Borja-Lloret, John Barrio, Peter Dendooven, Josep Oliver, Ikechi Ozoemelum, Jorge Roser, and Gabriela Llosá. Proton range verification with MACA-CO II Compton camera enhanced by a neural network for event selection. *Scientific Reports*, 11:9325, 04 2021.
- [46] Christian Golnik, Fernando Hueso-González, Andreas Müller, Peter Dendooven, Wolfgang Enghardt, Fine Fiedler, Thomas Kormoll, Katja Roemer, Johannes Petzoldt, Andreas Wagner, and Guntram Pausch. Range assessment in particle therapy based on prompt-gamma ray timing measurements. *Physics in Medicine and Biology*, 59(18):5399–5422, August 2014.
- [47] Joost M Verburg and Joao Seco. Proton range verification through prompt gamma-ray spectroscopy. *Physics in Medicine and Biology*, 59(23):7089–7106, November 2014.
- [48] Fernando Hueso-González, Moritz Rabe, Thomas A Ruggieri, Thomas Bortfeld, and Joost M Verburg. A full-scale clinical prototype for proton range verification using prompt gamma-ray spectroscopy. *Physics in Medicine and Biology*, 63(18):185019, September 2018.
- [49] J. Krimmer, G. Angellier, L. Balleyguier, D. Dauvergne, N. Freud, J. Hérault, J. M. Letang, H. Mathez, M. Pinto, E. Testa, and Y. Zoccarato. A cost-effective monitoring technique in particle therapy via uncollimated prompt gamma peak integration. *Applied Physics Letters*, 110(15), April 2017.
- [50] M. Pinto, D. Dauvergne, N. Freud, J. Krimmer, J. M. Letang, C. Ray, F. Roellinghoff, and E. Testa. Design optimisation of a TOF-based collimated camera prototype for online hadrontherapy monitoring. *Physics in Medicine and Biology*, 59(24):7653–7674, November 2014.
- [51] Youngmo Ku, Sehoon Choi, Jaeho Cho, Sehyun Jang, Jong Hwi Jeong, Sung Hun Kim, Sungkoo Cho, and Chan Hyeong Kim. Tackling range uncertainty in proton therapy: Development and evaluation of a new multi-slit prompt-gamma camera (MSPGC) system. *Nuclear Engineering and Technology*, 55:3140–3149, 9 2023.

- [52] J. Ready, V. Negut, L. Mihailescu, and K. Vetter. MO-FG-CAMPUS-JeP1-01: Prompt Gamma Imaging with a Multi-Knife-Edge Slit Collimator: Evaluation for Use in Proton Beam Range Verification. *Medical Physics*, 43(6Part31):3717–3717, June 2016.
- [53] Shifeng Sun, Yang Liu, and Xiaoping Ouyang. Design and performance evaluation of a coded aperture imaging system for real-time prompt gamma-ray monitoring during proton therapy. *Radiation Physics and Chemistry*, 174:108891, September 2020.
- [54] Ronja Hetzel, Vitalii Urbanevych, Andreas Bolke, Jonas Kasper, Monika Kercz, Magdalena Kołodziej, Andrzej Magiera, Florian Mueller, Sara Müller, Magdalena Rafecas, Katarzyna Rusiecka, David Schug, Volkmar Schulz, Achim Stahl, Bjoern Weissler, Ming-Liang Wong, and Aleksandra Wrońska. Near-field coded-mask technique and its potential for proton therapy monitoring. *Physics in Medicine and Biology*, 68(24):245028, December 2023.
- [55] Aleksandra Wrońska and Denis Dauvergne. Range verification by means of prompt-gamma detection in particle therapy. In Krzysztof Iniewski and Jan Iwańczyk, editors, *Radiation Detection Systems, vol. 2, Devices, Circuits, and Systems*. CRC Press/Routledge, 2021.
- [56] Hal O. Anger. Scintillation camera. *Review of Scientific Instruments*, 29(1):27–33, January 1958.
- [57] H. O. Anger and A. Gottschalk. Localization of brain tumors with the position scintillation camera. *Journal of Nuclear Medicine (U.S.)*, Vol: 4, 1963.
- [58] William R. Leo. *Techniques for Nuclear and Particle Physics Experiments: A How-to Approach*. Springer Berlin Heidelberg, 1994.
- [59] Stefaan Tavernier. *Experimental Techniques in Nuclear and Particle Physics*. Springer Berlin Heidelberg, 2009.
- [60] M.L. Roush, M.A. Wilson, and W.F. Hornyak. Pulse shape discrimination. *Nuclear Instruments and Methods*, 31(1):112–124, December 1964.
- [61] Hamamatsu. What is an SiPM and how does it work? <https://hub.hamamatsu.com/us/en/technical-notes/mppc-sipms/what-is-an-SiPM-and-how-does-it-work.html> (Accessed: 2024-31-12).
- [62] Rachel Georgel, Konstantin Grygoryev, Simon Sorensen, Huihui Lu, Stefan Andersson-Engels, Ray Burke, and Daniel O’Hare. Silicon Photomultiplier—A High Dynamic Range, High Sensitivity Sensor for Bio-Photonics Applications. *Biosensors*, 12(10):793, September 2022.
- [63] Fabio Acerbi and Stefan Gundacker. Understanding and simulating SiPMs. *Nuclear Instruments and Methods in Physics Research Section A: Accelerators, Spectrometers, Detectors and Associated Equipment*, 926:16–35, May 2019.
- [64] Guntram Pausch, Jonathan Berthold, Wolfgang Enghardt, Katja Römer, Arno Straessner, Andreas Wagner, Theresa Werner, and Toni Kögler. Detection systems for range monitoring in proton therapy: Needs and challenges.



*Nuclear Instruments and Methods in Physics Research Section A: Accelerators, Spectrometers, Detectors and Associated Equipment*, 954:161227, February 2020.

- [65] J. Krimmer, D. Dauvergne, J.M. Létang, and E. Testa. Prompt-gamma monitoring in hadrontherapy: A review. *Nuclear Instruments and Methods in Physics Research Section A: Accelerators, Spectrometers, Detectors and Associated Equipment*, 878:58–73, January 2018.
- [66] SiFi-CC. The SiFi-CC collaboration website. <https://bragg.if.uj.edu.pl/sificc> (Accessed: 2024-31-12).
- [67] Marco Pinto. Prompt-gamma imaging in particle therapy. *The European Physical Journal Plus*, 139(10), October 2024.
- [68] V. Schönfelder, A. Hirner, and K. Schneider. A telescope for soft gamma ray astronomy. *Nuclear Instruments and Methods*, 107(2):385–394, March 1973.
- [69] R. W. Todd, J. M. Nightingale, and D. B. Everett. A proposed  $\gamma$  camera. *Nature*, 251(5471):132–134, September 1974.
- [70] G.W. Phillips. Applications of Compton imaging in nuclear waste characterization and treaty verification. In *1997 IEEE Nuclear Science Symposium Conference Record*, volume 31 of NSSMIC-97, page 362–364. IEEE, 1997.
- [71] Anthony Sweeney. *Compton imaging for homeland security*. PhD thesis, University of Liverpool, 2014.
- [72] F. Roellinghoff, M.-H. Richard, M. Chevallier, J. Constanzo, D. Dauvergne, N. Freud, P. Henriquet, F. Le Foulher, J.M. Létang, G. Montarou, C. Ray, E. Testa, M. Testa, and A.H. Walenta. Design of a Compton camera for 3D prompt- $\gamma$  imaging during ion beam therapy. *Nuclear Instruments and Methods in Physics Research Section A: Accelerators, Spectrometers, Detectors and Associated Equipment*, 648:S20–S23, August 2011.
- [73] M.-H. Richard, M. Chevallier, D. Dauvergne, N. Freud, P. Henriquet, F. Le Foulher, J. M. Letang, G. Montarou, C. Ray, F. Roellinghoff, E. Testa, M. Testa, and A. H. Walenta. Design study of a Compton camera for prompt gamma imaging during ion beam therapy. In *2009 IEEE Nuclear Science Symposium Conference Record (NSS/MIC)*, volume 99, page 4172–4175. IEEE, 2009.
- [74] Shunsuke Kurosawa, Hidetoshi Kubo, Kazuki Ueno, Shigeto Kabuki, Satoru Iwaki, Michiaki Takahashi, Kojiro Taniue, Naoki Higashi, Kentaro Miuchi, Toru Tanimori, Dogyun Kim, and Jongwon Kim. Prompt gamma detection for range verification in proton therapy. *Current Applied Physics*, 12(2):364–368, March 2012.
- [75] G. Llosá, J. Cabello, S. Callier, J.E. Gillam, C. Lacasta, M. Rafecas, L. Raux, C. Solaz, V. Stankova, C. de La Taille, M. Trovato, and J. Barrio. First Compton telescope prototype based on continuous LaBr<sub>3</sub>-SiPM detectors. *Nuclear Instruments and Methods in Physics Research Section A: Accelerators, Spectrometers, Detectors and Associated Equipment*, 718:130–133, 2013.

- [76] L. Barrientos, M. Borja-Lloret, J.V. Casaña, P. Dendooven, J. García López, F. Hueso-González, M.C. Jiménez-Ramos, J. Pérez-Curbelo, A. Ros, J. Roser, C. Senra, R. Viegas, and G. Llosá. Gamma-ray sources imaging and test-beam results with MACACO III Compton camera. *Physica Medica*, 117:103199, January 2024.
- [77] Matt Young. The pinhole camera: Imaging without lenses or mirrors. *The Physics Teacher*, 27(9):648–655, December 1989.
- [78] L. Mertz and N.O. Young. Fresnel transformations of images. Proc. Int. Conf. Optical Instruments and Techniques (Chapman and Hall, London), p. 305 (1961), [https://people.csail.mit.edu/bkph/courses/papers/Coded\\_Aperture/Fresnel\\_Transform\\_Mertz\\_Young.pdf](https://people.csail.mit.edu/bkph/courses/papers/Coded_Aperture/Fresnel_Transform_Mertz_Young.pdf) (Accessed: 2024-31-12).
- [79] R. H. Dicke. Scatter-Hole Cameras for X-Rays and Gamma Rays. *The Astrophysical Journal*, 153:L101, August 1968.
- [80] L. A. Shepp and Y. Vardi. Maximum Likelihood Reconstruction for Emission Tomography. *IEEE Transactions on Medical Imaging*, 1(2):113–122, October 1982.
- [81] K. Lange and R. Carson. EM reconstruction algorithms for emission and transmission tomography. *IEEE Transactions on Medical Imaging*, 8(2):306–316, April 1984.
- [82] H.M. Hudson and R.S. Larkin. Accelerated image reconstruction using ordered subsets of projection data. *IEEE Transactions on Medical Imaging*, 13(4):601–609, 1994.
- [83] Zhiping Mu, Lawrence W. Dobrucki, and Yi-Hwa Liu. SPECT Imaging of 2-D and 3-D Distributed Sources with Near-Field Coded Aperture Collimation: Computer Simulation and Real Data Validation. *Journal of Medical and Biological Engineering*, 36(1):32–43, February 2016.
- [84] Amir Beck and Marc Teboulle. A Fast Iterative Shrinkage-Thresholding Algorithm for Linear Inverse Problems. *SIAM Journal on Imaging Sciences*, 2(1):183–202, January 2009.
- [85] A. Busboom, H. Elders-Boll, and H. D. Schotten. Uniformly Redundant Arrays. *Experimental Astronomy*, 8(2):97–123, 1998.
- [86] Stephen R. Gottesman and E. E. Fenimore. New family of binary arrays for coded aperture imaging. *Applied Optics*, 28(20):4344, October 1989.
- [87] K. Rusiecka, R. Hetzel, J. Kasper, M. Kazemi Kozani, N. Kohlhasse, M. Kołodziej, R. Lalik, A. Magiera, W. Migdał, M. Rafecas, A. Stahl, V. Urbaneych, M.L. Wong, and A. Wrońska. A systematic study of LYSO:Ce, LuAG:Ce and GAGG:Ce scintillating fibers properties. *Journal of Instrumentation*, 16(11):P11006, November 2021.

- [88] Katarzyna Rusiecka. *The SiFi-CC detector for beam range monitoring in proton therapy - characterization of components and a prototype detector module*. PhD thesis, Jagiellonian University, 2023. [10.48550/arXiv.2306.10820](https://arxiv.org/abs/10.48550/arXiv.2306.10820).
- [89] Jonas Kasper. *Optimisation of the SiFi-CC Compton camera for range verification in proton therapy through a genetic algorithm*. PhD thesis, RWTH Aachen University, 2022. [10.18154/RWTH-2022-11279](https://www.rwth-aachen.de/handle/11055/11279).
- [90] Broadcom. AFBR-S4K11C0125B SiPM Data Sheet. <https://docs.broadcom.com/doc/AFBR-S4K11C0125B-SiPM-DS> (Accessed: 2025-01-01).
- [91] Wacker. Elastosil RT 604 A/B. <https://www.wacker.com/h/en-us/c/elastosil-rt-604-ab/p/000009552> (Accessed: 2025-01-01).
- [92] CAEN. DT5742 desktop digitizer. <https://www.caen.it/products/dt5742/> (Accessed: 2025-01-01).
- [93] T. Frach, G. Prescher, C. Degenhardt, R. de Gruyter, A. Schmitz, and R. Balizany. The digital silicon photomultiplier - Principle of operation and intrinsic detector performance. In *2009 IEEE Nuclear Science Symposium Conference Record (NSS/MIC)*. IEEE, 2009.
- [94] Bjoern Weissler, Pierre Gebhardt, Peter M. Dueppenbecker, Jakob Wehner, David Schug, Christoph W. Lerche, Benjamin Goldschmidt, Andre Salomon, Iris Verel, Edwin Heijman, Michael Perkuhn, Dirk Heberling, Rene M. Botnar, Fabian Kiessling, and Volkmar Schulz. A Digital Preclinical PET/MRI Insert and Initial Results. *IEEE Transactions on Medical Imaging*, 34(11):2258–2270, November 2015.
- [95] Ltd. Jiangsu Zhongzhilian Steel Industry Co. 1060 Aluminum Sheet. <https://www.zzlsteel.com/prodetails/49/417.html> (Accessed: 2025-01-01).
- [96] Taiwan Applied Crystal. Taiwan Applied Crystal website. <https://www.tacrystal.com/> (Accessed: 2025-01-01).
- [97] Broadcom. AFBR-S4N44P164M SiPM Arrays. <https://docs.broadcom.com/doc/AFBR-S4N44P164M-DS-4x4-NUV-MT-Silicon-Photo-Multiplier-Array> (Accessed: 2025-01-01).
- [98] 3D Jake. 3D Printer Resin Aqua-Clear Plus. [https://www.3djake.pl/phrozen/aqua-resin-clear-plus?sai=17691&gad\\_source=1&gclid=EAIaIQobChMIuLud9pbPiAMVdWlBAh1vPwbtEAQYASABEgJi8vD\\_BwE](https://www.3djake.pl/phrozen/aqua-resin-clear-plus?sai=17691&gad_source=1&gclid=EAIaIQobChMIuLud9pbPiAMVdWlBAh1vPwbtEAQYASABEgJi8vD_BwE) (Accessed: 2025-01-01).
- [99] M.L. Wong, M. Kołodziej, K. Briggel, R. Hetzel, G. Korcyl, R. Lalik, A. Malige, A. Magiera, G. Ostrzolek, K. Rusiecka, A. Stahl, V. Urbanevych, M. Wiebusch, and A. Wrońska. Comparison of readout systems for high-rate silicon photomultiplier applications. *Journal of Instrumentation*, 19(01):P01019, January 2024.
- [100] CAEN Technologies Inc. FERS-5200 Front-End Readout System. <https://www.caentechnologies.com/product/fers-5200/> (Accessed: 2025-01-01).

- [101] CAEN. A5202/DT5202: 64-Channel Citiroc-1A Unit for FERS-5200 (rev. 4, 05- 2023). <https://www.caen.it/products/a5202/> (Accessed: 2024-31-12).
- [102] CAEN. Citiroc-1A Datasheet (rev. 05.2019). <https://www.caen.it/products/citiroc-1a/> (Accessed: 2024-31-12).
- [103] CAEN. DS7218 – FERS-5200 (rev.4, 03.2022). <https://www.caen.it/?downloadfile=6627> (Accessed: 2025-01-01).
- [104] Stefan Ritt. Design and performance of the 6 GHz waveform digitizing chip DRS4. In *2008 IEEE Nuclear Science Symposium Conference Record (NSS/MIC)*, pages 1512--1515, 2008.
- [105] K. Wang, S. Samaranayake, and A. Estrade. Investigation of a digitizer for the plastic scintillation detectors of time-of-flight mass measurements. *Nuclear Instruments and Methods in Physics Research Section A: Accelerators, Spectrometers, Detectors and Associated Equipment*, 1027:166050, 2022.
- [106] Antoine Laudrain. The CALICE AHCAL: a highly granular SiPM-on-tile hadron calorimeter prototype. *Journal of Physics: Conference Series*, 2374(1):012017, 2022.
- [107] K. Francis et al. Performance of the first prototype of the CALICE scintillator strip electromagnetic calorimeter. *Nuclear Instruments and Methods in Physics Research Section A: Accelerators, Spectrometers, Detectors and Associated Equipment*, 763:278--289, 2014.
- [108] CALICE. The CALICE Collaboration website. <https://twiki.cern.ch/twiki/bin/view/CALICE/> (Accessed: 2025-01-01).
- [109] K. Briggel, M. Dorn, R. Hagdorn, T. Harion, H. C. Schultz-Coulon, and W. Shen. KLauS: an ASIC for silicon photomultiplier readout and its application in a setup for production testing of scintillating tiles. *Journal of Instrumentation*, 9(02):C02013–C02013, February 2014.
- [110] Zhenxiong Yuan, Konrad Briggel, Huangshan Chen, Yonathan Munwes, Hans-Christian Schultz-Coulon, and Wei Shen. KLauS: A Low-power SiPM Readout ASIC for Highly Granular Calorimeters. In *2019 IEEE Nuclear Science Symposium and Medical Imaging Conference (NSS/MIC)*, volume 30, page 1–4. IEEE, 2019.
- [111] Agostino Di Francesco, Ricardo Bugalho, Luis Oliveira, Angelo Rivetti, Manuel Rolo, Jose C. Silva, and Joao Varela. TOFPET 2: A high-performance circuit for PET time-of-flight. *Nuclear Instruments and Methods in Physics Research Section A: Accelerators, Spectrometers, Detectors and Associated Equipment*, 824:194--195, 2016. Frontier Detectors for Frontier Physics: Proceedings of the 13th Pisa Meeting on Advanced Detectors.
- [112] PETsys. SiPM Readout System (v.15, 07.2023). [https://www.petsyselectronics.com/web/website/docs/products/product4/Long%20Flyer%20SiPM%20readout%20chain\\_v15.pdf](https://www.petsyselectronics.com/web/website/docs/products/product4/Long%20Flyer%20SiPM%20readout%20chain_v15.pdf) (Accessed: 2025-01-01).

- [113] GSI Helmholtzzentrum für Schwerionenforschung, Darmstadt and FAIR GmbH, Darmstadt. *GSI-FAIR Scientific Report 2021*. 2021. [10.15120/GSI-2022-00454](#).
- [114] GSI Helmholtzzentrum für Schwerionenforschung. The TRB family. <http://trb.gsi.de/> (Accessed: 2025-01-01).
- [115] A. Neiser et al. TRB3: a 264 channel high precision TDC platform and its applications. *Journal of Instrumentation*, 8:C12043, 2013.
- [116] M. Rudigier, Zs. Podolyák, P.H. Regan, A.M. Bruce, S. Lalkovski, R.L. Canavan, E.R. Gamba, O. Roberts, I. Burrows, D.M. Cullen, L.M. Fraile, L. Gerhard, J. Gerl, M. Gorska, A. Grant, J. Jolie, V. Karayonchev, N. Kurz, W. Korten, I.H. Lazarus, C.R. Nita, V.F.E. Pucknell, J.-M. Régis, H. Schaffner, J. Simpson, P. Singh, C.M. Townsley, J.F. Smith, and J. Vesic. FATIMA — FAsT TIMing array for DESPEC at FAIR. *Nuclear Instruments and Methods in Physics Research Section A: Accelerators, Spectrometers, Detectors and Associated Equipment*, 969:163967, 2020.
- [117] Jan Michel, Ingo Frohlich, Michael Bohmer, Grzegorz Korcyl, Ludwig Maier, Marek Palka, Joachim Stroth, Michael Traxler, and Sergey Yurevich. The HADES trigger and readout board network (TrbNet). In *2010 17th IEEE-NPSS Real Time Conference*, page 1–5. IEEE, 2010.
- [118] J. Adamczewski-Musch, N. Kurz, and S. Linev. Developments and applications of DAQ framework DABC v2. *Journal of Physics: Conference Series*, 664(8):082027, 2015.
- [119] P. Anfre, C. Dujardin, J.-M. Fourmigue, B. Hautefeuille, K. Lebbou, C. Pedrini, D. Perrodin, and O. Tillement. Evaluation of fiber-shaped LYSO for double readout gamma photon detection. *IEEE Transactions on Nuclear Science*, 54(2):391--397, April 2007.
- [120] Keysight. 81160A Pulse Function Arbitrary Noise Generator. <https://www.keysight.com/us/en/product/81160A/81160a-pulse-function-arbitrary-noise-generator.html> (Accessed: 2025-01-01).
- [121] Thorlabs, Inc. BK5 Black Nylon, Polyurethane-Coated Fabric. <https://www.thorlabs.com/thorproduct.cfm?partnumber=BK5> (Accessed: 2025-01-01).
- [122] Magdalena Kołodziej, Stephan Brons, Mikołaj Dubiel, George N. Farah, Alexander Fenger, Ronja Hetzel, Jonas Kasper, Monika Kercz, Barbara Kołodziej, Linn Mielke, Gabriel Ostrzolek, Magdalena Rafecas, Jorge Roser, Katarzyna Rusiecka, Achim Stahl, Vitalii Urbanevych, Ming-Liang Wong, and Aleksandra Wrońska. First experimental test of a coded-mask gamma camera for proton therapy monitoring, 2025. arXiv preprint arXiv:2501.00666, <https://arxiv.org/abs/2501.00666>.
- [123] Ltd Henan Tendeli Metallurgical Materials Co. 8011 Aluminum Sheet. <https://www.htmmgroup.com/aluminium-foil/alloy-8011-o-temper-household-aluminum-f.html> (Accessed: 2025-01-01).

- [124] Th. Haberer, J. Debus, H. Eickhoff, O. Jäkel, D. Schulz-Ertner, and U. Weber. The Heidelberg Ion Therapy Center. *Radiotherapy and Oncology*, 73:S186–S190, 2004.
- [125] Heidelberg University Hospital. Heidelberg Ion-beam Therapy Center. <https://www.klinikum.uni-heidelberg.de/> (Accessed: 2025-01-01).
- [126] National Institute of Standards and Technology. The PSTAR program: Stopping Power and Range Tables for Protons. <https://physics.nist.gov/PhysRefData/Star/Text/PSTAR.html> (Accessed: 2025-01-01).
- [127] Broadcom. AFBR-S4NxxPyy4M NUV-MT SiPM Performance Correlation - application note. <https://docs.broadcom.com/doc/AFBR-S4NxxPyy4M-NUV-MT-SiPM-Performance-Correlation> (Accessed: 2025-01-01).
- [128] H. Alva-Sánchez, A. Zepeda-Barrios, V. D. Díaz-Martínez, T. Murrieta-Rodríguez, A. Martínez-Dávalos, and M. Rodríguez-Villafuerte. Understanding the intrinsic radioactivity energy spectrum from  $^{176}\text{Lu}$  in LYSO/LSO scintillation crystals. *Scientific Reports*, 8(1), November 2018.
- [129] PETsys Electronics. TOFPET2 Data Acquisition Software. [https://github.com/PETsys/sw\\_daq\\_tofpet2](https://github.com/PETsys/sw_daq_tofpet2) (Accessed: 2025-01-01).
- [130] M. L. Wong. Modified TOFPET2 Data Acquisition Software. <https://github.com/SiFi-CC/DAQ/tree/nonLinCorr> (Accessed: 2025-01-01).
- [131] PETsys Electronics. TOFPET2 ASIC SiPM Readout System software user guide, v.2022.04.
- [132] SiFi-CC collaboration. SiFi framework. [https://github.com/SiFi-CC/sifi-framework/tree/4to1\\_classes\\_HIT\\_refactoring](https://github.com/SiFi-CC/sifi-framework/tree/4to1_classes_HIT_refactoring) (Accessed: 2025-01-01).
- [133] James F. Ziegler. The Stopping and Range of Ions in Matter (SRIM) Software. <http://www.srim.org/> (Accessed: 2025-01-01).
- [134] S. Agostinelli, J. Allison, K. Amako, J. Apostolakis, H. Araujo, P. Arce, M. Asai, D. Axen, S. Banerjee, G. Barrand, F. Behner, L. Bellagamba, J. Boudreau, L. Broglia, A. Brunengo, H. Burkhardt, S. Chauvie, J. Chuma, R. Chytrcek, G. Cooperman, G. Cosmo, P. Degtyarenko, A. Dell’Acqua, G. Depaola, D. Dietrich, R. Enami, A. Feliciello, C. Ferguson, H. Fesefeldt, G. Folger, F. Foppiano, A. Forti, S. Garelli, S. Giani, R. Giannitrapani, D. Gibin, J.J. Gómez Cadenas, I. González, G. Gracia Abril, G. Greeniaus, W. Greiner, V. Grichine, A. Grossheim, S. Guatelli, P. Gumplinger, R. Hamatsu, K. Hashimoto, H. Hasui, A. Heikkinen, A. Howard, V. Ivanchenko, A. Johnson, F.W. Jones, J. Kallenbach, N. Kanaya, M. Kawabata, Y. Kawabata, M. Kawaguti, S. Kelner, P. Kent, A. Kimura, T. Kodama, R. Kokoulin, M. Kossov, H. Kurashige, E. Lamanna, T. Lampén, V. Lara, V. Lefebure, F. Lei, M. Liendl, W. Lockman, F. Longo, S. Magni, M. Maire, E. Medernach, K. Minamimoto, P. Mora de Freitas, Y. Morita,



- K. Murakami, M. Nagamatu, R. Nartallo, P. Nieminen, T. Nishimura, K. Ohtsubo, M. Okamura, S. O’Neale, Y. Oohata, K. Paech, J. Perl, A. Pfeiffer, M.G. Pia, F. Ranjard, A. Rybin, S. Sadilov, E. Di Salvo, G. Santin, T. Sasaki, N. Savvas, Y. Sawada, S. Scherer, S. Sei, V. Sirotenko, D. Smith, N. Starkov, H. Stoecker, J. Sulkimo, M. Takahata, S. Tanaka, E. Tcherniaev, E. Safai Tehrani, M. Tropeano, P. Truscott, H. Uno, L. Urban, P. Urban, M. Verderi, A. Walkden, W. Wander, H. Weber, J.P. Wellisch, T. Wenaus, D.C. Williams, D. Wright, T. Yamada, H. Yoshida, and D. Zschesche. Geant4—a simulation toolkit. *Nuclear Instruments and Methods in Physics Research Section A: Accelerators, Spectrometers, Detectors and Associated Equipment*, 506(3):250–303, 2003.
- [135] Geant4 Collaboration. Guide For Physics Lists. release 11.3, <https://geant4-userdoc.web.cern.ch/UsersGuides/PhysicsListGuide/fo/PhysicsListGuide.pdf> (Accessed: 2025-01-01).
- [136] E. Dietz-Laursonn, T. Hebbeker, A. Künsken, M. Merschmeyer, S. Nieswand, and T. Niggemann. GODDeSS: A Geant4 extension for easy modelling of optical detector components. *Journal of Instrumentation*, 12:P04026–P04026, 04 2017.
- [137] M. Rafecas, B. Mosler, M. Dietz, M. Pogl, D.P. McElroy, and S.I. Ziegler. Use of a Monte-Carlo based probability matrix for 3D iterative reconstruction of MADPET-II data. In *2003 IEEE Nuclear Science Symposium. Conference Record*, pages 1775–1779 Vol.3. IEEE, 2003.
- [138] P. Gueth, D. Dauvergne, N. Freud, J. M. Létang, C. Ray, E. Testa, and D. Sarut. Machine learning-based patient specific prompt-gamma dose monitoring in proton therapy. *Physics in Medicine and Biology*, 58(13):4563–4577, June 2013.
- [139] SciPy Documentation. `scipy.ndimage.gaussian_filter` function. [https://docs.scipy.org/doc/scipy/reference/generated/scipy.ndimage.gaussian\\_filter.html](https://docs.scipy.org/doc/scipy/reference/generated/scipy.ndimage.gaussian_filter.html) (Accessed: 2025-01-01).
- [140] Bradley Efron. *Bootstrap Methods: Another Look at the Jackknife*, page 569–593. Springer New York, 1992.
- [141] A. Di Francesco, R. Bugalho, L. Oliveira, L. Pacher, A. Rivetti, M. Rolo, J.C. Silva, R. Silva, and J. Varela. TOFPET2: a high-performance ASIC for time and amplitude measurements of SiPM signals in time-of-flight applications. *Journal of Instrumentation*, 11(03):C03042–C03042, March 2016.
- [142] Stefanie Bertschi, Kristin Stützer, Jonathan Berthold, Julian Pietsch, Julien Smeets, Guillaume Janssens, and Christian Richter. Potential margin reduction in prostate cancer proton therapy with prompt gamma imaging for online treatment verification. *Physics and Imaging in Radiation Oncology*, 26, 4 2023.